Tropical Cyclogenesis Via Convectively Forced Vortex Rossby Waves In A Three-Dimensional Quasigeostrophic Model

Janice Enagonio and Michael T. Montgomery

Research supported by the National Science Foundation
Grant # NSF ATM-9529295.

Colorado State University

DEPARTMENT OF ATMOSPHERIC SCIENCE

PAPER NO. 656

TROPICAL CYCLOGENESIS VIA CONVECTIVELY FORCED VORTEX ROSSBY WAVES IN A THREE-DIMENSIONAL QUASIGEOSTROPHIC MODEL

Janice Enagonio and Michael T. Montgomery

Research supported by National Science Foundation Grants ATM-9312655 and ATM-9529295

Principal Investigator: Michael T. Montgomery

Department of Atmospheric Science
Colorado State University
Fort Collins, CO 80523

July 1998

Atmospheric Science Paper No. 656

ABSTRACT

This work investigates the problem of tropical cyclogenesis in three dimensions. In particular, we examine the interaction of small-scale convective disturbances with a larger-scale vortex circulation in a nonlinear quasigeostrophic balance model. Convective forcing is parameterized by its estimated net effect on the potential vorticity field. Idealized numerical experiments show that vortex intensification proceeds by ingestion of like-sign potential vorticity anomalies into the parent vortex and expulsion of opposite-sign potential vorticity anomalies during the axisymmetrization process. For the finite amplitude forcing considered here the weakly nonlinear vortex Rossby wave, mean-flow predictions for the magnitude and location of the spinup are in good agreement with the model results. Vortex development is analyzed using Lagrangian trajectories, Eliassen-Palm flux vectors, and the Lorenz energy cycle.

Using numerical estimates of the magnitude of PV injection based on previous observational and theoretical work, we obtain spinup to a 15 ms^{-1} cyclone on realistic time scales. Simulation of a midlevel vortex with peripheral convection shows that axisymmetrization results in the spinup of a surface cyclone. The axisymmetrization mechanism demonstrates the development of a warm-core vortex. The relative contribution from eddy heat fluxes and eddy momentum fluxes to the warm core structure of the cyclone is investigated.

The vortex spinup obtained shows greater than linear dependence on the forcing amplitude, indicating the existence of a nonlinear feedback mechanism associated with the vortex Rossby waves.

Building on recent work by several authors, this work further clarifies the significance of the axisymmetrization process for the problem of tropical cyclogenesis. The theory

is shown to be consistent with published observations of tropical cyclogenesis. Further observational tests of the theory, specific to the dynamics examined here, are proposed.

ACKNOWLEDGEMENTS

We gratefully acknowledge Dr. Richard Johnson for his assistance in estimating tropical convective heating rates. We also thank Dr. Gerhard Dangelmayr and Dr. Wayne Schubert, who, as members of the first author's M.S. thesis committee, contributed many valuable comments. Mr. Paul Reasor provided many helpful discussions as well as assistance in implementation of the semispectral model. We also acknowledge Dr. James McWilliams, Dr. Michael McIntyre, Dr. Raymond Pierrehumbert, Dr. Dominique Moeller, Dr. Lloyd Shapiro, Dr. Vic Ooyama and Ms. Zongjun Yang for insightful comments and discussions. We appreciate the computing support provided by Mr. David Stepaniak and Mr. Rick Taft. This work was supported in part by National Science Foundation grants ATM-9312655 and ATM-9529295.

CONTENTS

LIST OF FIGURES

Chapter 1

INTRODUCTION

Tropical cyclones form in the presence of convective disturbances in the tropics. Many such disturbances are present in an ocean basin at any time. However, only a small fraction (about 80 per year) evolve into tropical storms, which may in turn become hurricanes. It is generally accepted that favorable climatological conditions for tropical cyclogenesis include the presence of low-level cyclonic relative vorticity, the presence of low-level convergence, the absence of strong vertical shear of the horizontal winds, an atmosphere conducive to deep moist convection, a significant value of the planetary vorticity, and sea surface temperatures greater than approximately 26°C with a deep oceanic mixed layer. About 80% of all tropical cyclones originate in or near the monsoon troughs or the Intertropical Convergence Zone; most others form from disturbances in the easterly trade winds (Gray 1968, Frank 1987).

There have been several significant theoretical studies of tropical cyclogenesis. Kurihara and Tuleya (1981) studied cyclogenesis in a primitive equation numerical model. The initial state used was an idealization of an environment in which tropical storms in the Atlantic Ocean are observed to form. A shallow easterly wave was the cause of the initial disturbance. In the model results, a pressure drop from 1008 mb to 1002 mb occurred in 96 hr, with the maximum low-level wind intensifying to greater than 17 ms^{-1} after 96 hr. The development of a tropical depression with a cluster-type cloud distribution and increasing rainfall from an initially cloud-free state was observed. A warm core formed initially at approximately 335 mb and propagated downward during the intensification from tropical depression to tropical storm. A moist column extending from 200 to 700 mb developed by 96 hr. The tropical storm showed intense precipitation of 11 mm/hr within

a 300 km diameter region near the center, with less precipitation in the outer regions. An upper-level disturbance also evolved in the course of the integration. Kurihara and Tuleya also studied the effects of diabatic heating and, in an accompanying study (Tuleya and Kurihara 1981), the effects of environmental winds on storm genesis.

Challa and Pfeffer (1980, 1990) and Pfeffer and Challa (1981) studied the effect of large-scale asymmetries on tropical cyclone formation. They stressed the key role of large-scale upper-level eddy-momentum-flux convergence in the cyclogenesis process. Eddy-momentum-flux convergence induces a radial circulation which supplies warm, moist air to the center of the storm. Challa and Pfeffer (1990) based the initial conditions for their model on composites for developing and nondeveloping Atlantic tropical disturbances. The developing composite showed a large inward flux of angular momentum near 200 mb, at radii from 6° to 14° latitude from the disturbance's center. The composite of non-developers did not show a pronounced large-scale angular momentum flux. Challa and Pfeffer performed model integrations beginning with developer and nondeveloper composites. They also studied cases for which the initial conditions were the axially symmetric components of the composites for developers. They found that in all cases for which the initial conditions had large eddy-momentum-flux convergences, hurricanes developed in their model; for all cases for which the initial conditions did not, hurricanes did not develop. They concluded that cooperative instability and Ekman pumping alone are not sufficient to amplify Atlantic tropical disturbances into hurricanes.

Rotunno and Emanuel (1987) and Emanuel (1989) studied intensification from the air-sea interaction viewpoint. To investigate the role of convective available potential energy, Rotunno and Emanuel considered an idealized axisymmetric model with an explicit representation of convection and obtained spinup of a tropical cyclone beginning with a nearly convectively neutral sounding. In their theory, a finite-amplitude disturbance (a pre-existing vortex of 12 ms^{-1} maximum winds) is required in order to initiate genesis. Spinup then proceeds by a feedback between the radial temperature gradients which drive the vortex's circulation and anomalous sea-air heat transfer due to frictional inflow. The question of whether their models would also simulate cyclogenesis from a less intense pre-existing vortex of perhaps 5 ms^{-1} was left open.

Montgomery and Farrell (1993) proposed a cyclogenesis mechanism due to upper-level potential vorticity (PV) anomalies interacting with a low-level vortex. Studies of this mechanism were made in two- and three-dimensional geostrophic momentum models. In a nearly moist neutral environment associated with cumulus convection, geostrophic lifting causes vortex stretching and thus spinup of the lower vortex. Depending on model parameters, cyclones of tropical storm intensity were obtained on time scales of 2.5-3.6 days, and an incipient spiral structure was seen at the surface. This mechanism was advanced to describe genesis in the subtropics, but left open the issue of genesis in the deep tropics.

Shapiro (1977) studied the transformation of easterly waves to tropical depressions. Shapiro developed a parameter ϵ', which estimates the importance of nonlinear vorticity advection (wave self-interaction) in the disturbance. Quasi-linear easterly waves are characterized by a balance between linear advection (local time changes and advection by the mean wind) and the Coriolis, pressure gradient and frictional forces. In a tropical storm the balance is between the Coriolis force and nonlinear advection, in particular centrifugal acceleration. Large ϵ' indicates increasing importance of nonlinear contributions to the wave processes, and thus may be expected to indicate the onset of storm formation. Shapiro described a means of determining ϵ' from regular operational wind observations, and applied the ϵ' criterion to climatological data and to the data from a single hurricane season.

Fritsch et al. (1994) described the radial growth and intensification of a warm core vortex over land. The authors suggested that such mesoscale vortices could provide the "starter vortex" required in some models of tropical cyclogenesis including that to be described in our paper. Fritsch et al. noted that over land – at least for the vortex they described – low-level cooling from melting and evaporation appeared to be too strong to allow the formation of a surface mesolow and surface warm core. They speculated that strong, long-term fluxes of warm, moist air from a warm water surface might be required for the formation of a tropical cyclone.

Bosart and Sanders (1981) found that the mesoscale convective complex (MCC) responsible for the Johnstown flood became a tropical storm as it moved out over the warm

water of the Atlantic. Numerical simulations and some observational evidence (see Zhang and Fritsch 1987 and references therein) indicated that this MCC formed an inertially stable warm-core vortex. It has also been observed (Velasco and Fritsch 1987) that, of MCCs occurring over water, a significant fraction develop into tropical storms, perhaps because MCCs are often associated with midlevel vortices.

Harr et al. (1996) reported a case study of the formation of a midget tropical cyclone during the TCM-93 field experiment. During two aircraft observation periods, three mesoscale convectively-generated vortices (MCVs) were identified in association with an area of persistent deep convection near a monsoon gyre. Only one of these MCVs developed into a low-level circulation; it eventually became tropical storm Ofelia. The successfully developing MCV was located within the cyclonic shear zone of the monsoon gyre. The development of the MCV into a tropical depression was accompanied by a strong outbreak of deep convection.

The cyclogenesis process examined here builds on the recent studies of vortex axisymmetrization and vortex Rossby wave dynamics by MacDonald (1968), Guinn and Schubert (1993), Smith and Montgomery (1995), Kallenbach and Montgomery (1995) and Montgomery and Kallenbach (1997; henceforth MK). MacDonald suggested that spiral rainbands in mature hurricanes might be due to Rossby waves on the vorticity gradient of the cyclone, and made quantitative observational estimates of the flux of cyclonic angular momentum from spiral band eddies toward the hurricane's radius of maximum winds. Guinn and Schubert made an extensive study of the connection between PV or vortex Rossby waves and mature hurricane spiral bands, including a simulation of the PV dynamics of convective asymmetries. Guinn and Schubert also discussed tropical cyclogenesis via ITCZ breakdown.

MK studied azimuthally and radially propagating asymmetric disturbances on a circular vortex using an exact solution for wavenumber one due to Smith and Rosenbluth (1990), WKB solutions, a nondivergent numerical model, and a shallow water asymmetric balance (AB) model (Shapiro and Montgomery 1993, Kallenbach and Montgomery 1995, MK). These studies also indicated the existence of radially-propagating, wavelike

disturbances which depended on the radial gradient of the basic state vorticity and were therefore identified as vortex Rossby waves. Using the WKB approximation, MK derived dispersion relations and expressions for the radial and azimuthal group velocities for the nondivergent and divergent shallow water cases. The WKB results were validated using the numerical models.

MK also examined the possible relationship between hurricane spiral bands and vortex Rossby waves. The AB model results were compared to high-resolution radar reflectivity observations of spiral bands studied by Tuttle and Gall (1995). The model results were consistent with the observations, but it was concluded that further observations were required to verify the existence of vortex Rossby waves in hurricanes.

MK also studied vortex Rossby wave, mean flow interactions in the nondivergent model. They hypothesized that initial vorticity asymmetries such as those which arise from moist convective forcing would accelerate the mean tangential winds, and proposed this interaction as a mechanism for tropical cyclogenesis. These ideas are analogous to the problem of the intensification and maintenance of a large-scale zonal jet by forced planetary Rossby waves (Shepherd 1987) except the pertinent vorticity gradient in our case is the radial vorticity gradient of the vortex. This paper tests the MK spinup mechanism in a fully nonlinear, three-dimensional quasigeostrophic (QG) balance model. The three-dimensional character of the model allows the investigation of the vortex's eddy-forced secondary circulation, crucial to understanding the origin of the vortex's warm core.

We examine the problem of vortex development associated with the production of cyclonic vertical vorticity by cumulus convection. Such convection could be caused by environmental forcing (Challa and Pfeffer 1980,1990, Pfeffer and Challa 1981, Montgomery and Farrell 1993), or by mesoscale processes. Although it has long been known that energy extracted from the underlying ocean and realized as latent heat during condensation provides the principal energy source for tropical cyclones, and this process has been simulated by numerical models such as that of Ooyama (1969) and Kurihara and Tuleya (1981), this work further elucidates the non-axisymmetric advective dynamics that promotes the upscale transfer of convective-scale energy to vortex-scale energy. Organization

of convection by the storm is not necessary in our model, although organization into a tropical cloud cluster or mesoscale convective system is assumed. The cyclogenesis mechanism proposed here does not require a cooperative interaction between convection and the large-scale vortex. Cooperative interaction (Smith 1997; Stevens et al. 1997; Ooyama 1982) could enhance the development process presented here at later stages in the cyclone life cycle, and may become the dominant development mechanism by the hurricane stage. For simplicity, we also ignore the possible effects of ambient vertical shear.

Our work describes cyclogenesis from a pre-existing mesoscale vortex in the presence of convection, such as that which would be present in a tropical cloud cluster. The initiating vortex in our simulations has a 200 km radius of maximum tangential winds (RMW) and an initial maximum tangential wind speed of 5 ms^{-1}. The physical setup is consistent with typical values for mesoscale convectively-generated vortices (Johnston 1981; Bartels and Maddox 1991). Cyclonic vortices of this type could also be found within the closed flow patterns occurring in easterly waves (Reed et al. 1977). PV anomalies generated by cumulus convection on the periphery of the vortex axisymmetrize into the parent vortex. Although this process can be described phenomenologically as vortex merger and stripping, we show that it is also useful to characterize it in terms of the interaction between vortex Rossby waves and the mean flow. The wave, mean-flow approach, which has proven successful in describing other atmospheric phenomena such as the quasi- biennial oscillation and sudden stratospheric warmings (Holton 1992), is shown here to yield valid quantitative predictions for the magnitude and location of the vortex spinup at the finite amplitudes relevant to the cyclogenesis problem. The formation of a 5K warm core within a reasonable time scale provides compelling evidence that our proposed mechanism may capture the essence of the cyclogenesis process. In addition, we find that symmetric outbreaks of penetrative convection near the center of the pre-existing vortex wil give stronger and more rapid spinup. Our cyclogenesis theory is in good agreement with the case study by Harr et al. (1996) described above, in which cyclogenesis was accompanied by a strong outbreak of convection.

Sensitivity studies of the axisymmetrization mechanism reveal the presence of nonlinear feedback in the spinup process, with the increase in tangential velocity generally having a greater than linear proportionality to the forcing amplitude.

The cyclogenesis mechanism proposed here may be contrasted with cyclogenesis due to the interaction and merger of midlevel MCVs produced in the stratiform region of mesoscale convective systems in a favorable large-scale environment (Simpson et al. 1997, Ritchie and Holland 1997, Ritchie 1995). Our mechanism focuses on the process by which PV (or vorticity) anomalies due to moist penetrative convection relax to axisymmetry in the presence of a pre-existing vortex, such as an MCV or a low-level cyclonic vorticity anomaly. The difference between these two approaches lies in the emphasis placed on the importance of convective versus stratiform heating. The two ideas are not mutually exclusive; in fact, Ritchie and Holland (1997; section 4b) describe an interaction of two low-level circulations in the early stages of cyclogenesis which may well be an example of our process. In addition, our work demonstrates the usefulness of the underlying vortex Rossby wave dynamics in describing the redistribution of convectively-induced PV.

In Chapters 2 and 3 we discuss the formulation and implementation of the models used in our studies. The reader already familiar with the models may skip to Chapter 4, where we examine three-dimensional vortex axisymmetrization in the presence of convection. Vortex axisymmetrization is studied from the viewpoints of wave, mean flow interaction, Lagrangian trajectories and the energy budget. Chapter 5 examines vortex spinup in the presence of ongoing convection, and describes sensitivity tests of our results. Chapter 6 reviews the most relevant observations of tropical cyclogenesis to our theory. Chapter 7 summarizes the results of our work and proposes further observational tests of the theory.

A summary version of this work is to be published in the *Journal of the Atmospheric Sciences* (Montgomery and Enagonio 1998).

Chapter 2

MODEL FORMULATION

2.1 Introduction

This chapter describes the formulation of the primary theoretical model used for our studies. We first present the primitive equations in pseudo-height coordinates. We next motivate the QG approximation, non-dimensionalize the primitive equations, and then derive the QG equations. Our model, here called the QG3D model, describes QG motion on an f-plane. The model uses three basic equations, for invertibility, adiabatic motion and PV conservation. The reader already familiar with QG theory may wish to go directly to Chapter 4 where the presentation of results begins.

2.2 Primitive Equations in Pseudo-Height Coordinates

For our vertical coordinate we adopt the pseudo-height z (Hoskins and Bretherton 1972) :

$$z = \frac{c_p \theta_0}{g}\left[1 - \left(\frac{p}{p_0}\right)^{R/C_p}\right] = \frac{\gamma}{\gamma - 1} H_s \left[1 - \left(\frac{p}{p_0}\right)^{(\gamma-1)/\gamma}\right], \tag{2.1}$$

where H_s is the scale height, C_p is the specific heat of air at constant pressure, C_v is the specific heat at constant volume, γ is the ratio C_p/C_v, and zero subscripts refer to typical values at the Earth's surface. The scale height H_s is based on the surface temperature $H_s = RT_s/g = p_0/(\rho_0 g)$. The maximum z is attained when $p \to 0$. For a scale height of 8 km,

$$z_a \equiv z_{max} = \frac{\gamma}{\gamma - 1} H_s \approx 28 \text{ km}. \tag{2.2}$$

From (2.1) one obtains

$$dz = -\frac{\theta_0}{\rho g \Theta} dp, \tag{2.3}$$

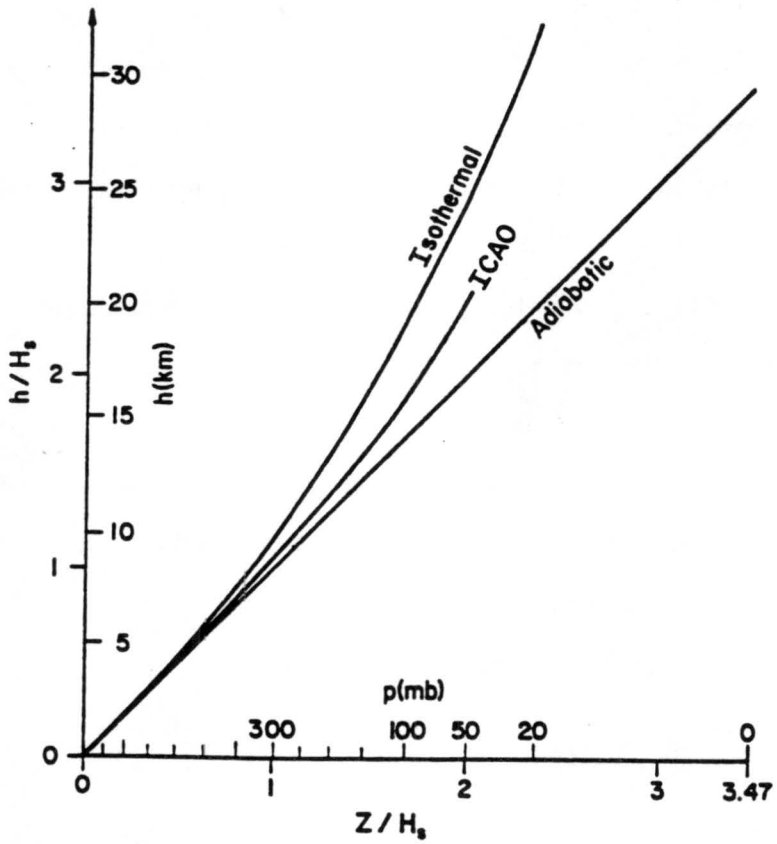

Figure 2.1: Relationship between pseudo-height z and physical height h for the ICAO standard atmosphere and for isothermal and adiabatic atmospheres (from Hoskins and Bretherton 1972).

and for the physical height h,

$$\frac{dp}{dh} = -\rho g. \tag{2.4}$$

It follows that $\theta_0 dh = \Theta dz$. For an adiabatic atmosphere ($\Theta \equiv \theta_0$), the pseudoheight equals the physical height, $z = h$. The relationship between z and h for various atmospheres is shown in Figure 2.1 from Hoskins and Bretherton (1972). Typical atmospheric soundings give a curve between the isothermal and adiabatic curves, so $z \approx h$ is usually a good approximation in the troposphere for stably stratified large-scale flows.

In this theoretical study it is sufficient to consider an idealized atmosphere bounded below by a rigid horizontal surface at $h = 0$ (Earth's surface) and unbounded above. The vertical boundary conditions are $w \equiv dz/dt = 0$ at $z = z_a$ and $w = 0$ at $z = 0$. The first condition follows from the definition of z and w in terms of pressure (at $p = 0$ there can be no vertical motion). The second condition is an approximation based on the fact that at the ground we must have $dh/dt = 0$. Since $z \approx h$, it follows that $w \approx 0$ at $z = 0$. This boundary condition filters Lamb waves.

It proves convenient to introduce the pseudo-density

$$\rho_*(z) = \rho_0 \left(\frac{p}{p_0}\right)^{1/\gamma} = \rho_0 \left(1 - \frac{z}{z_a}\right)^{1/(\gamma-1)} \tag{2.5}$$

which is a known function of pressure only. ρ_* is chosen so that

$$\frac{dp}{dz} = -\rho_* g. \tag{2.6}$$

In pseudo-height coordinates, the adiabatic f - plane primitive equations are

$$\frac{Du}{Dt} - fv = -\frac{\partial \Phi}{\partial x}, \tag{2.7}$$

$$\frac{Dv}{Dt} + fu = -\frac{\partial \Phi}{\partial y}, \tag{2.8}$$

$$\nabla \cdot (\rho_* \mathbf{v}) = 0, \tag{2.9}$$

$$\frac{D\Theta}{Dt} = 0, \tag{2.10}$$

$$\frac{\partial \Phi}{\partial z} = \frac{g}{\theta_0}\Theta, \tag{2.11}$$

where $\nabla = \mathbf{i}\partial_x + \mathbf{j}\partial_y + \mathbf{k}\partial_z$ and

$$\frac{D}{Dt} = \frac{\partial}{\partial t} + u\frac{\partial}{\partial x} + v\frac{\partial}{\partial y} + w\frac{\partial}{\partial z}$$

is the material derivative. Here (x, y) are the horizontal Cartesian coordinates, t is time, f is the local Coriolis parameter, $\mathbf{v} = (u, v, w) = (Dx/Dt, Dy/Dt, Dz/Dt)$, Φ is the geopotential and Θ the potential temperature.

Since ρ_* is a function of z only, (2.9) can be written

$$\frac{\partial u}{\partial x} + \frac{\partial v}{\partial y} + \frac{1}{\rho_*}\frac{\partial(\rho_* w)}{\partial z} = 0, \tag{2.12}$$

from which

$$\nabla \cdot \mathbf{v} = \frac{w}{\gamma H_s(1 - \frac{z}{z_a})}. \tag{2.13}$$

If the characteristic vertical scale for w is much smaller than the scale height, the term on the right side of (2.13) can be neglected. In this case the continuity equation reduces to

$$\nabla \cdot \mathbf{v} = 0. \tag{2.14}$$

Strictly, the Boussinesq approximation requires that the characteristic vertical scale of w be small compared to the scale height. Experience has shown us, however, that limitations of the Boussinesq approximation are not as severe as scaling suggests.

2.3 Quasigeostrophic Approximation

We next develop the QG approximation to the primitive equations. The QG approximation has two major advantages. First, it simplifies the equations of motion. The QG approximation leads to the definition of the QG PV, which in the absence of diabatic heating is conserved following the geostrophic wind. A simple linear relationship between the QG PV and the geopotential, independent of time and of the ageostrophic velocities, is derived. Thus, one obtains a simple predictive algorithm for the PV and geopotential (and thus for the winds, temperature and vorticity). The second advantage of the QG formulation is that it filters gravity waves, which occur on time scales much shorter than the geostrophic motion.

The QG approximation is valid provided the Rossby number $\epsilon = U/fL \ll 1$, where U is a characteristic horizontal velocity and L a characteristic horizontal length scale. For a circular vortex forced by small but finite amplitude asymmetries this condition becomes $\epsilon_{vortex} = v(r)/fr$, where $v(r)$ is the basic state tangential wind of the model vortex and r is the radius from the center of the vortex. In our work v is initially 5 ms^{-1} at the RMW and the RMW is 200 km; taking $f = 5 \cdot 10^{-5}$ s^{-1}, we obtain $\epsilon = 0.5$ at the RMW. As the tangential winds increase, ϵ_{vortex} becomes ≈ 1. For the results presented in this paper we take $f = 10^{-4}$ s^{-1}. Although the value for f is roughly twice that found at tropical latitudes, we have chosen the higher value in order to keep the initial Rossby number of the symmetric vortex less than unity. The justification for using the larger value of f is based on the idea of incorporating the average rotation rate of an incipient vortex into the definition of f. The physical justification behind this idea is provided in Shapiro and Montgomery (1993), where the balance theory derived was based on a generalized Rossby number incorporating the local rotation rate of the vortex. An analysis of our results using the primitive equations and asymmetric balance equations (Shapiro and Montgomery 1993) is a topic of current work which will be reported in due course. Note that the basic axisymmetrization results described in Chapter 4 have maximum Rossby numbers of approximately 0.5 with Rossby numbers of about 0.3 at the RMW. The QG approximation is used here because of its simplicity; we believe that its regime of practical validity extends beyond the range of formal validity $\epsilon \ll 1$.

The QG equations of motion are traditionally obtained by carrying out a series expansion of the dependent variables u,v, Φ and w in powers of the Rossby number. Although the formulation has been thoroughly developed elsewhere (e.g. Charney 1948; Lindzen 1990), the derivation of the QG approximation is reproduced here for its pedagogical value.

Before carrying out the ϵ-expansion it is useful to consider a fluid at rest in hydrostatic equilibrium. The static stability

$$N_r^2(z) = \frac{g}{\theta_0}\frac{d\theta_r}{dz} = N_r^2(z, \text{only}), \tag{2.15}$$

with θ_r the potential temperature of the resting basic state.

The hydrostatic equation then gives

$$\frac{g}{\theta_0}\theta_r = \frac{\partial \phi_r}{\partial z}, \tag{2.16}$$

where ϕ_r is the geopotential of the resting basic state. Writing θ_r as the sum of its value at $z = 0$ plus a function of z

$$\theta_r = \theta_0(1 + f(z)), \tag{2.17}$$

equation (2.16) can be integrated to obtain

$$\phi_r = gz + \int_0^z gf(z')dz'$$

or in terms of N_r^2

$$\phi_r = gz + \int_0^z dz' \int_0^{z'} N_r^2(z'')dz''. \tag{2.18}$$

We now non-dimensionalize the primitive equations so the Rossby number dependence appears explicitly. Let H be the depth of the troposphere. We then define the non-dimensional variables $\tilde{u} = u/U$, $\tilde{v} = v/U$, $\tilde{w} = wL/(UH)$, $\tilde{x} = x/L$, $\tilde{y} = y/L$, $\tilde{z} = z/H$, $\tilde{t} = tU/L$ and $\tilde{\Phi} = \Phi/(UfL)$.

Equation (2.10) can then be nondimensionalized as follows. The total geopotential $\Phi = \phi_r + \phi$, where ϕ represents the geopotential of the moving fluid, hereafter called the flow geopotential. Focusing on the vertical advèction term we have

$$w\frac{\partial^2 \Phi}{\partial z^2} = w\frac{\partial^2 \phi_r}{\partial z^2} + w\frac{\partial^2 \phi}{\partial z^2} \tag{2.19}$$

$$= wN_r^2(z)\left(1 + \frac{1}{N_r^2(z)}\frac{\partial^2 \phi}{\partial z^2}\right) \tag{2.20}$$

$$= wN_r^2(z)\left(1 + \frac{UfL}{N_r^2(z)H^2}\frac{\partial^2 \tilde{\phi}}{\partial \tilde{z}^2}\right). \tag{2.21}$$

Letting the horizontal scale L = the Rossby radius of deformation $= N_r^* H/f$, where N_r^* is a characteristic value of N_r, equation (2.21) becomes

$$w\frac{\partial^2 \Phi}{\partial z^2} = wN_r^2(z)\left(1 + \frac{U}{N_r(z)H}\frac{N_r^*}{N_r(z)}\frac{\partial^2 \tilde{\phi}}{\partial \tilde{z}^2}\right) \tag{2.22}$$

$$= wN_r^2(z)\left(1 + \epsilon g(z)\frac{\partial^2 \tilde{\phi}}{\partial \tilde{z}^2}\right), \tag{2.23}$$

where $U/N_r^* H = \epsilon$ and $g(z) = (N_r^*)^2/N_r^2(z)$ is a function of order unity throughout the troposphere.

Inserting the dimensionless variables and using equation (2.23), the thermodynamic equation becomes

$$\epsilon\left(\frac{\partial}{\partial\tilde{t}} + \tilde{u}\frac{\partial}{\partial\tilde{x}} + \tilde{v}\frac{\partial}{\partial\tilde{y}}\right)\frac{\partial\tilde{\phi}}{\partial\tilde{z}} + \frac{\tilde{N}_r^2(\tilde{z})}{(N_r^*)^2}\tilde{w}\left(1 + \epsilon\tilde{g}(\tilde{z})\frac{\partial^2\tilde{\phi}}{\partial\tilde{z}^2}\right) = 0$$

or

$$\epsilon\left(\frac{\partial}{\partial\tilde{t}} + \tilde{u}\frac{\partial}{\partial\tilde{x}} + \tilde{v}\frac{\partial}{\partial\tilde{y}}\right)\frac{\partial\tilde{\phi}}{\partial\tilde{z}} + N_0^2(\tilde{z})\tilde{w}\left(1 + \epsilon\tilde{g}(\tilde{z})\frac{\partial^2\tilde{\phi}}{\partial\tilde{z}^2}\right) = 0, \tag{2.24}$$

where $\tilde{N}_r^2(\tilde{z})$ is the static stability in terms of $\tilde{z}$ and $N_0^2(\tilde{z}) = \tilde{N}_r^2(\tilde{z})/(N_r^*)^2$ is the reference static stability normalized by $(N_r^*)^2$.

The x-momentum equation can be written

$$\epsilon\left(\frac{\partial\tilde{u}}{\partial\tilde{t}} + \tilde{u}\frac{\partial\tilde{u}}{\partial\tilde{x}} + \tilde{v}\frac{\partial\tilde{u}}{\partial\tilde{y}} + \tilde{w}\frac{\partial\tilde{u}}{\partial\tilde{z}}\right) - \tilde{v} = -\frac{\partial\tilde{\phi}}{\partial\tilde{x}}, \tag{2.25}$$

and the y-momentum equation is

$$\epsilon\left(\frac{\partial\tilde{v}}{\partial\tilde{t}} + \tilde{u}\frac{\partial\tilde{v}}{\partial\tilde{x}} + \tilde{v}\frac{\partial\tilde{v}}{\partial\tilde{y}} + \tilde{w}\frac{\partial\tilde{v}}{\partial\tilde{z}}\right) + \tilde{u} = -\frac{\partial\tilde{\phi}}{\partial\tilde{y}}. \tag{2.26}$$

We now expand $\tilde{u}$, $\tilde{v}$, $\tilde{\phi}$ and $\tilde{w}$ as Taylor series in ϵ. Dropping tildes we write

$$u = u(x,y,t;\epsilon) = u(x,y,t;0) + \frac{\partial u}{\partial\epsilon}(x,y,t;0)\cdot\epsilon + \frac{\partial^2 u}{\partial\epsilon^2}(x,y,t;0)\cdot\frac{\epsilon^2}{2} + \ldots \equiv u_0 + u_1\epsilon + u_2\epsilon^2 + \ldots, \tag{2.27}$$

$$v = v(x,y,t;\epsilon) = v(x,y,t;0) + \frac{\partial v}{\partial\epsilon}(x,y,t;0)\cdot\epsilon + \frac{\partial^2 v}{\partial\epsilon^2}(x,y,t;0)\cdot\frac{\epsilon^2}{2} + \ldots \equiv v_0 + v_1\epsilon + v_2\epsilon^2 + \ldots, \tag{2.28}$$

$$\phi = \phi(x,y,t;\epsilon) = \phi(x,y,t;0) + \frac{\partial\phi}{\partial\epsilon}(x,y,t;0)\cdot\epsilon + \frac{\partial^2\phi}{\partial\epsilon^2}(x,y,t;0)\cdot\frac{\epsilon^2}{2} + \ldots \equiv \phi_0 + \phi_1\epsilon + \phi_2\epsilon^2 + \ldots, \tag{2.29}$$

$$w = w(x,y,t;\epsilon) = w(x,y,t;0) + \frac{\partial w}{\partial\epsilon}(x,y,t;0)\cdot\epsilon + \frac{\partial^2 w}{\partial\epsilon^2}(x,y,t;0)\cdot\frac{\epsilon^2}{2} + \ldots \equiv w_0 + w_1\epsilon + w_2\epsilon^2 + \ldots \tag{2.30}$$

At zeroth order in ϵ, the momentum equations give

$$v_0 = \frac{\partial\phi_0}{\partial x} \tag{2.31}$$

and

$$u_0 = -\frac{\partial \phi_0}{\partial y}, \tag{2.32}$$

from which

$$\frac{\partial u_0}{\partial x} + \frac{\partial v_0}{\partial y} = 0. \tag{2.33}$$

Thus u_0 and v_0 are the geostrophic winds. The continuity equation at zeroth order then gives

$$\frac{\partial w_0}{\partial z} = 0. \tag{2.34}$$

Integrating this equation in z and invoking the boundary condition that $w = 0$ at $z = 0$ yields $w_0 \equiv 0$.

The order ϵ thermodynamic equation is

$$\frac{D_g}{Dt}\frac{\partial \phi_0}{\partial z} + w_1 N_0^2 = 0 \tag{2.35}$$

where

$$\frac{D_g}{Dt} = \frac{\partial}{\partial t} + u_0\frac{\partial}{\partial x} + v_0\frac{\partial}{\partial y}.$$

The order ϵ continuity equation is

$$\frac{\partial u_1}{\partial x} + \frac{\partial v_1}{\partial y} = -\frac{1}{\rho_*}\frac{\partial(\rho_* w_1)}{\partial z}. \tag{2.36}$$

The order ϵ momentum equations are

$$\frac{\partial u_0}{\partial t} + u_0\frac{\partial u_0}{\partial x} + v_0\frac{\partial u_0}{\partial y} - v_1 = -\frac{\partial \phi_1}{\partial x} \tag{2.37}$$

and

$$\frac{\partial v_0}{\partial t} + u_0\frac{\partial v_0}{\partial x} + v_0\frac{\partial v_0}{\partial y} + u_1 = -\frac{\partial \phi_1}{\partial y}. \tag{2.38}$$

Taking $\partial(2.38)/\partial x - \partial(2.37)/\partial y$, we find

$$\left(\frac{\partial}{\partial t} + u_0\frac{\partial}{\partial x} + v_0\frac{\partial}{\partial y}\right)\left(\frac{\partial v_o}{\partial x} - \frac{\partial u_0}{\partial y}\right) + \left(\frac{\partial u_1}{\partial x} + \frac{\partial v_1}{\partial y}\right) = 0. \tag{2.39}$$

Equations (2.35), (2.36), and (2.39) can be combined to obtain

$$\left(\frac{\partial}{\partial t} + u_0\frac{\partial}{\partial x} + v_0\frac{\partial}{\partial y}\right)\left[\frac{\partial v_0}{\partial x} - \frac{\partial u_0}{\partial y} + \frac{1}{\rho_*}\frac{\partial}{\partial z}\left(\frac{\rho_*}{N_0^2}\frac{\partial \phi_0}{\partial z}\right)\right] = 0 \tag{2.40}$$

which we write as

$$\frac{D_g Q_g}{Dt} = 0 \tag{2.41}$$

where

$$Q_g \equiv \frac{\partial v_0}{\partial x} - \frac{\partial u_0}{\partial y} + \frac{1}{\rho_*}\frac{\partial}{\partial z}\left(\frac{\rho_*}{N_0^2}\frac{\partial \phi_0}{\partial z}\right) \tag{2.42}$$

is the QG PV minus f.

From equation (2.42), using equations (2.31) and (2.32), we also find

$$Q_g = \frac{\partial^2 \phi_0}{\partial x^2} + \frac{\partial^2 \phi_0}{\partial y^2} + \frac{1}{\rho_*}\frac{\partial}{\partial z}\left(\frac{\rho_*}{N_0^2}\frac{\partial \phi_0}{\partial z}\right). \tag{2.43}$$

This equation, which relates the QG PV (minus f) to derivatives of the geopotential, is called the QG invertibility relation.

In dimensional form, the PV conservation equation, the thermodynamic equation and the invertibility equation take the form

$$\frac{D_g Q_g}{Dt} = 0, \tag{2.44}$$

$$\frac{D_g}{Dt}\left(\frac{\partial \phi_0}{\partial z}\right) + w_1 N_r^2(z) = 0, \tag{2.45}$$

and

$$Q_g = \frac{1}{f}\frac{\partial^2 \phi_0}{\partial x^2} + \frac{1}{f}\frac{\partial^2 \phi_0}{\partial y^2} + \frac{1}{\rho_*}\frac{\partial}{\partial z}\left(\frac{f\rho_*}{N_r^2}\frac{\partial \phi_0}{\partial z}\right) \tag{2.46}$$

Chapter 3

THE QUASIGEOSTROPHIC AND NONDIVERGENT BAROTROPIC MODELS

3.1 Introduction

Two numerical models, a three-dimensional quasigeostrophic model and a barotropic nondivergent model, were used in this study. The models are described here.

3.2 The Nondimensional QG Equations

We will assume that the static stability is uniform throughout the troposphere, and take $N^2 = (N_r^*)^2 = 10^{-4}$ s^{-2}, where N_r^* is the characteristic value of the resting state static stability defined in Chapter 2. Henceforth Q denotes the total QG PV, θ_0 is the potential temperature at the surface, $H = 10$ km is the depth of the model troposphere, and L is the Rossby radius $NH/f = 1000$ km. For convenience we solve equations (2.44), (2.45) and (2.46) in nondimensional form. Denoting nondimensional variables with tildes we let

$$(x, y, z, t) = (\tilde{x}L, \tilde{y}L, \tilde{z}H, \tilde{t}f^{-1}), \tag{3.1}$$

$$(v_x, v_y, w) = NH(\tilde{v}_x, \tilde{v}_y, \frac{H}{L}\tilde{w}), \tag{3.2}$$

$$(\Phi, \theta, Q) = (\tilde{\Phi}N^2H^2, \tilde{\theta}\frac{N^2H\theta_0}{g}, \tilde{Q}f). \tag{3.3}$$

Here (v_x, v_y, w) denote the zonal geostrophic, meridional geostrophic and vertical velocities, respectively. We also define $(r,\ \lambda)$ to be the cylindrical coordinates with $r = 0$ at the center of the initial azimuthal mean vortex on the lowest level and u and v to be the radial and tangential geostrophic velocities. Overbars denote azimuthal mean quantities

Quantity	To obtain dimensional quantity, multiply nondimensional quantity by
horizontal distance (x, y, r)	10^6 m
vertical distance (z)	10^4 m
time (t)	10^4 s
time period (T)	$\tau_{eddy} = 2.91$ days
horizontal velocity (u, v)	100 ms^{-1}
vertical velocity (w)	1 ms^{-1}
temperature (θ)	30 K
geopotential (ϕ)	10^4 J kg^{-1}
vertical vorticity (ζ)	10^{-4} s^{-1}
potential vorticity (Q)	$0.3 \cdot 10^{-6}$ m^2 s^{-1} K kg^{-1}

Table 3.1: Factors to be used in converting from nondimensional to dimensional units.

and primes represent departures from the azimuthal mean. Factors to be used in converting between nondimensional and dimensional quantities are shown in Table 3.1. The conversion of PV to MKS units assumes a near-surface density of 1 kg m^{-3}. Note also that T is used to indicate time periods in units of the initial eddy turnover time of the basic state vortex. The eddy turnover time of a vortex is defined here as $\tau_{eddy} \equiv 2\pi R_M / v_{max}$, where R_M is the RMW and v_{max} is the tangential wind at that radius. The eddy turnover time of our initial basic state vortex is $2.5 \cdot 10^5$ s or approximately 2.91 days.

In equation (2.46), we neglect the vertical variation of ρ, consistent with the Boussinesq approximation. We take

$$\tilde{\Phi} = \frac{\tilde{z}^2}{2} + \frac{g}{N^2 H}\tilde{z} + \tilde{\phi}.$$

The nondimensional invertibility equation becomes

$$\tilde{\nabla}_h^2 \tilde{\phi} + \frac{\partial^2 \tilde{\phi}}{\partial \tilde{z}^2} = \tilde{Q} - 1. \tag{3.4}$$

where

$$\tilde{\nabla}_h^2 = \frac{\partial^2}{\partial \tilde{x}^2} + \frac{\partial^2}{\partial \tilde{y}^2}$$

The nondimensional thermodynamic equation becomes

$$\frac{\tilde{D}_g}{D\tilde{t}} \frac{\partial \tilde{\phi}}{\partial \tilde{z}} + \tilde{w} = 0. \tag{3.5}$$

The nondimensional PV equation is

$$\frac{\tilde{D}_g \tilde{Q}}{D\tilde{t}} = 0. \tag{3.6}$$

3.3 QG Model Numerics

We now drop tildes and subscripts and use only nondimensional variables unless specified. Thus, unless otherwise specified $\mathbf{u} = (u,v)$ denotes the geostrophic wind.

Since analytical solutions of equations (3.4), (3.5), and (3.6) are generally not available, we solve them numerically on a set of discrete points in (x, y, z). The model begins by initializing the potential vorticity at all points in space, and the perturbation temperature $\theta = \partial\phi/\partial z$ on the boundaries z=0 and z=1. Next the invertibility equation is solved for ϕ using successive overrelaxation (Press 1992), requiring convergence to $1 \cdot 10^{-4}$ in the pointwise residual. This requirement corresponds to a tolerance of approximately 1 mm in the geopotential height at 500 mb. We verified that decreasing this tolerance from 10^{-4} to 10^{-5} did not affect our results. Given ϕ, one then calculates the geostrophic winds, which are used to horizontally advect Q and $\theta(z = 0, z = 1)$ by one time step. The invertibility relation is then solved again with the same convergence requirement, allowing another time step, and so forth until the desired number of time steps have been computed.

The numerical solution is subject to periodicity in both x and y directions. The additional boundary condition used in solving equation (3.4) is obtained by evaluating the thermodynamic equation on $(z = 0, z = 1)$ and invoking the condition $w = 0$ to furnish an evolution equation for θ on the horizontal boundaries. The updated values of θ are then used as Neumann boundary conditions for the solution of the invertibility relation. The predicted fields (Q, θ) are minimally corrected at each time step to insure solvability of the Neumann problem: solvability is equivalent to enforcing global conservation of quasigeostrophic potential vorticity.

Timestepping is performed by a two-step predictor-corrector Adams-Bashforth method (Gazdag 1976). The advective terms of equations (3.5) and (3.6) are calculated using fourth-order Arakawa advection (Arakawa 1966) with the sign correction as noted by

Orszag (1971) in order to minimize dispersion errors. All other derivatives employ second-order centered differences.

The vertical grid spacing $dz = 1.25$ km, corresponding to nine vertical levels. The horizontal grid spacing (dx, dy) is typically 13.9 km, corresponding to about 14 grid points inside the radius of maximum winds of the initial circular vortex, and a total of 144 $\times$ 144 total points in x and y. The Courant-Friedrichs-Lewy (CFL) condition then requires a time step less than or equal to $2.78 \cdot 10^3$ s. We generally used a time step a factor of four to eight smaller than the CFL limit. For the single cluster and midlevel cases (sections 4.4 and 4.5), we decreased the horizontal grid spacing to 7.5 km by increasing the number of (x, y, z) points in the model to 200 $\times$ 200 $\times$ 9 and shrinking the domain size from 2000 $\times$ 2000 $\times$ 10 km to 1500 $\times$ 1500 $\times$ 10 km.

The model also includes second-order horizontal diffusion of Q. Diffusion is added to remove small-scale PV associated with the potential enstrophy cascade. The value of the diffusion coefficient is based on two characteristic time scales, $1/2\ \tau_{eddy}$ and τ_{shear}. The characteristic shear time is calculated based on the inverse of the local radial shear in a circular vortex,

$$\tau_{shear} = \left(r \frac{d\bar{\Omega}}{dr} \right)^{-1}$$

where $\bar{\Omega} = \bar{v}(r)/r$ is the angular velocity of the circular vortex in geostrophic and hydrostatic balance. For our vortex the maximum radial shear occurs initially near $r = 0.15$ and has a dimensional value of $0.18 \cdot 10^{-4}$ s^{-1}. This yields a diffusivity based on the vortex shear of ν_{shear} = (horizontal grid spacing)$^2/\tau_{shear} = 3.5 \cdot 10^3$ m^{2}s^{-1}. Corresponding to $1/2\ \tau_{eddy}$ we find ν_{eddy} = (horizontal grid spacing)$^2/(\frac{1}{2}\tau_{eddy}) = 1.5 \cdot 10^3$ m^{2}s^{-1}. Table 3.2 lists the characteristic times and diffusion coefficients for these two cases. Based on these calculations and examination of the model results at small scales, we chose $\nu = 4.2 \cdot 10^2$ m^{2}s^{-1}, a factor of six smaller than the mean value of ν_{eddy} and ν_{shear}. The results presented below have been verified to be insensitive to the precise value of ν used as long as PV with scales on the order of the grid spacing is removed rather than being allowed to accumulate.

	Characteristic Time	Diffusion Coefficient
$\frac{1}{2}\tau_{eddy}$	$1.2 \cdot 10^5$ s	$1.5 \cdot 10^3$ m^{2}s^{-1}
τ_{shear}	$5.6 \cdot 10^4$ s	$3.5 \cdot 10^3$ m^{2}s^{-1}

Table 3.2: Characteristic times and horizontal diffusion coefficients based on the initial circular vortex, possessing maximum tangential winds of 5 ms^{-1}, radius of maximum winds at 200 km and a grid spacing of 13.9 km.

We tested our principal results for sensitivity to the time step size and the required convergence tolerance of the invertibility solver. No sensitivity to these parameters was found.

3.4 Lagrangian Trajectories

As we will see in Chapter 4, a great deal can be learned about our model systems just from the fields of interest (PV, vorticity, geopotential and vertical velocity), which are output by the model about six times per model run (typically at $T = 0$, 0.5 τ_E, τ_E, 1.5 τ_E, 2 τ_E and 2.5 τ_E). From the output fields we can obtain contour plots at each output time, as well as azimuthal means and asymmetries of the fields.

To further elucidate the lateral mixing processes taking place within the vortex, another diagnostic model was created. This model tracks Lagrangian trajectories of PV particles, small elements of fluid which have a fixed value of PV and are advected by the geostrophic wind. Note these are not the trajectories of actual fluid parcels which are advected by the total wind. The "forward tracking" algorithm finds the end location of a particle with a given *initial* location at $t = 0$ after a given amount of time (typically the model run time) has passed. The "backward tracking" algorithm finds, for a particle at a given location *after* the model has run, the location from which the particle originated at $t = 0$. Examples of problems which can be investigated with these algorithms are given in Chapter 4.

To show how the trajectory algorithms are implemented, we first discuss forward tracking. We consider the inital-value problem

$$\frac{dx_i}{dt} = u(x_i, y_i, t) \tag{3.7}$$

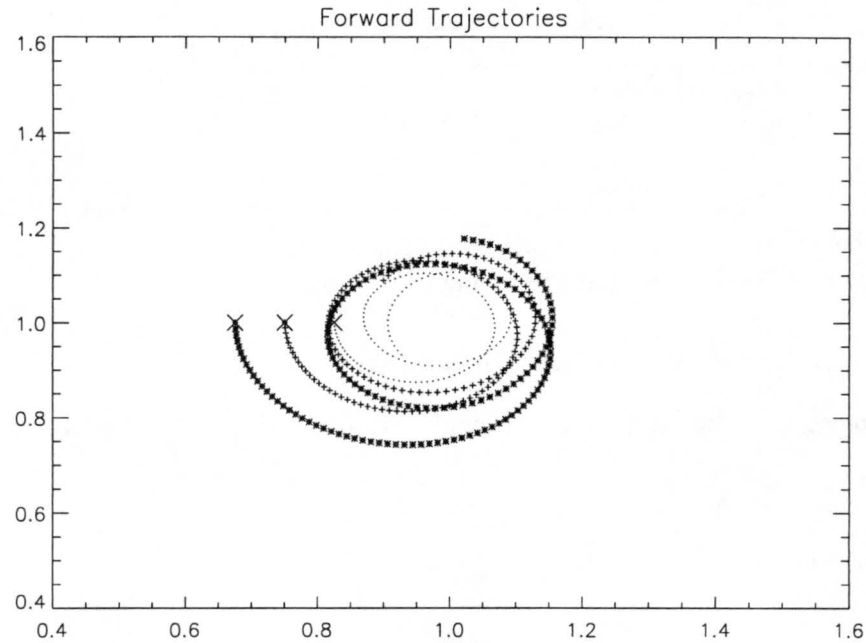

Figure 3.1: An example of the Lagrangian trajectories for three particles originating on the positive PV anomaly of the barotropic wavenumber two model run. X's depict the initial locations of the particles.

$$\frac{dy_i}{dt} = v(x_i, y_i, t) \tag{3.8}$$

for the i'th PV particle, where u and v are the x and y velocity fields calculated by the model, and $x_i(0) = \alpha$ and $y_i(0) = \beta$ are given. Thus, for each of the i PV particles we have a pair of coupled differential equations, which we wish to solve for $x_i(t)$ and $y_i(t)$.

The equations are solved by fourth order Runge-Kutta integration (Burden and Faires 1989, Abramowitz and Stegun 1972). To calculate the right-hand sides of equations (3.7) - (3.8), gridded velocity fields at a chosen z level are output from the QG3D model at each time step. The values of $u(x_i, y_i, t)$ and $v(x_i, y_i, t)$ are obtained from the gridded velocities by bilinear interpolation.

Model output is typically a plot of the trajectories in the (x,y) plane at the chosen model level. An example is displayed in Figure 3.1, which shows trajectories for three particles initially located near one of the positive PV anomalies in a barotropic wavenumber two model run.

Backward trajectories are only slightly more complicated. The Runge-Kutta algorithm must step through the velocity fields from the end ($t = 2\frac{1}{2}\tau_E$) of the file to its beginning at $t = 0$. Because the trajectories are time-reversed (analogous to running a movie backwards) the velocity vectors must also be reversed.

3.5 The Barotropic Nondivergent Model

The fully nonlinear barotropic wavenumber two simulation described in section 4.2 was performed with a semispectral model based on the two-dimensional nondivergent barotropic vorticity equation on an f-plane. Although the nondivergent vorticity equation can be simulated with the quasigeostrophic model by simplifying to barotropic dynamics and interpreting ϕ as the streamfunction, comparatively higher temporal and spatial resolution can be obtained with the semispectral model of MK extended to include the nonlinear advective terms. In the nondivergent model the perturbation streamfunction ψ' and the perturbation relative vorticity ζ' are represented semispectrally:

$$\psi'(r,\lambda,t) = \sum_{l=-N}^{N} \hat{\psi}_l(r,t) e^{il\lambda} \tag{3.9}$$

and

$$\zeta'(r,\lambda,t) = \sum_{m=-N}^{N} \hat{\zeta}_m(r,t) e^{im\lambda}, \tag{3.10}$$

where $\hat{\psi}_l$ and $\hat{\zeta}_m$ denote the azimuthal Fourier amplitudes for streamfunction and vorticity respectively and an azimuthal wavenumber truncation of N = 8 is used for the example considered. The dimensional prognostic equation for the streamfunction is

$$\frac{\partial \hat{\psi}_n}{\partial t} = \nabla_n^{-2} \hat{F}_n(r,t) \tag{3.11}$$

where

$$\hat{F}_n(r,t) = \frac{1}{r}\left\{ \sum_{\substack{|k|\le N \\ |n-k|\le N}} \left[ik\frac{\partial}{\partial r}(\hat{\psi}_k \hat{\zeta}_{n-k}) - in\hat{\zeta}_{n-k}\frac{\partial \hat{\psi}_k}{\partial r} \right] + in\frac{d\bar{\zeta}}{dr}\hat{\psi}_n - in\frac{d\bar{\psi}}{dr}\hat{\zeta}_n \right\} + \nu\nabla_n^2\hat{\zeta}_n, \tag{3.12}$$

$n \neq k$ and $\nabla_n^2 = (1/r)\partial/\partial r + \partial^2/\partial r^2 - n^2/r^2$. A diffusion coefficient ν of 20 $m^2 s^{-1}$ is used for this simulation. The inversion is carried out using a standard tri-diagonal solver.

Radial derivatives are computed with centered second-order differences. Timestepping is performed using a fourth-order Runge-Kutta scheme (Abramowitz and Stegun 1972). The radial grid spacing is 8.5 km, with 200 radial points.

3.6 The Basic State Vortices

For our first three examples the initial flow consists of a barotropic, circular vortex superposed with either of three types of perturbation asymmetries. The initial circular vortex for the barotropic simulation is the same as that used in the nondivergent calculations of MK (section 2). The basic state circular vortex for the three-dimensional model is defined by the PV field

$$Q_{basic}(x, y, z) = 1 + \alpha_0 e^{-\beta_0 r_o^2}, \tag{3.13}$$

where

$$r_o^2 = (x - x_c)^2 + (y - y_c)^2, \tag{3.14}$$

(x_c, y_c) is the center of the vortex, and parameters such as α_0 and β_0 are listed in Table 3.3. For both cases the basic state vortex has an RMW of 0.2 (200 km), and a maximum tangential wind of 0.05 (5.0 ms^{-1}). Future work should investigate the precise thresholds of basic state vortex strength and areal extent required for the cyclogenesis process described here to occur. The maximum pressure drop associated with this initial basic state vortex in the three-dimensional model is 2.7 mb. Figure 3.2 shows the corresponding radial profiles of the azimuthal mean PV, azimuthal mean vorticity, azimuthal mean flow geopotential and azimuthal mean tangential wind for the three-dimensional model basic state. In the three-dimensional model, to ensure compatibility with the doubly periodic boundary conditions the basic state PV has been adjusted so that the area integral of the anomalous basic state PV is zero. The adjustment is a small effect and amounts to the requirement that the net circulation in the horizontal plane is zero.

For our fourth example we consider the case of a basic state vortex which, rather than being barotropic, has maximum tangential winds at the middle z level. This configuration is of meteorological interest because, as noted in Chapter 1, our initial basic state vortex

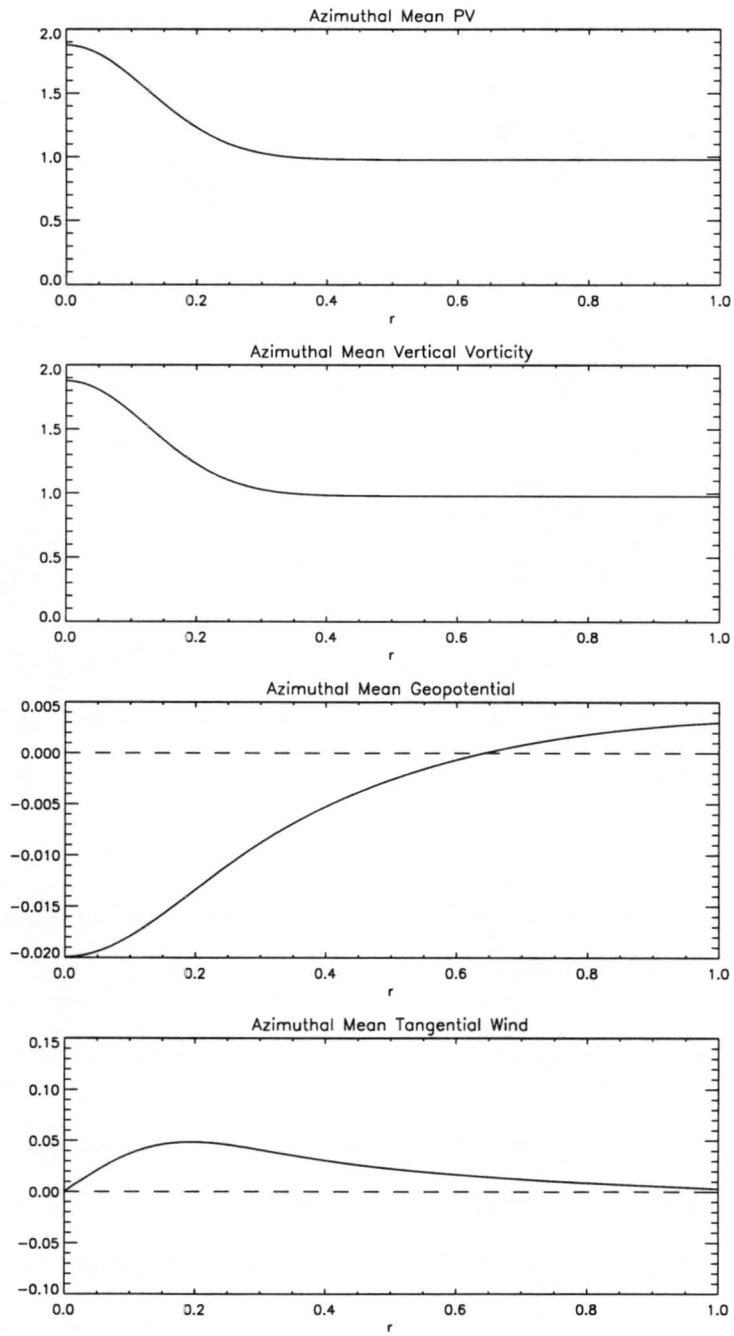

Figure 3.2: Radial profiles of the azimuthal mean potential vorticity, absolute vertical vorticity, flow geopotential and tangential wind for the basic state vortex. To obtain PV in 10^{-6} m^2 s^{-1} K kg^{-1}, multiply by 0.3. To obtain vorticity in s^{-1}, multiply by 10^{-4}. To obtain geopotential in J kg^{-1}, multiply by 10^4. To obtain tangential wind in ms^{-1}, multiply by 100.

Parameter	Value
α_0	0.900
α_1	4.12
α_2	1.00
α_3	1.00
β_0	32.0
β_1	128.
β_2	100.
β_3	100.
x_c	1.00
y_c	1.00
x_{c1}	1.25
y_{c1}	1.00
x_{c2}	0.75
y_{c2}	1.00

Table 3.3: Parameters describing the QG PV initialization.

could be a mesoscale convectively-generated vortex; MCVs typically have maximum tangential winds at midlevels (Johnston 1981, Bartels and Maddox 1991). To model such an initial flow we take

$$Q_{\text{midlevel}} = 1 + \alpha_0 e^{-\beta_0 r_0^2} \sin(\pi z).$$

The parameters α_0 and β_0 are listed in Table 3.3 and are the same as were used for the barotropic basic state vortex.

3.7 Physical Description of Convection in the QG Model

Although it is obviously not possible to resolve convective-scale dynamics (e.g. Weisman et al. 1993, Trier et al. 1997) in a quasigeostrophic model, the approach taken here is a phenomenological one whereby the vertical vorticity budget of an incipient vortex and an ensemble of convective cells is parameterized by potential vorticity anomalies having a horizontal scale of approximately 200 km. Neglecting internal friction, Ertel's PV equation based on dry potential temperature is

$$\frac{DQ}{Dt} = \frac{\zeta_a \cdot \nabla \dot{\theta}}{\rho},$$

where ζ_a is the absolute vorticity, ρ is the density and $\dot{\theta}$ is the heating rate associated with cumulus convection. In the QG Boussinesq approximation, only the vertical component of $\zeta_a \cdot \nabla\dot{\theta}$ is assumed significant, and the density is treated as constant yielding

$$\frac{DQ}{Dt} \approx \frac{(f+\zeta)}{\rho}\frac{\partial\dot{\theta}}{\partial z}, \tag{3.15}$$

where ζ is the magnitude of the vertical relative vorticity. Although the strict QG approximation would neglect ζ compared to f in equation (3.15), we retain both components of the vorticity for these numerical estimates.

Since realistic convective heating profiles have $\partial\dot{\theta}/\partial z$ greater than zero at low levels and less than zero at high levels, convection is seen to create a positive PV anomaly at low levels and a negative PV anomaly aloft. Since $\dot{\theta}$ is assumed zero at the horizontal boundaries, (i.e. no explicit enthalpy fluxes at the ocean's surface), no PV is fluxed into the domain and consequently the mass-weighted integral of PV will not change (Hoskins et al. 1985; Section 7).

The magnitudes of the convectively induced PV anomalies can be determined if the heating rate is known. Convective heating rates for midlatitude convective systems have been studied both observationally and theoretically (Gallus and Johnson 1991, Hertenstein 1996); an appropriate value of $\dot{\theta}$ averaged over several convective cells is found to be $\dot{\theta}_{max} \approx 15$ Khr^{-1} or 360 Kd^{-1}. From recent radar observations of tropical mesoscale convective systems (Mapes and Houze 1995) one obtains an estimate for $\dot{\theta}$ of 190-380 Kd^{-1}. Assuming further that the convective heating rate depends on z as $\sin(\pi z/H_c)$, where H_c is the vertical scale, and that the incipient vortex has relative vorticity O(f), we find

$$\text{PV change} \approx \int_0^{6\text{ h}} \frac{2f\dot{\theta}_{max}}{\rho}\frac{\pi}{H_c}dt' \approx \text{1-2 PVU},$$

where one PVU = 10^{-6} m^2 s^{-1} K kg^{-1}. Here we have used $f = 5\cdot10^{-5}$ s^{-1}, $H_c = 15$ km, and taken ρ to be 1.0 kg m^{-3} for a realistic estimate of the magnitude of PV generation in the lower troposphere. As suggested by the observations of Zehr (1992) discussed in Chapter 6 and displayed in Figure 5.1, we integrate for a period of six hours corresponding to the bursts of convection shown in the figure. Although the peaks in the figure have a

duration of approximately 12 hours, we expect the lifetime of the cold-cloud tops to be longer than the time period during which heating is occurring.

The main vortex's PV can be estimated similarly:

$$\mathrm{PV}_{\text{main vortex}} \approx \frac{\zeta_a}{\rho}\frac{\partial\theta}{\partial z} \approx \frac{2f\theta_0 N^2}{g\rho} \approx 0.3 \text{ PVU}.$$

Thus, even being quite conservative, we see that the convective anomalies for our system can have roughly the same PV magnitude as the basic state vortex.

3.8 Initial PV Anomalies

For the nondivergent simulation, the basic state vortex is perturbed with a localized wavenumber two vorticity disturbance whose Fourier amplitude is given by

$$\hat{\zeta}_2(r) = \begin{cases} 0.20\ \bar{\zeta}(\mathrm{RMW})\sin^2\left(\frac{\pi(r-0.070)}{0.26}\right), & |r-\mathrm{RMW}| \le 0.13\ ; \\ 0, & |r-\mathrm{RMW}| > 0.13. \end{cases}$$

Here $\bar{\zeta}(\mathrm{RMW})$ is the azimuthal mean vorticity at the vortex's RMW and the parameters are chosen to give a maximum asymmetry at the RMW, where the physical space asymmetry amplitude is 40 % of the basic state amplitude. A map plot of the relative vorticity for this anomaly added to the basic state is shown in the initial condition of Figure 4.1.

The second and third asymmetries considered were intended to model the effects of an outbreak of convection near the initially circular vortex.

A PV anomaly that has approximately the same magnitude as the basic state vortex PV and has the desired property of adding positive PV at low levels and depleting it at upper levels while keeping the mass-weighted integral of PV unchanged is given by

$$Q_2'(x,y,z) = \alpha_2(e^{-\beta_2(\delta r_1)^2} + e^{-\beta_2(\delta r_2)^2})\cos(\pi z), \tag{3.16}$$

where $(\delta r_1)^2 = (x-x_{c1})^2+(y-y_{c1})^2$, $(\delta r_2)^2 = (x-x_{c2})^2+(y-y_{c2})^2$ and the parameters α_2, β_2,x_{c1}, x_{c2}, y_{c1} and y_{c2} are listed in Table 3.3. This configuration, called the two-cluster convective anomaly, has two regions of convection on opposite sides of the basic state vortex, at radii of 0.25 (250 km) from the center of the vortex. Contour plots of the PV, vorticity and flow geopotential for $Q_2 = Q_{basic} + Q_2'$ are shown in Figure 3.3. The top and

middle panels of Figure 3.4 show an x-cross section of the initial basic state compared to a similar cross section of the two-cluster convective anomaly. The maximum pressure drop of each positive anomaly associated with Q_2' is 1.0 mb (not shown), with a corresponding maximum tangential wind velocity of 3.0 ms^{-1} (not shown). The maximum temperature deviation from the resting basic state for Q_2' occurs at $z = 0.5$ and is approximately 0.75 K (not shown).

As a model for convection that is localized in one area we take

$$Q_3' = \alpha_3 e^{-\beta_3(\delta r_1)^2} \cos(\pi z) \tag{3.17}$$

and refer to this configuration as the single-cluster convective anomaly. Plots of the PV, vorticity and flow geopotential for $Q_3 = Q_{basic} + Q_3'$ are shown in Figure 3.5. An x-cross section of the single-cluster convective anomaly is shown in the bottom panel of Figure 3.4. The maximum pressure drop of the positive anomaly associated with Q_3' is 0.92 mb (not shown), with a corresponding maximum tangential wind of 2.8 ms^{-1} (not shown). The maximum temperature deviation from a resting basic state for the Q_3' anomaly occurs at $z = 0.5$ and is approximately 0.75 K (not shown).

When the negative anomalies associated with Q_2' and Q_3' are added to the basic state PV the total PV remains positive, thereby ensuring symmetric stability ($fQ > 0$) of the model atmosphere.

For the midlevel vortex example we used the same single-cluster convective anomaly as that described above. Thus the PV distribution for this example is given by $Q_4 = Q_{\text{midlevel}} + Q_3'$.

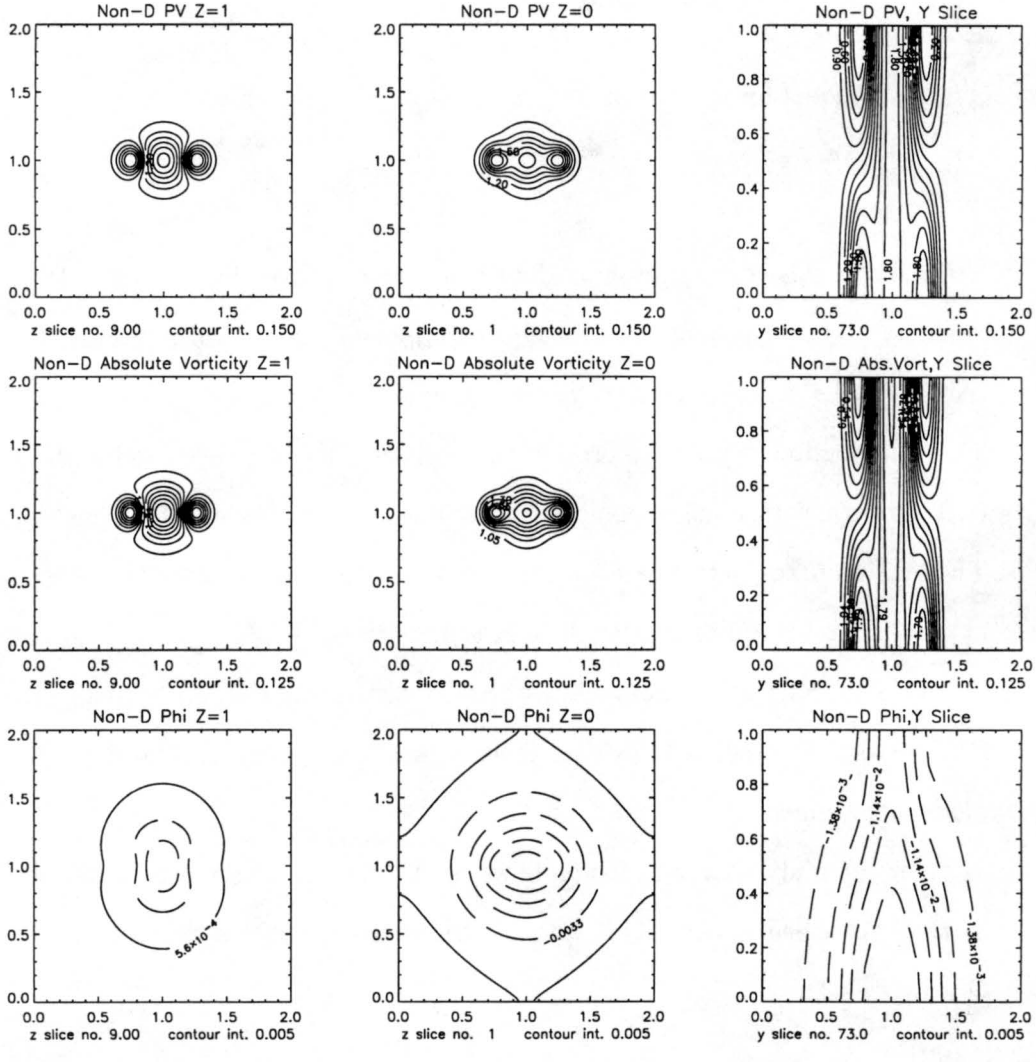

Figure 3.3: Initial nondimensional basic state vortex + baroclinic two-cluster PV, absolute vertical vorticity and flow geopotential at top (z=1), bottom (z=0) and y-slice along y=1.

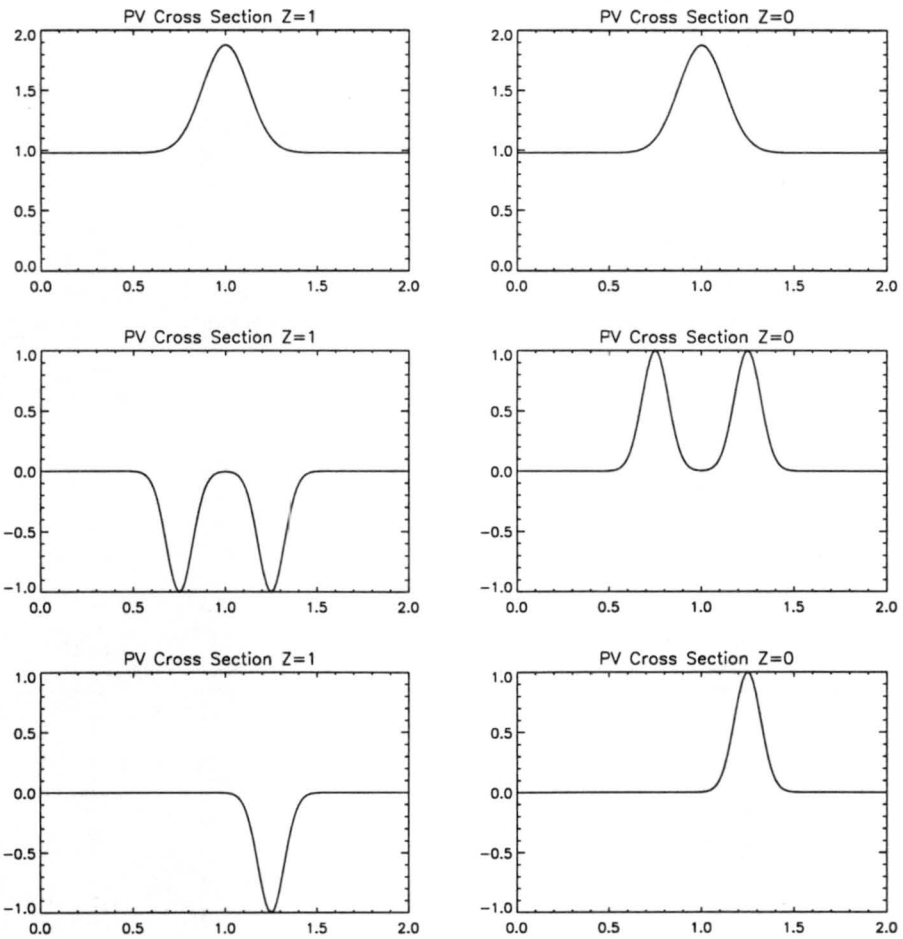

Figure 3.4: X-cross section of the initial basic state vortex PV (top panel), the initial two-cluster convective PV anomaly (middle panel), and the initial single-cluster convective PV anomaly (bottom panel).

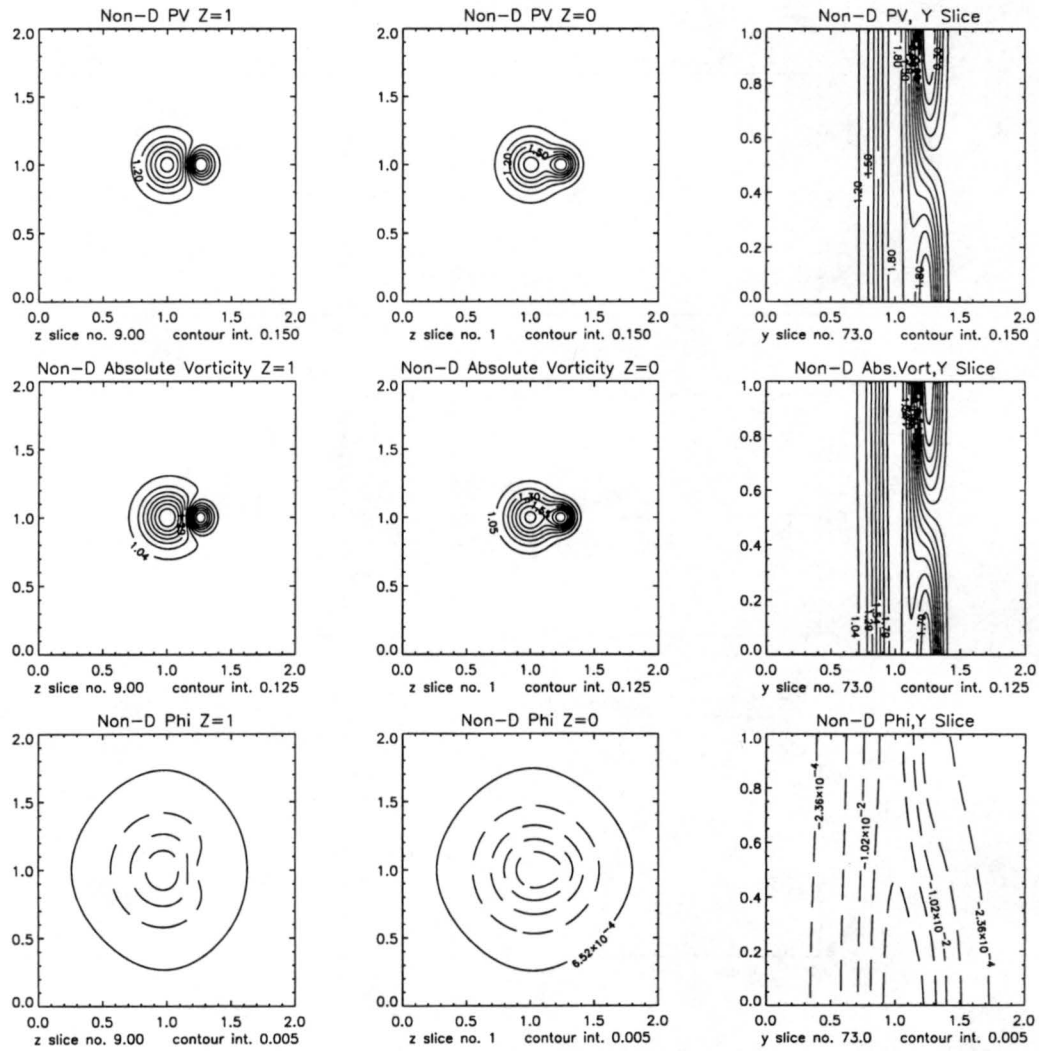

Figure 3.5: Initial nondimensional basic state vortex + baroclinic single-cluster PV, absolute vertical vorticity and flow geopotential at top (z=1), bottom (z=0) and y-slice along $y = 1$.

Chapter 4

FUNDAMENTALS OF THREE-DIMENSIONAL VORTEX AXISYMMETRIZATION

4.1 Introduction

To lay a conceptual foundation for the dynamics of ongoing moist convection in vortex shear flow, we study first the free adjustment or "relaxation" associated with finite-amplitude asymmetric PV anomalies near the radius of maximum winds of an incipient cyclonic vortex. The combination of a basic state barotropic circular vortex with three different asymmetries is analyzed in detail. The three representative examples are a barotropic wavenumber two anomaly and three-dimensional two-cluster and single-cluster anomalies which are intended to simulate the net effect of tropical convection. The problem of a midlevel vortex in the presence of convection is also considered.

4.2 The Barotropic Wavenumber Two Asymmetry

To validate the wave, mean-flow predictions of MK as well as to provide a conceptual foundation for the upcoming baroclinic experiments we first consider the relaxation of the initial barotropic wavenumber two anomaly. Figure 4.1 shows the evolution of the total and asymmetric relative vorticity for this case. Waves propagating both azimuthally and radially are clearly evident in the asymmetric vorticity. In particular, as the positive and negative vorticity perturbations are sheared into trailing spirals by the mean vortex the perturbations propagate outward. Excitation of secondary wave features in the interior of the vortex following the shearing of the initial asymmetries is also evident.

The axisymmetrizing wave disturbances evident in Figure 4.1 cannot be gravity waves since gravity waves are completely excised in the nondivergent model. Indeed, the waves

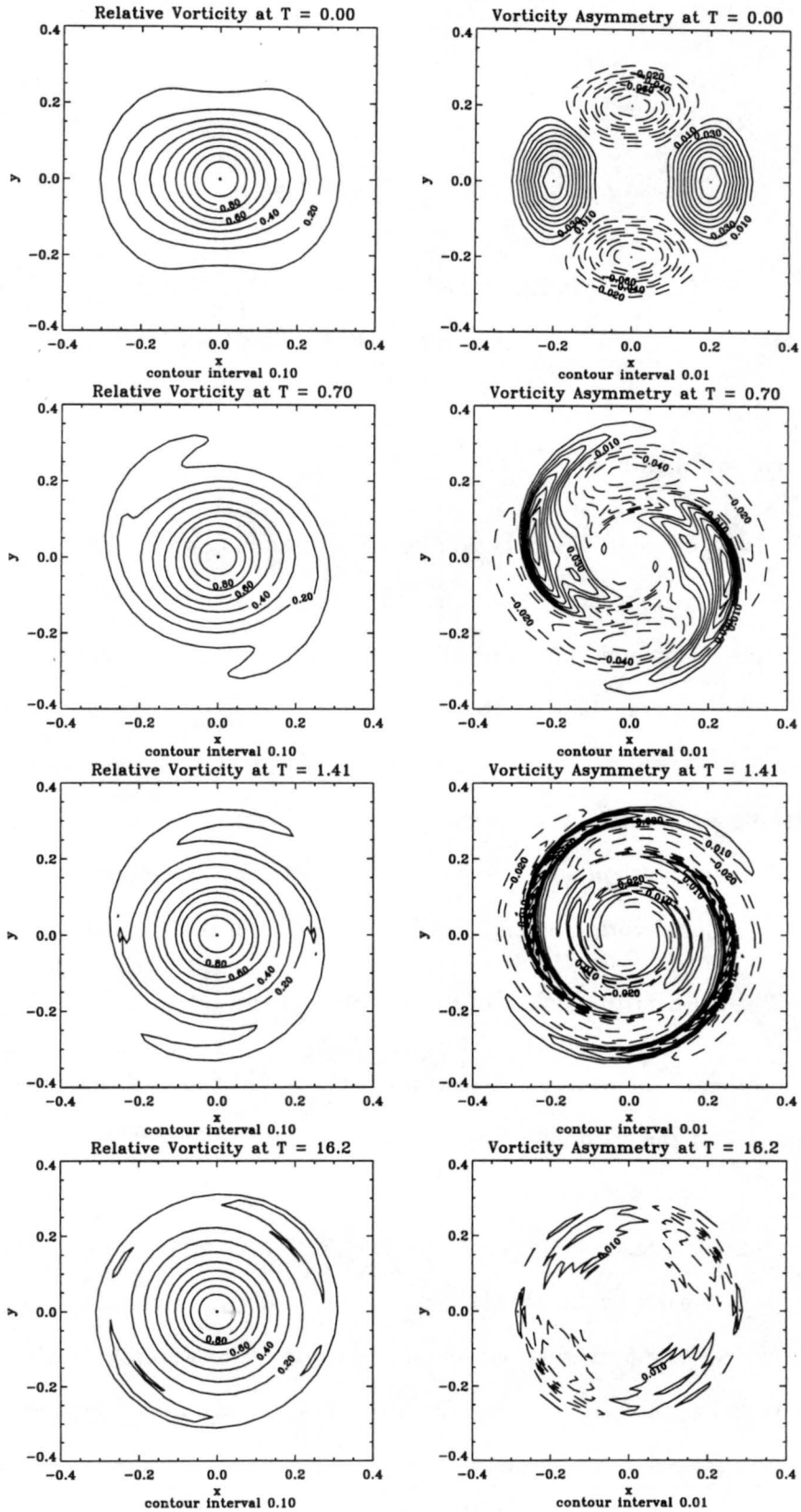

Figure 4.1: Evolution of the relative vertical vorticity and the relative vertical vorticity asymmetry for the barotropic wavenumber two simulation. Only the inner 800 km $\times$ 800 km of the model domain is shown.

are vortex Rossby waves whose restoring mechanism is associated with the radial gradient of basic state vortex vorticity. The basic theory for these waves was developed by MK. The radial group velocity for vortex Rossby wave packets in the WKB approximation is given by

$$C_{gr} = \frac{-2kn\bar{\zeta}_0'}{R_0(k^2 + \frac{n^2}{R_0^2})^2},$$

where n is the azimuthal wave number and $\bar{\zeta}_0'$ is the basic state radial vorticity gradient at reference radius $r = R_0$. The radial wavenumber k is given by $k(t) = k_0 - nt\bar{\Omega}_0'$, where k_0 is its initial value, and $\bar{\Omega}_0'$ is the radial gradient of the basic state angular velocity. Outside the RMW, our initially circularly symmetric anomaly will be deformed to a downshear-tilted patch. For downshear tilt $k_0 > 0$. Since for our vortex $\bar{\Omega}_0' < 0$, the initially positive k will grow more positive with time. If the relative vorticity gradient is negative, as is initially the case, C_{gr} will be positive and wave packets will propagate outward. In the upcoming examples using larger amplitude initial asymmetries, the outermost wave creates a region of positive mean vorticity gradient; in that region $C_{gr} < 0$ and wave packets propagate inward.

Figure 4.2 shows the wave-induced changes in azimuthal mean relative vorticity and tangential velocity. This figure can be compared with Figure 8 in MK; the results are in qualitative agreement. A notable feature of Figure 4.2 is the acceleration or "spinup" of the mean tangential winds and vorticity near the radius of the initial asymmetry. This spinup was predicted by MK; as we will see, it persists in the three-dimensional setting.

Although significant excitation of higher wavenumber components does occur, analysis of the wavenumber two vorticity component shows that the instantaneous wavenumber two packet propagates radially outward to a stagnation radius (r=0.27) very close to the zero in the $\delta\bar{v}$ plot. This qualitative behavior was predicted in the WKB framework of MK, and is consistent with the wave activity interpretation of Held and Phillips (1987) generalized to vortex flow. Quantitatively, the quasilinear prediction for $\delta\bar{v}(r)$ using the linear solutions to compute the eddy vorticity flux yields a $\delta\bar{v}_{max}$ of 0.10 ms^{-1}; the value observed in the nonlinear model is 0.09 ms^{-1}. The MK results, valid at second order in the wave amplitude, are still approximately valid. Thus the interaction of vortex Rossby

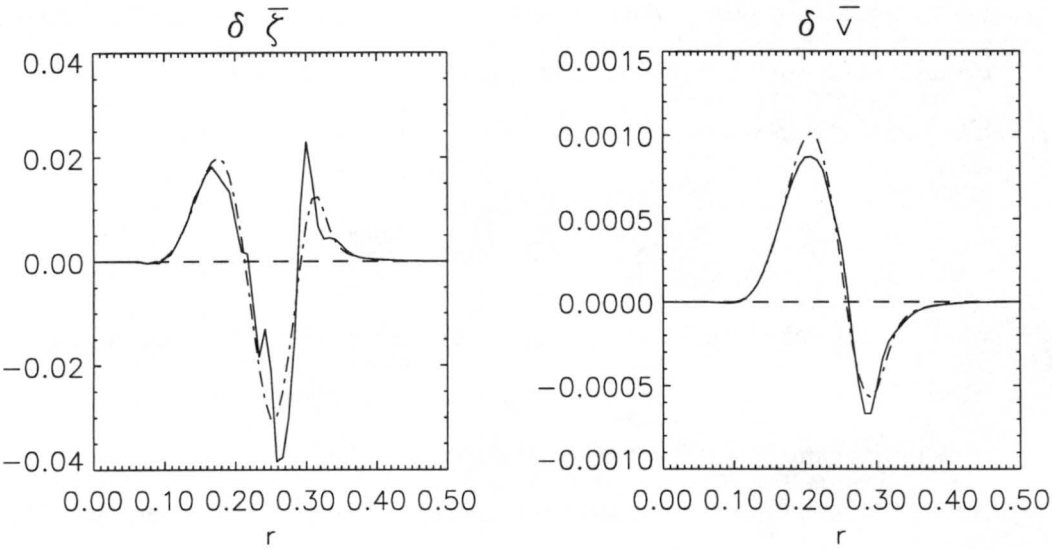

Figure 4.2: Change in the relative vertical vorticity and mean tangential wind at T=4 for the barotropic wavenumber two system. $\delta\bar{v}$ in ms^{-1} is obtained by multiplying by 100. Solid line shows the result of the fully nonlinear simulation and dashed line shows the quasilinear result.

waves with the mean flow captures the essence of the physics at these small but finite amplitudes. At higher amplitudes we find that wave-wave interactions play a more significant role.

As the initial asymmetry is sheared by the mean vortex some of the positive vorticity anomaly is transported towards the interior of the vortex. The remaining portion of the positive vorticity anomaly is transported outward to form the positive vorticity filaments which orbit the vortex core. The negative vorticity anomaly is also transported outward and becomes more nearly axisymmetric. Lagrangian trajectory analyses lend further support to these ideas about vorticity transport in the symmetrization process. A contour plot of the initial azimuthal mean vorticity subtracted from the total vorticity at T = 2.5 shows central regions of vorticity augmentation surrounded by spiral arms of vorticity depletion, with an outer region of vorticity augmentation as well. We studied Lagrangian back trajectories for particles destined to be found in each of these regions. Particles in the inner vorticity augmentation region were found to originate in the initial positive vorticity anomalies, in agreement with our understanding that positive vorticity from the anomalies moves inward and pools near the center of the vortex. Particles in the vorticity

depletion region backtracked to the initial vorticity depletion regions of the wavenumber two anomaly.

A nearly neutral discrete Rossby mode associated with a sign change of the radial vorticity gradient is visible in the barotropic experiment for $T \geq 4$. Such modes are discussed further in section 4.8.

4.3 The Two-Cluster Convective Anomaly

We consider next the two-cluster convective anomaly. Figures 4.3 - 4.5 show the fields of potential vorticity, vorticity and geopotential for top, middle and bottom z surfaces as a function of time. At the top level, the negative anomalies are expelled from the main vortex and are advected around the vortex. The negative anomalies do not axisymmetrize. At low z levels the behavior is similar to the barotropic case discussed above; the positive anomalies merge into the main vortex, with accompanying production of high-PV filaments, and again the vortex symmetrizes almost completely. However, due to the wave-induced change in the mean vorticity gradient shown below, neutral or weakly unstable modes are evident in the inner core region (see section 4.8).

Figure 4.6 shows the azimuthal mean and asymmetric PV as a function of time at the highest model level (z=1). Disturbances to the mean flow are evident. As noted earlier, the PV deficit regions move outward. Axisymmetrization does not occur at upper levels, however. The flow there resembles a vortex tripole (Polvani and Carton 1990, Orlandi and van Heijst 1992). From a linear wave viewpoint the tripole can be thought of as a finite amplitude wavenumber two discrete or weakly unstable vortex Rossby mode which is supported by a sign change in the mean radial PV gradient (see section 4.8).

On the middle level (see Figure 4.3) there is almost no change in the PV distribution; since PV is conserved following the geostrophic wind in our quasigeostrophic model, particles of higher or lower PV from the other levels cannot move to this level. However, PV can be advected on the $z = 0.5$ surface. The flow geopotential, consistent with the isothermal boundary conditions on $z = 0$ and $z = 1$ for the anomalies chosen here, can be written as a Fourier series

$$\phi = \sum_{m=0}^{\infty} \hat{\phi}_m(x, y, t) \cos(m\pi z),$$

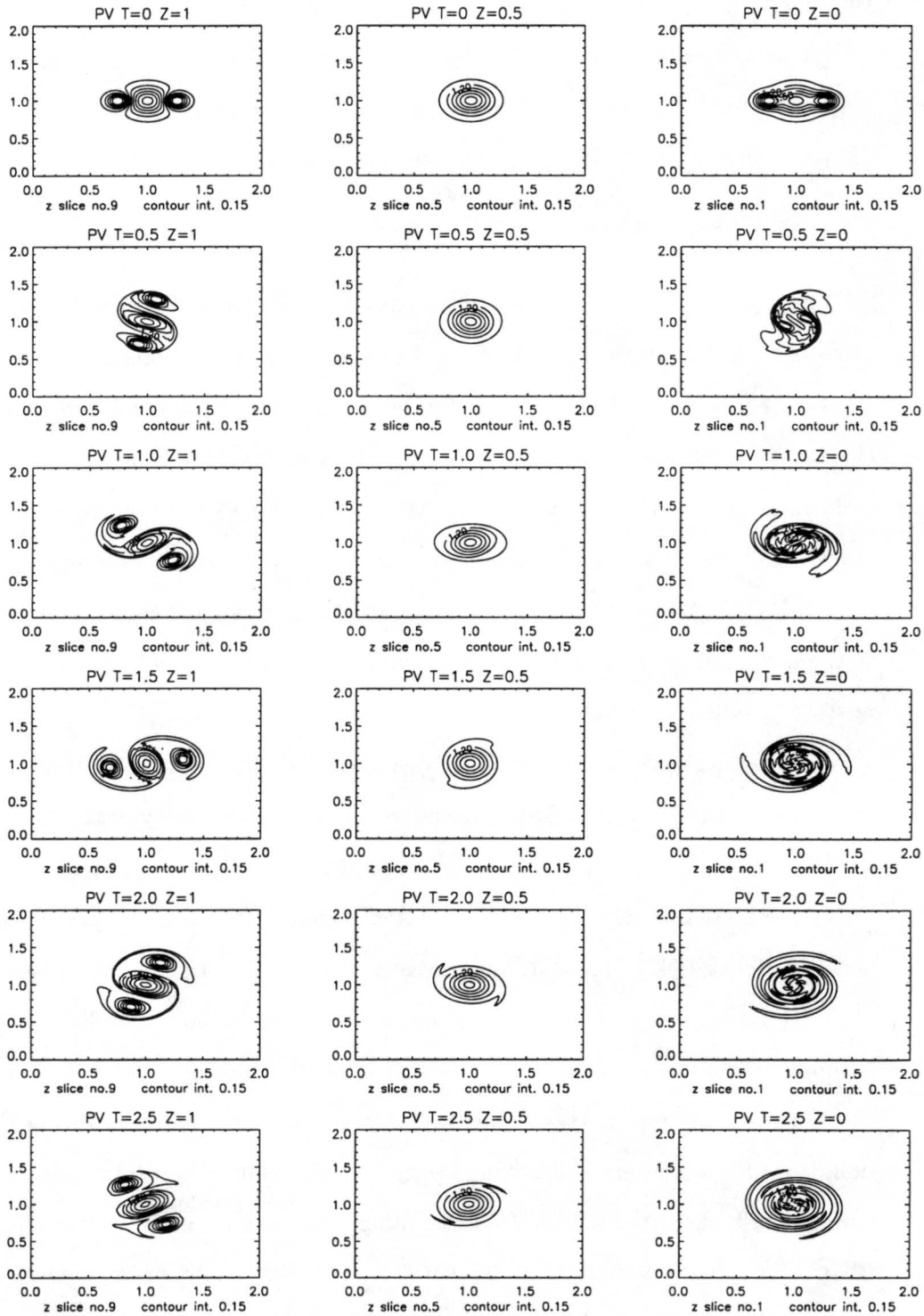

Figure 4.3: PV evolution for the two-cluster convective case at top, middle and bottom model levels.

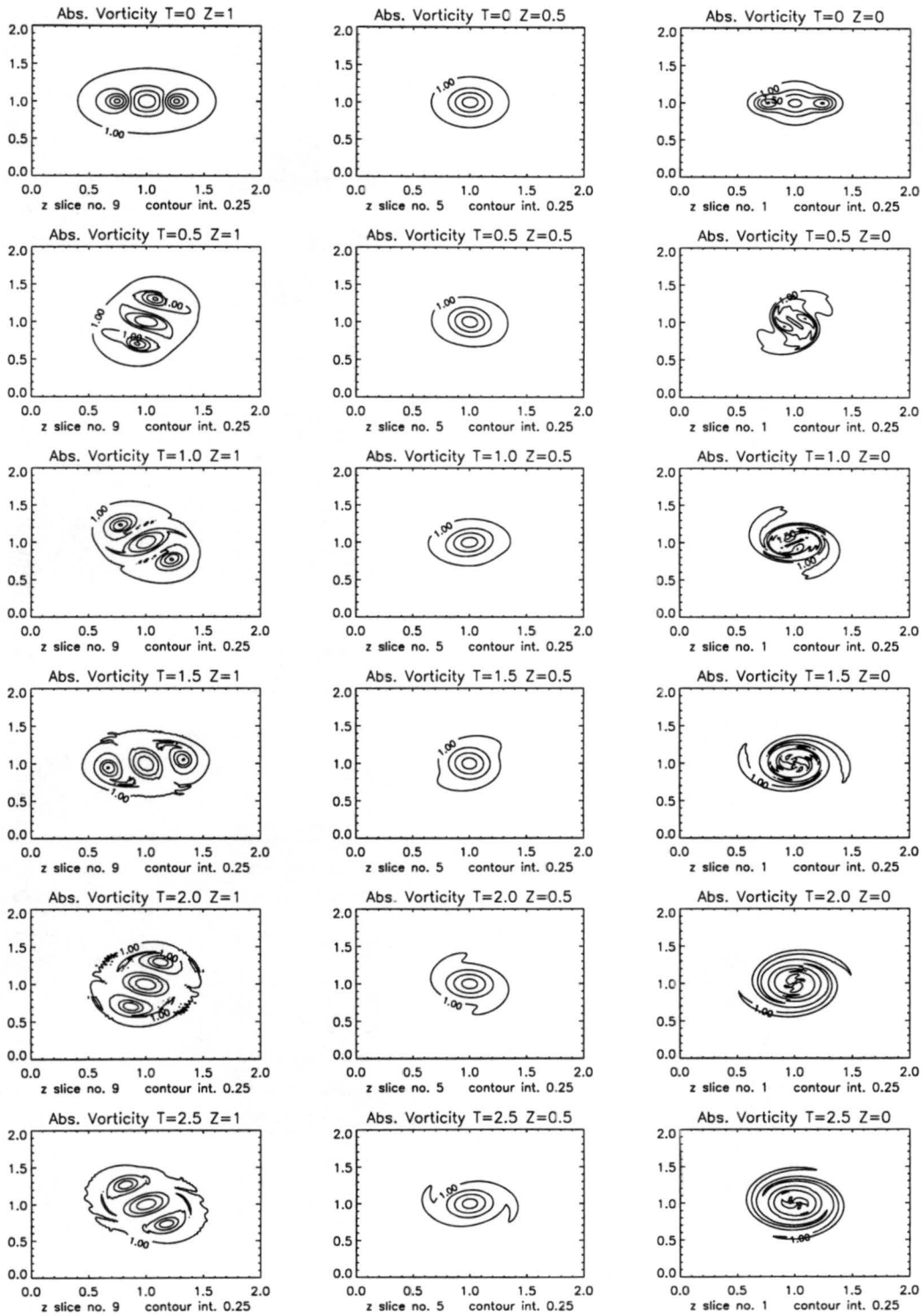

Figure 4.4: Evolution of the vorticity field for the two-cluster convective case at top, middle and bottom model levels.

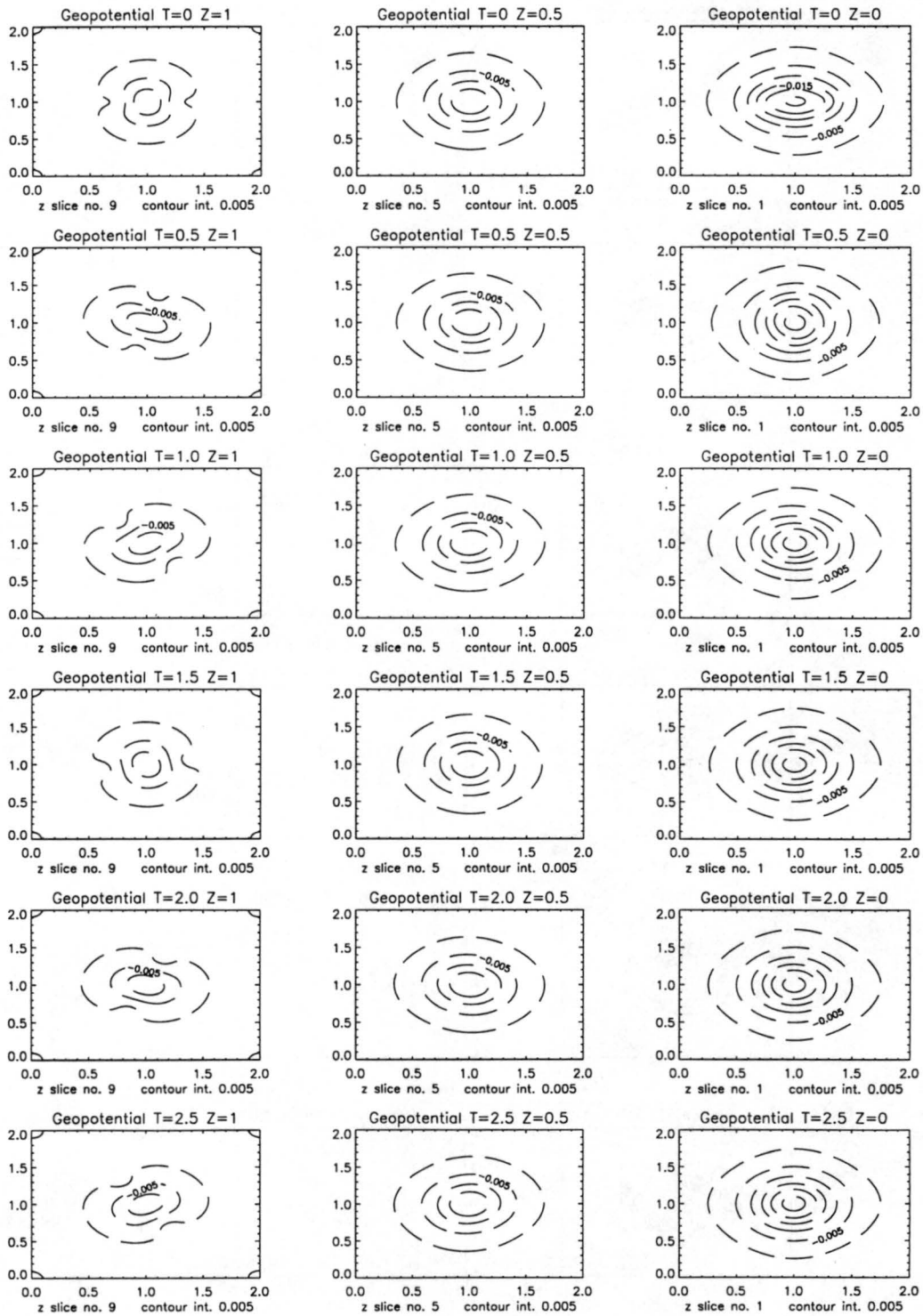

Figure 4.5: Evolution of the geopotential field for the two-cluster convective case at top, middle and bottom model levels.

where $\hat{\phi}_m$ denotes the m'th Fourier coefficient in the vertical. Initially we have contributions from $m = 0$ and $m = 1$. The $m = 0$ contribution comes from the barotropic basic state vortex, while the $m = 1$ contribution comes from the convectively-induced PV anomaly $\propto \cos \pi z$. Since

$$\frac{\partial Q}{\partial t} = -\mathbf{u} \cdot \nabla \mathrm{Q},$$

in general higher vertical modes of ϕ will be excited as the symmetrization proceeds, leading to advection of PV on the $z = 0.5$ level. In practice, for these experiments we see very little change in the PV on this level. This is evidence for the self-consistency of our using only nine levels in the vertical.

The bottom level (Figure 4.7) shows an increase in mean PV at a radius of approximately 0.1 (100 km), especially at earlier times. As in the barotropic case, there is an overall steepening of the PV gradient.

Figure 4.8 shows the evolution of the tangential velocity and the Rossby number with time at the bottom z surface. Figures 4.9(a) and (b) show the changes in the azimuthally averaged PV and tangential velocity at the bottom z surface. The similarity to the barotropic example (figure 4.2) is evident. The pooling of high PV at radius 0.125 (125 km) is evident. A spinup of 1.0 ms^{-1} occurs over the period of 1 τ_{eddy} (approximately 3 days). No further acceleration is observed after 1 τ_{eddy}.

In the double-cluster simulation, the stagnation radius of the initial wavenumber two wave packet is again approximately equal to the radius of the zero in the $\delta\bar{v}$ plot (r=0.3). Taking the primary azimuthal mode and its next two harmonics into account, the value of $\delta\bar{v}_{max}$ predicted by the quasilinear nondivergent theory is 0.94 ms^{-1}.

Forward Lagrangian trajectories for the two-cluster convective anomaly at the lowest model level have also been analyzed. Particles were placed randomly on a circle of radius 0.1 (approximately the size at half maximum of the positive anomaly) centered at the anomaly center. The results for a few selected particles are shown in Figure 4.9(c). Many of the particles move inward toward $r \approx 0.125$ (125 km). The others move outward to form the outer high-PV filaments. Trajectories at the highest level (not shown) were also analyzed. At this level, particles from the negative PV anomalies move generally

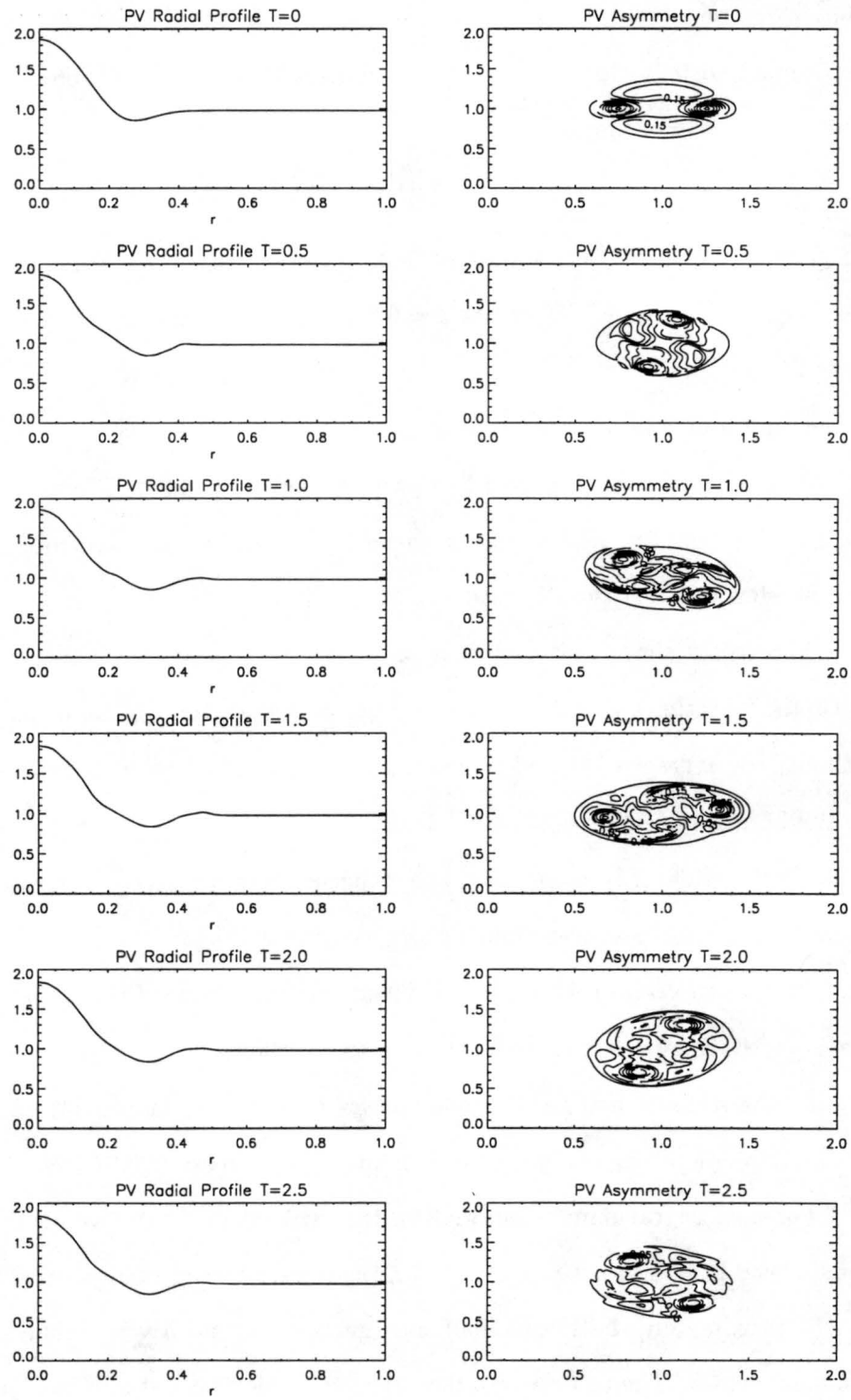

Figure 4.6: Evolution of the azimuthal mean PV and asymmetric PV for the two-cluster convective anomaly at the highest model level (z=1).

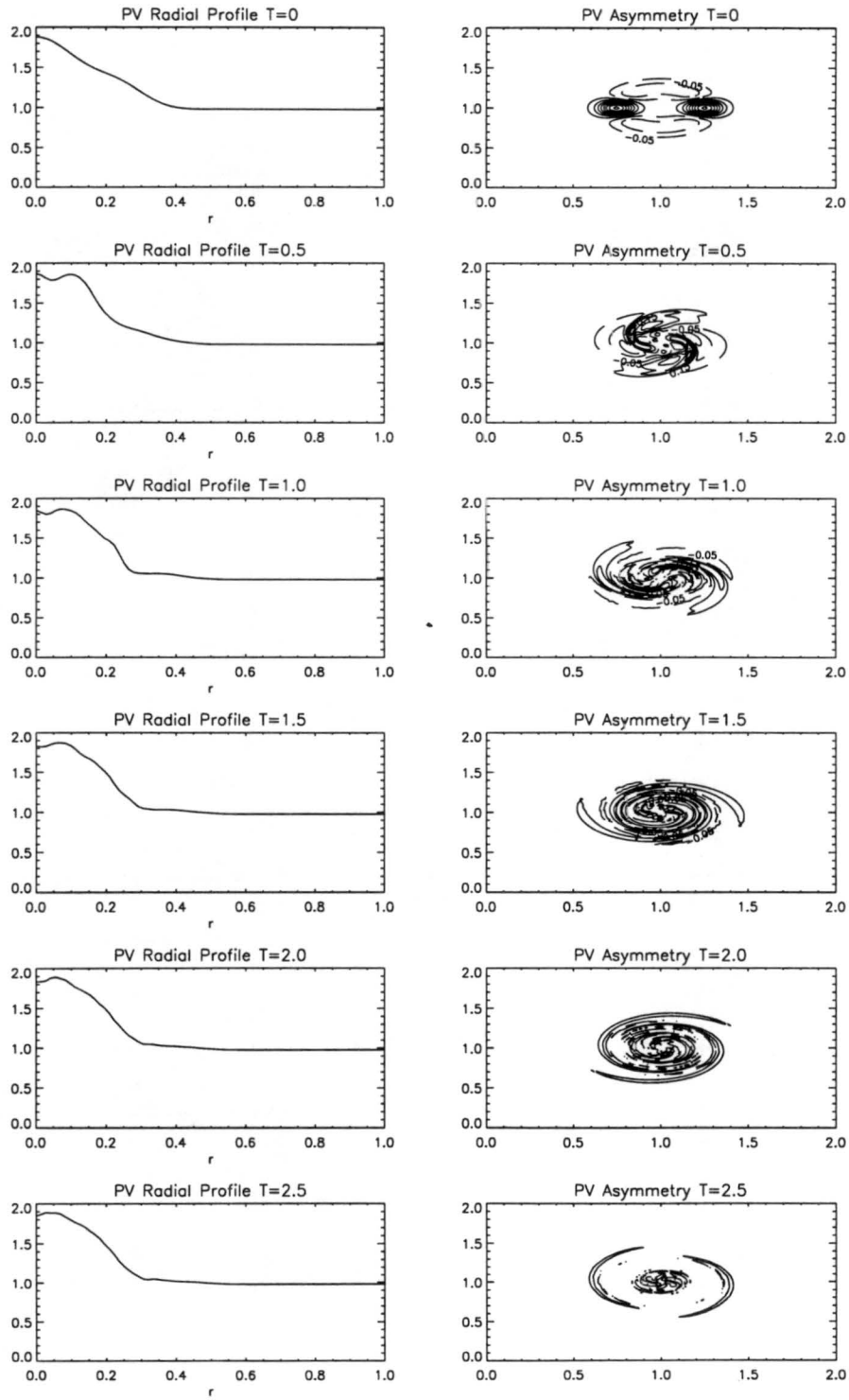

Figure 4.7: Evolution of the azimuthal mean PV and asymmetric PV for the two-cluster convective anomaly at the lowest model level (z=0).

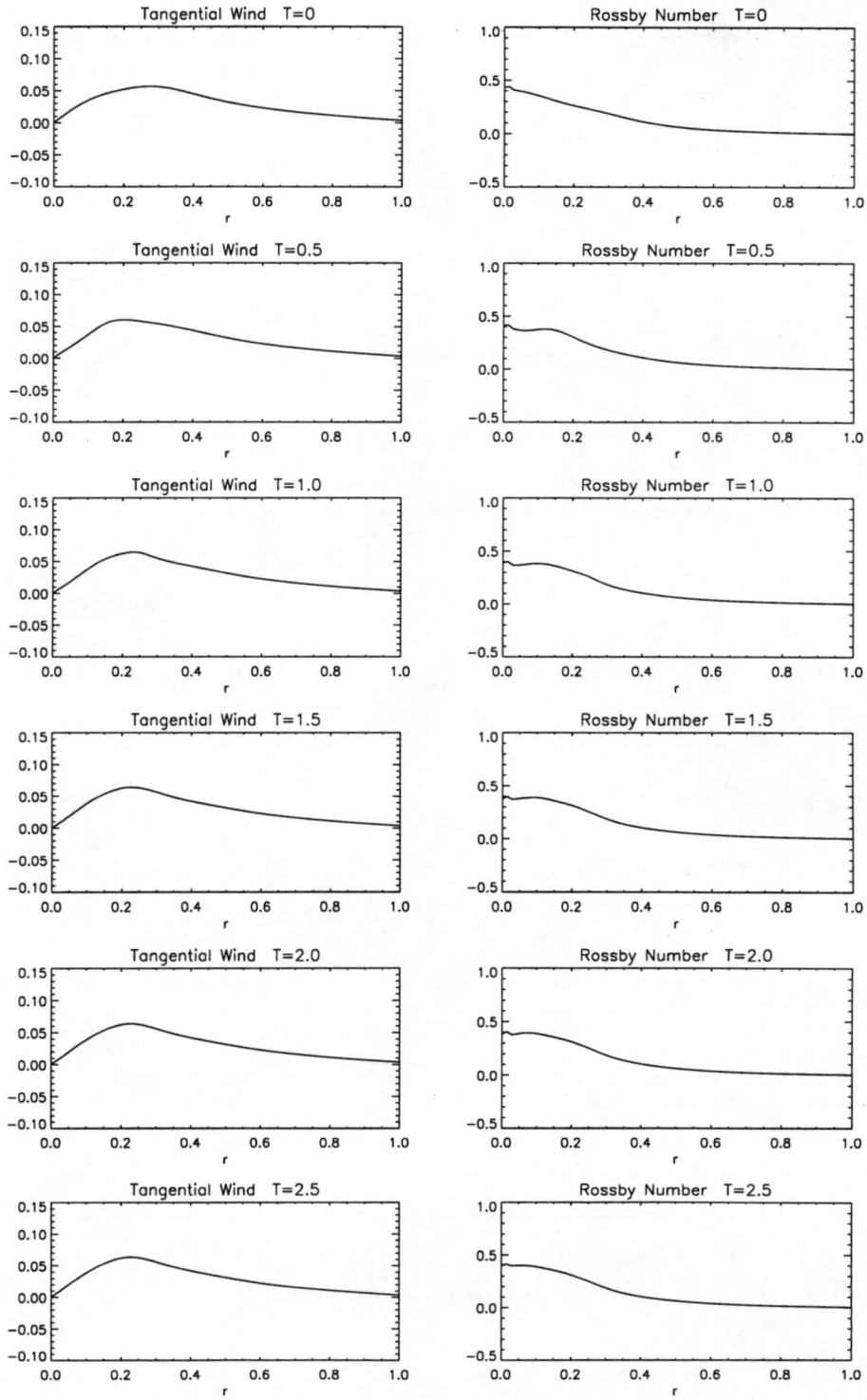

Figure 4.8: Evolution of the azimuthal mean tangential velocity and the Rossby number for the two-cluster convective anomaly at the lowest model level (z=0). To obtain dimensional $\bar{v}$ in ms^{-1}, multiply nondimensional $\bar{v}$ by 100.

outward, in agreement with Figure 4.6. Particles from the positive anomalies at upper levels (resulting from subtracting the azimuthal mean from the total PV field – see Figure 4.6) either move inward to form the slight bump of positive mean PV shown at $r \approx 0.225$ in the radial profiles of Figure 4.6, or move outward to form the secondary maximum at $r \approx 0.45$. These results are in qualitative agreement with our understanding of the vortex's dynamics from the wave, mean flow diagnostics discussed above.

The energy exchange between the mean flow and the eddies can also be quantified. In the absence of heating and friction the sum of the total kinetic energy K plus the available potential energy P integrated over the domain is conserved. The potential enstrophy is also conserved if the vertical boundaries are isothermal, as is the case for all initial conditions used here. We expect to see a slight decrease in energy and potential enstrophy with time due to the explicit diffusion of PV in the numerical model. Each of these quantities decreased by less than 0.5 % in a 1.5 eddy-turnover-time run.

From Appendix A we have for the mean and eddy available potential energies $\bar{P}$ and P':

$$\frac{d\bar{P}}{dt} = -[\bar{P} \cdot \bar{K}] + [P' \cdot \bar{P}] \tag{4.1}$$

and

$$\frac{dP'}{dt} = -[P' \cdot K'] - [P' \cdot \bar{P}]. \tag{4.2}$$

$[\bar{P} \cdot \bar{K}]$ represents the conversion of mean available potential energy to mean kinetic energy. $[P' \cdot \bar{P}]$ represents the conversion of eddy available potential energy to mean available potential energy. $[P' \cdot K']$ represents conversion of eddy available potential energy to eddy kinetic energy. For the mean and eddy kinetic energies $\bar{K}$ and K':

$$\frac{d\bar{K}}{dt} = [\bar{P} \cdot \bar{K}] + [K' \cdot \bar{K}] \tag{4.3}$$

and

$$\frac{dK'}{dt} = [P' \cdot K'] - [K' \cdot \bar{K}] \tag{4.4}$$

$[K' \cdot \bar{K}]$ represents conversion of eddy kinetic energy to mean kinetic energy.

The relationships (4.1) - (4.4) for the two-cluster convective experiment may be summarized in Lorenz box diagrams such as Figure 4.10. All quantities follow the conventions

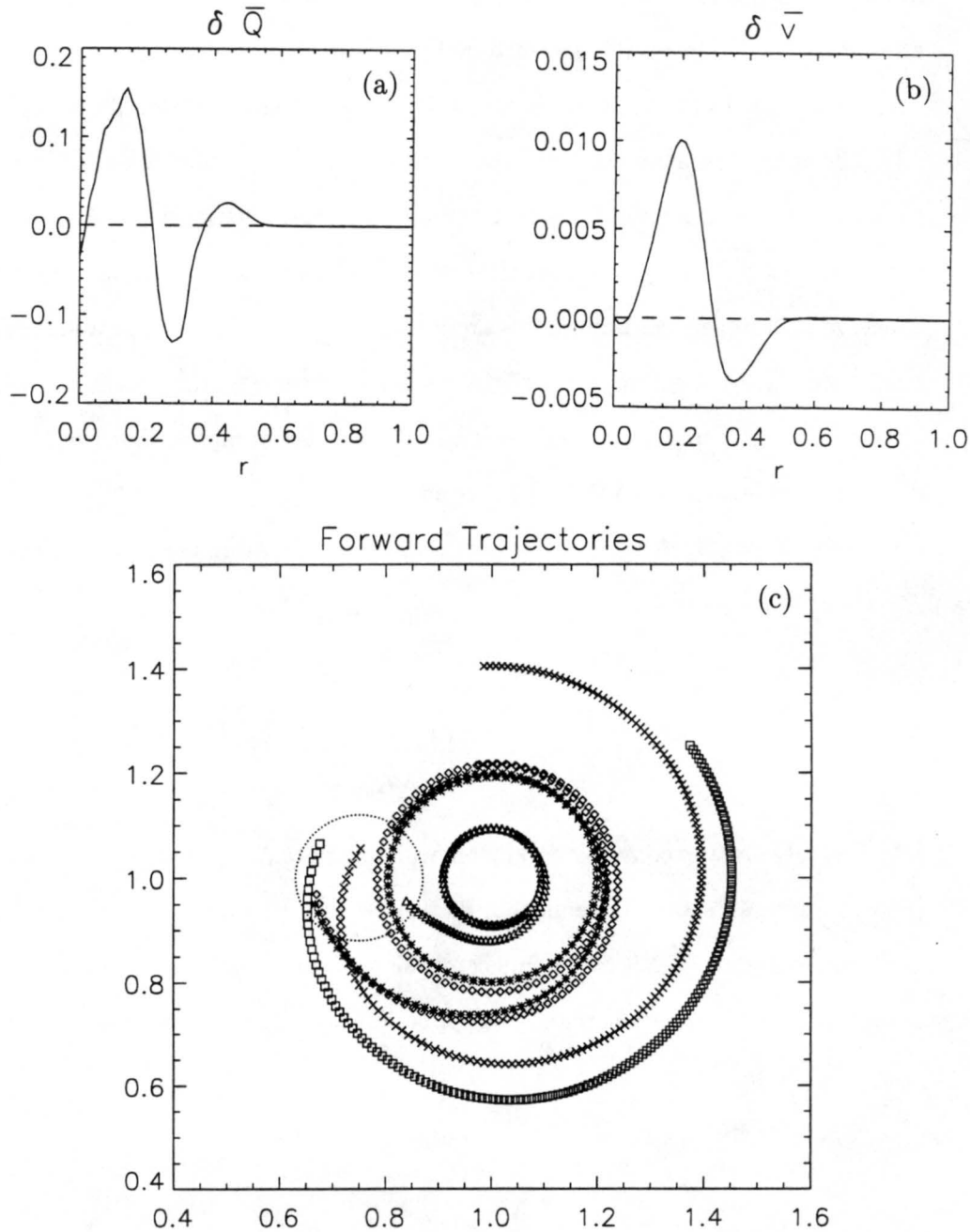

Figure 4.9: (a) Change in azimuthal mean PV ($\delta\overline{Q}$) and (b) change in mean tangential wind ($\delta\bar{v}$) at T=2.5 for the two-cluster convective case at the lowest model level (z=0). $\delta\bar{v}$ in ms^{-1} is obtained by multiplying by 100. (c) Forward trajectories for the two-cluster convective anomaly at the lowest model level (z=0). The dotted line shows the location of the anomaly from which the particles originate. Only the inner 1200 km $\times$ 1200 km of the model domain is shown.

of Holton (1992) suitably defined for cylindrical geometry and are appropriately dimensionalized for comparison with future results. As expected, the largest energy storage is found to be in the mean flow kinetic energy with much smaller amounts stored in the available potential energy of the mean flow, in the eddy kinetic energy and in the eddy available potential energy. The largest energy conversion is that from K' to $\bar{K}$, corresponding to the spinup of the basic state vortex by the eddies observed with the wave, mean flow diagnostics.

4.4 The Single-Cluster Convective Anomaly

For our third example we consider the single-cluster convective anomaly. The single-cluster configuration is intended to simulate a localized outbreak of convection near the pre-existing vortex. For this case the center of the (r,λ) coordinate system is taken to be the geopotential minimum on the lowest level. The behavior is in many ways similar to the two-cluster convective anomaly. Figures 4.11 and 4.12 show the evolution of the mean and eddy PV fields at the top and bottom model levels, respectively, for this anomaly. At the top level, the positive and negative anomalies move apart; at the lowest level the two positive anomalies move together and symmetrize. However, the lowest-level $\delta\bar{Q}$ and $\delta\bar{v}$ distributions, plotted in Figures 4.13(a) and 4.13(b), show a new phenomenon: transport of PV to the center of the vortex. This occurs because the single-cluster convective anomaly has a wavenumber one Fourier component. Only wavenumber one can transport particles to the center of the vortex. This fact can be demonstrated as follows. From the azimuthal mean tangential momentum equation neglecting the Coriolis acceleration we have

$$\frac{\partial \bar{v}}{\partial t} = -\overline{u'\zeta_g'},$$

where ζ_g' is the asymmetric geostrophic vertical vorticity and we recall that u and v denote the radial and tangential geostrophic winds. Integrating over time, assuming the eddy-vorticity flux becomes negligible after some time τ gives

$$\delta\bar{v} = -\int_0^\tau \overline{u'\zeta_g'}dt.$$

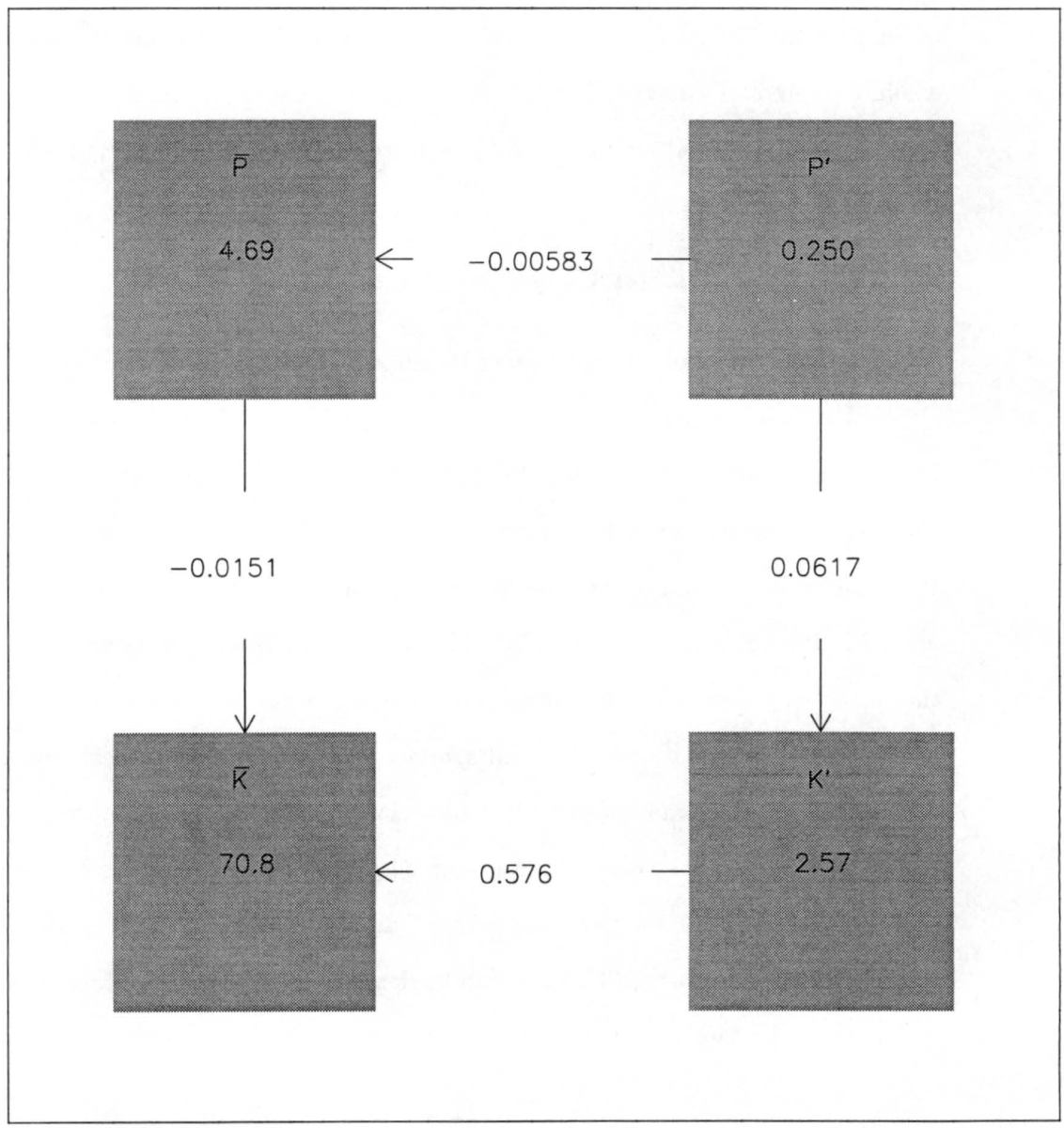

Figure 4.10: Lorenz energy box diagram for the two-cluster convective study at T=0.5. The energies $\bar{P}$, P', $\bar{K}$ and K' are in 10^{15}J and the conversion quantities $[P' \cdot \bar{P}]$, $[P' \cdot K']$, $[K' \cdot \bar{K}]$, and $[\bar{P} \cdot \bar{K}]$ are in 10^{15}J d^{-1}.

By Taylor expanding the perturbation streamfunction ψ' and vorticity about the origin and changing to cylindrical coordinates, it can be shown that the nth Fourier coefficients for both ψ' and ζ_g' vary as r^n as $r \to 0$. The vorticity change for small r is then

$$\delta\bar{\zeta}_g = \frac{1}{r}\frac{\partial(r\delta\bar{v})}{\partial r} \propto r^{2n-2},$$

from which it follows that only $n = 1$ can transport vorticity (and thus PV) to the vortex center. The Lagrangian trajectories show the same effect. Figure 4.13(c) shows the forward trajectory paths for a few selected particles initially distributed randomly over the +PV anomaly, for the single-cluster case. Unlike Figure 4.9(c) in which particles are excluded from the center of the vortex, in Figure 4.13(c) particles pass arbitrarily close to the center.

Figure 4.13(b) shows a low-level spinup of about 0.4 ms^{-1} for single-cluster convection. This is about a factor of 2.5 smaller than for the two-cluster convective anomaly. This reflects the fact that the total initial forcing in the single-cluster case is approximately a factor of two smaller: we use the same magnitude anomaly in both cases, but there are two positive anomalies for the two-cluster case and only one for the one-cluster example. For a comparison of the spinup due to single-cluster versus double-cluster anomalies as a function of the anomaly amplitude, see section 4.7.

Table 4.1 shows the dependence of the final maximum low-level azimuthal mean tangential wind speed about the geopotential minimum on the radial location of the convective patch for the single-cluster convective configuration. Convection at or near the center of the basic state vortex produces significantly greater values of $\bar{v}_{max}$. For radii much greater than the initial radius of maximum winds of the basic state vortex, a slight spindown ($\delta\bar{v}_{max} < 0$) is observed. This is because, for anomalies at radii much greater than the initial RMW of the basic state vortex, the surface RMW moves outward, resulting in some spindown at inner radii ($\leq$ 200 km) and a slight increase in surface mean tangential winds at larger radii (300 - 500 km). An overall slight reduction in the maximum mean tangential surface wind, compared to the nominal case, is observed. The final radius of maximum winds also depends on the initial radial location of the convection, ranging from

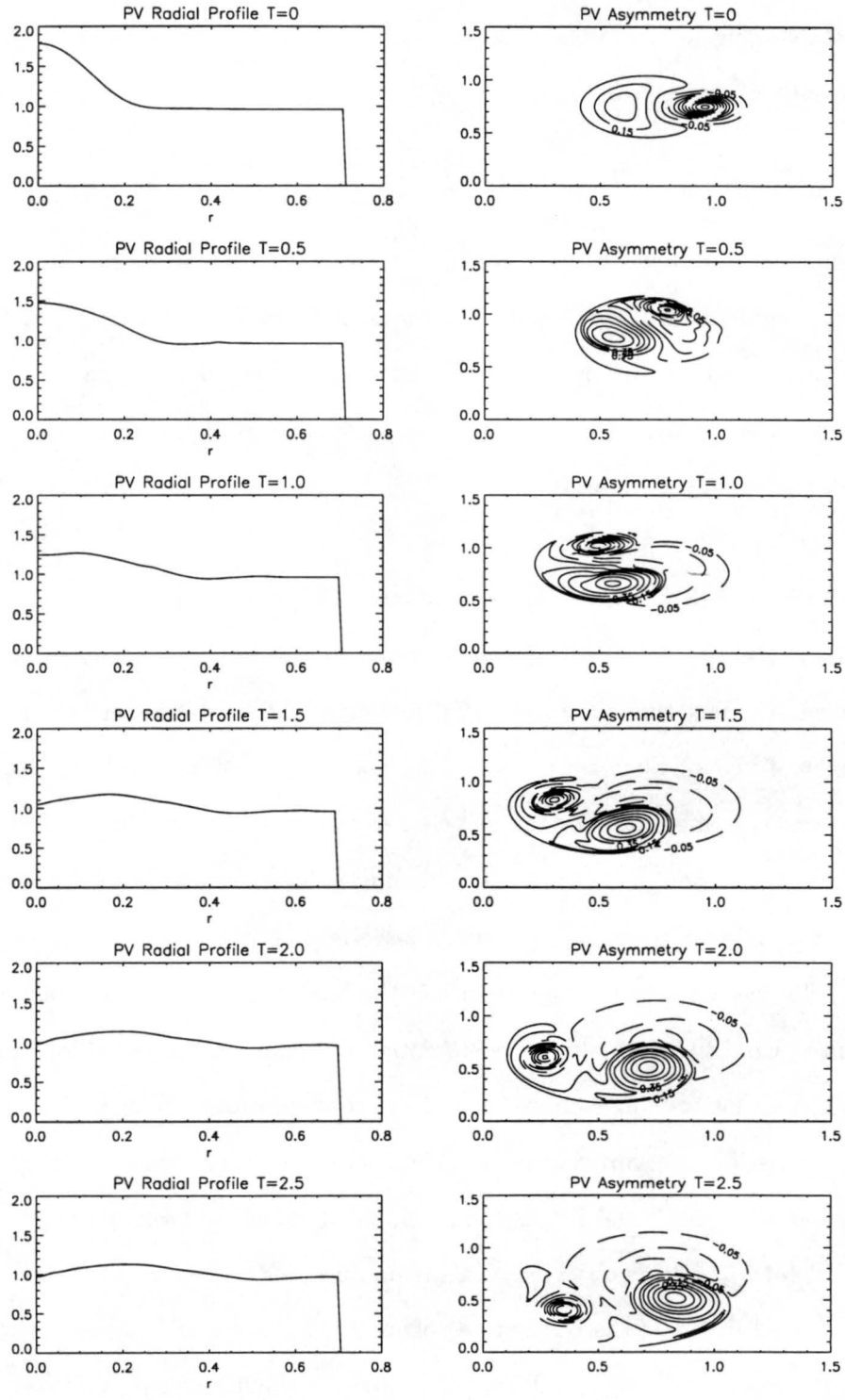

Figure 4.11: Evolution of the azimuthal mean PV and asymmetric PV for the single-cluster convective case at the highest model level (z=1). Radial profiles extend only to approximately 700 km because of the motion of the lowest-level center of the system.

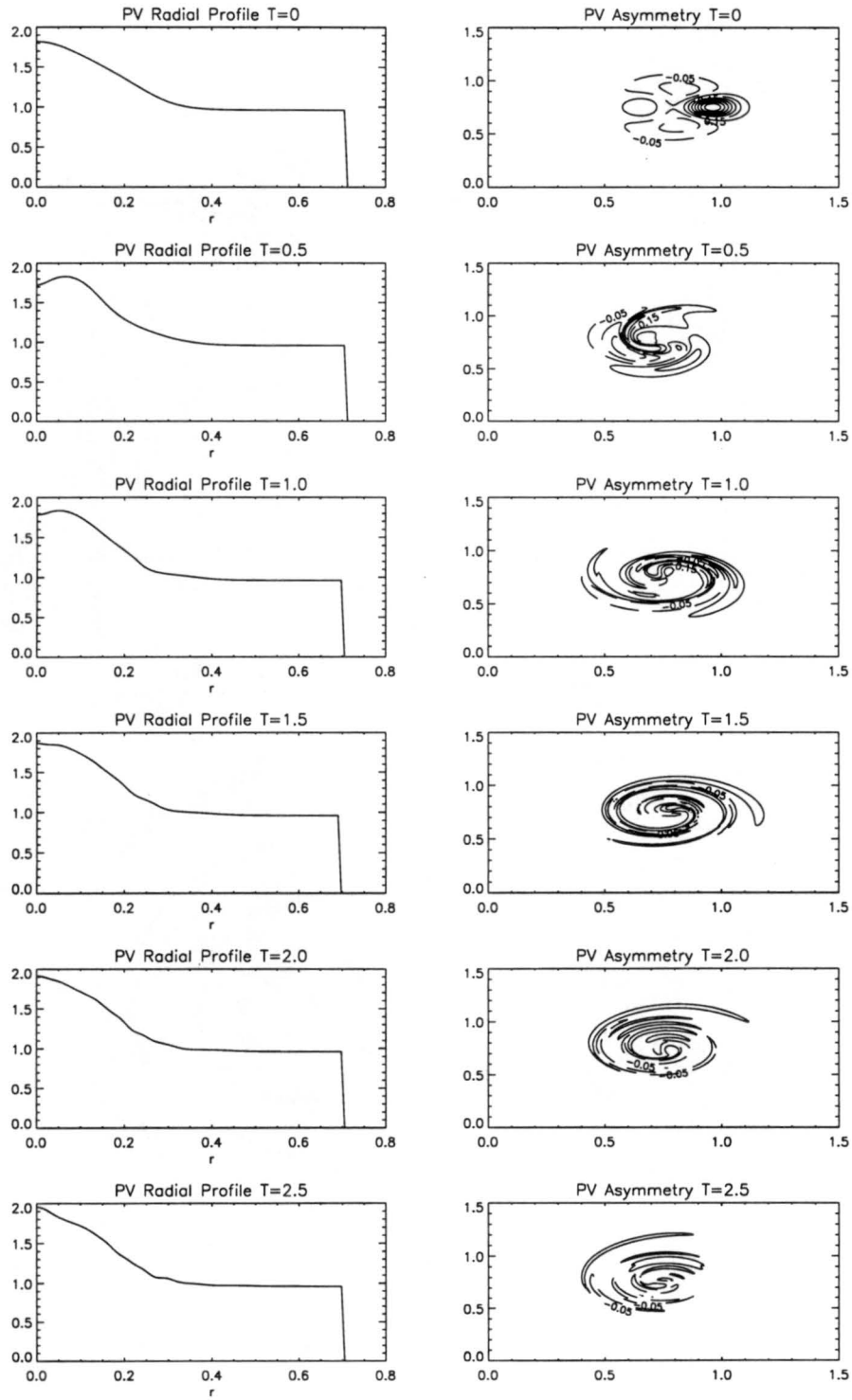

Figure 4.12: Evolution of the azimuthal mean PV and asymmetric PV for the single-cluster convective anomaly at the lowest model level (z=0). Radial profiles extend only to approximately 700 km because of the motion of the lowest-level center of the system.

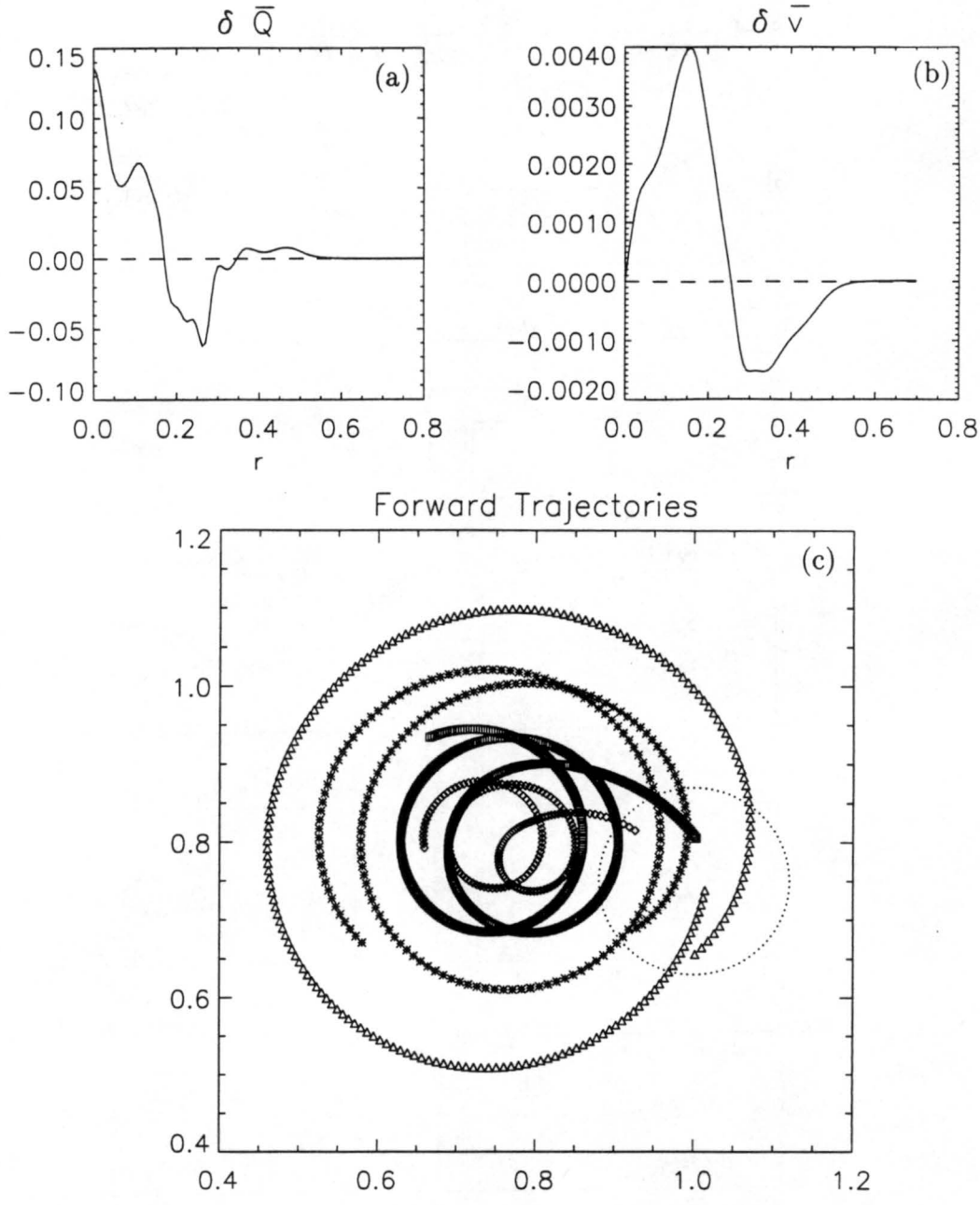

Figure 4.13: (a) Change in azimuthal mean PV ($\delta\bar{Q}$) and (b) change in azimuthal mean tangential wind ($\delta\bar{v}$) at T=2.5 for the single-cluster convective case at the lowest model level (z=0). $\delta\bar{v}$ in ms^{-1} is obtained by multiplying by 100. (c) Forward trajectories for the single-cluster convective case at the lowest model level (z=0). The dotted line shows the location of the anomaly from which the particles originate. Only the inner 800 km × 800 km of the model domain is shown.

Radius of Convective Anomaly (km)	$\bar{v}_{max}$ (ms^{-1})
0	7.0
100	6.4
250	5.6
400	4.9
500	4.7

Table 4.1: Final maximum azimuthal mean tangential wind as a function of the radial location of the convective patch from the initial vortex center.

approximately 150 km for convection at the center to 235 km for convection at 500 km radius.

The largest increase in tangential velocity occurs when the convective patch is placed at the center of the initial basic state vortex. In view of this fact, the reader may wonder why our emphasis is on the role of asymmetries in the spinup process. However, it should be noted that, assuming that at the genesis stage the pre-existing vortex does not play a strong role in organizing the convection, it is more probable that convective outbreaks will occur somewhere near the periphery of the vortex rather than very close to the center; thus we believe that asymmetric processes are likely to be an important contribution to mechanisms for tropical cyclogenesis. As discussed in Chapter 6, observations appear to indicate that asymmetries play an important role in the genesis process. When symmetric convection does occur, it can be expected to yield stronger and more rapid spinup.

4.5 A Midlevel Vortex With Convection

The time evolution of the midlevel vortex configuration is shown in Figures 4.14 - 4.17. The figures show contours of PV on z=0, z=0.25, z=0.5, z=0.75 and z=1, as well as a plan view of contours of PV versus x and y on z=0. The midlevel vortex is initially centered at x=0.75, y=0.75. The low-level PV anomaly, initially 0.25 (250 km) from the center of the basic state vortex, is drawn approximately 0.2 (200 km) into the center to a position underneath the main vortex and subsequently remains aligned with it, producing a vertically stacked vortex in the mid- to low-level troposphere. In contrast, the negative PV anomaly at upper levels is expelled laterally from the axis of the now-aligned vortex

system. This example demonstrates that our axisymmetrization mechanism could cause an MCV to appear to "build downward" in the presence of peripheral convection, resulting in spinup of strong winds at the surface.

The midlevel vortex experiment shows some spinup of the azimuthal mean tangential wind about the center of the midlevel vortex. At T=0 the mean tangential wind maximum at the surface occurs at about 300 km from the axis of the mean vortex, approximately corresponding to the position of the convective anomaly. The mean surface tangential wind maximum measured about the axis of the midlevel vortex is 2.3 ms^{-1}. At T=2.5, the surface RMW has contracted to 150 km and the mean surface tangential wind maximum has increased to 3.0 ms^{-1}, with a maximum spinup of 1.7 ms^{-1}. The surface vortex is now capable of further growth if convection continues to occur around it.

4.6 Warm Core Formation Through Axisymmetrization

In the course of the two-cluster relaxation experiment, a slight warming of 0.08 K in the azimuthal mean temperature field is observed at middle to low levels. As we will see in Chapter 5, in the presence of ongoing convection a strong warm core of magnitude 3-5 K forms during the axisymmetrization process. We now discuss the physical basis for the warming observed in the relaxation experiments.

On azimuthally averaging the thermodynamic equation we obtain

$$\frac{\partial \overline{\phi}_z}{\partial t} = -\frac{\partial}{r\partial r}\left[r\overline{u'\phi'_z}\right] - N^2\overline{w} + \frac{g}{\theta_0}\overline{\dot{\theta}}. \tag{4.5}$$

Contributions to $\partial\overline{\phi}_z/\partial t$ come from radial eddy-heat flux, mean vertical motion, and heating due to convection. In the relaxation experiments after the initial pulse $\overline{\dot{\theta}} = 0$.

The mean vertical motion is given by the radial derivative of the transverse streamfunction:

$$\bar{w} = \frac{\partial}{r\partial r}\overline{\psi},$$

where $\overline{\psi}$ is deduced upon solving the Sawyer-Eliassen equation derived in Appendix A:

$$N^2\frac{\partial}{\partial r}\left(\frac{\partial}{r\partial r}\overline{\psi}\right) + \frac{f^2}{r}\frac{\partial^2\overline{\psi}}{\partial z^2} = \frac{\partial E}{\partial r} - \frac{\partial F}{\partial z} \tag{4.6}$$

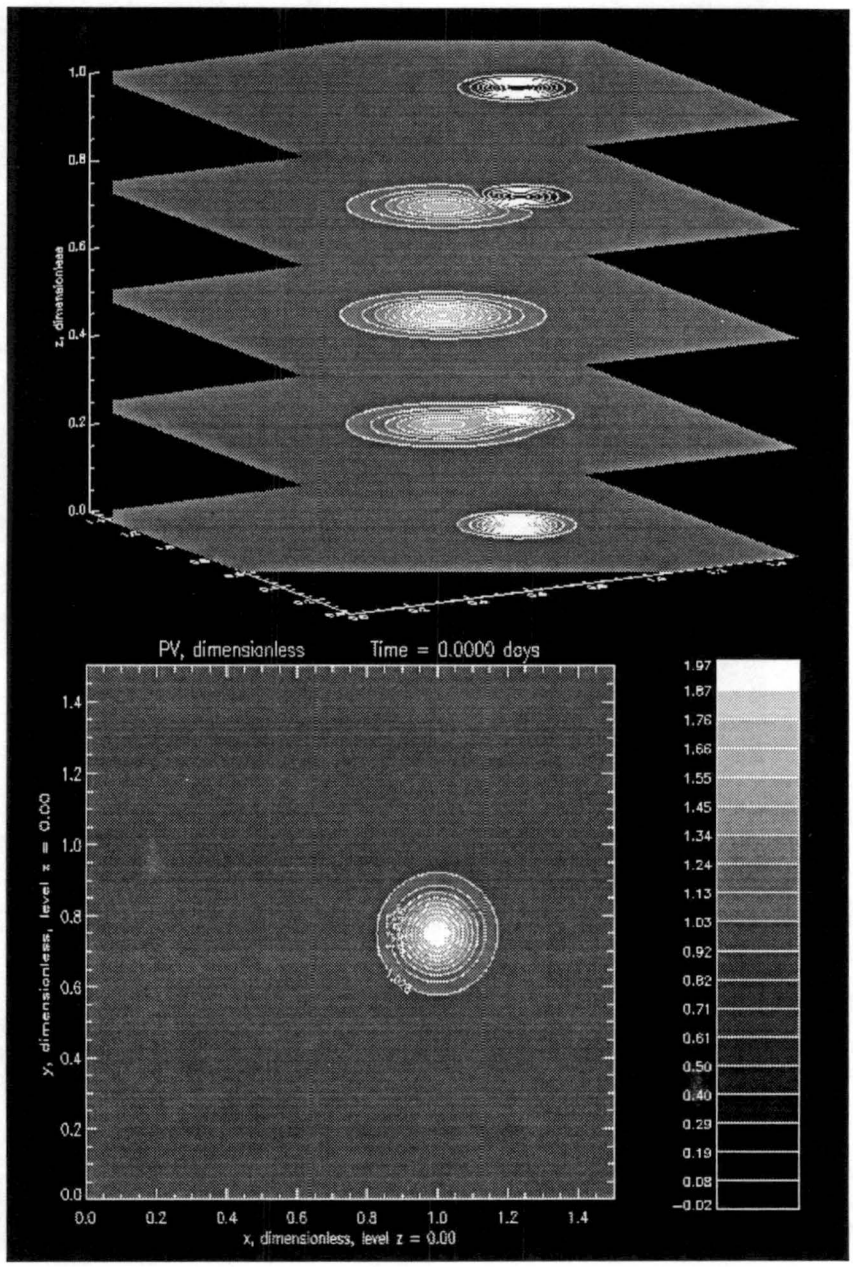

Figure 4.14: Contours of PV versus x and y on z=0, z=0.25, z=0.5, z=0.75 and z=1, as well as a plan view of contours of PV versus x and y on z=0, for the midlevel vortex with single-cluster convection at time T=0.

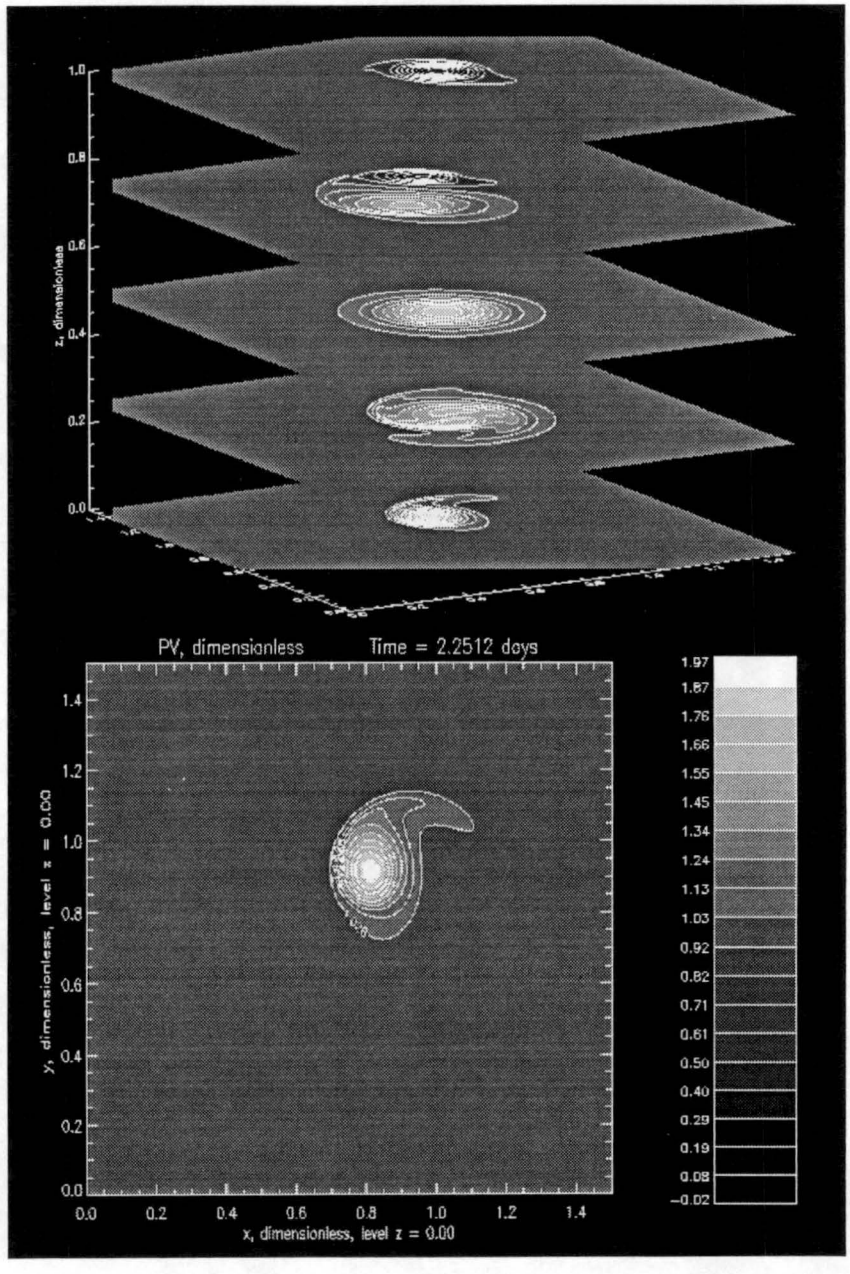

Figure 4.15: Contours of PV versus x and y on z=0, z=0.25, z=0.5, z=0.75 and z=1, as well as a plan view of contours of PV versus x and y on z=0, for the midlevel vortex with single-cluster convection at time T=2.25 days.

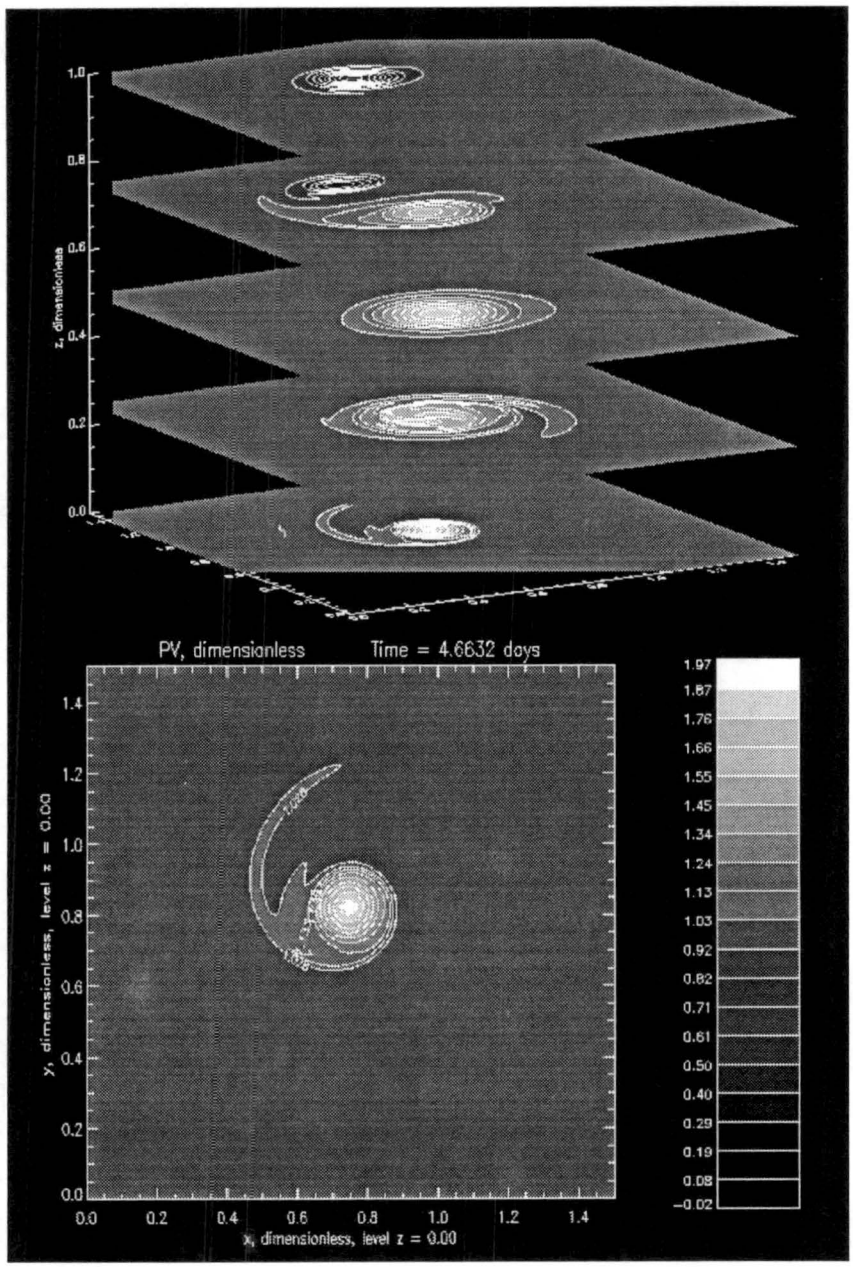

Figure 4.16: Contours of PV versus x and y on z=0, z=0.25, z=0.5, z=0.75 and z=1, as well as a plan view of contours of PV versus x and y on z=0, for the midlevel vortex with single-cluster convectionat time T=4.66 days.

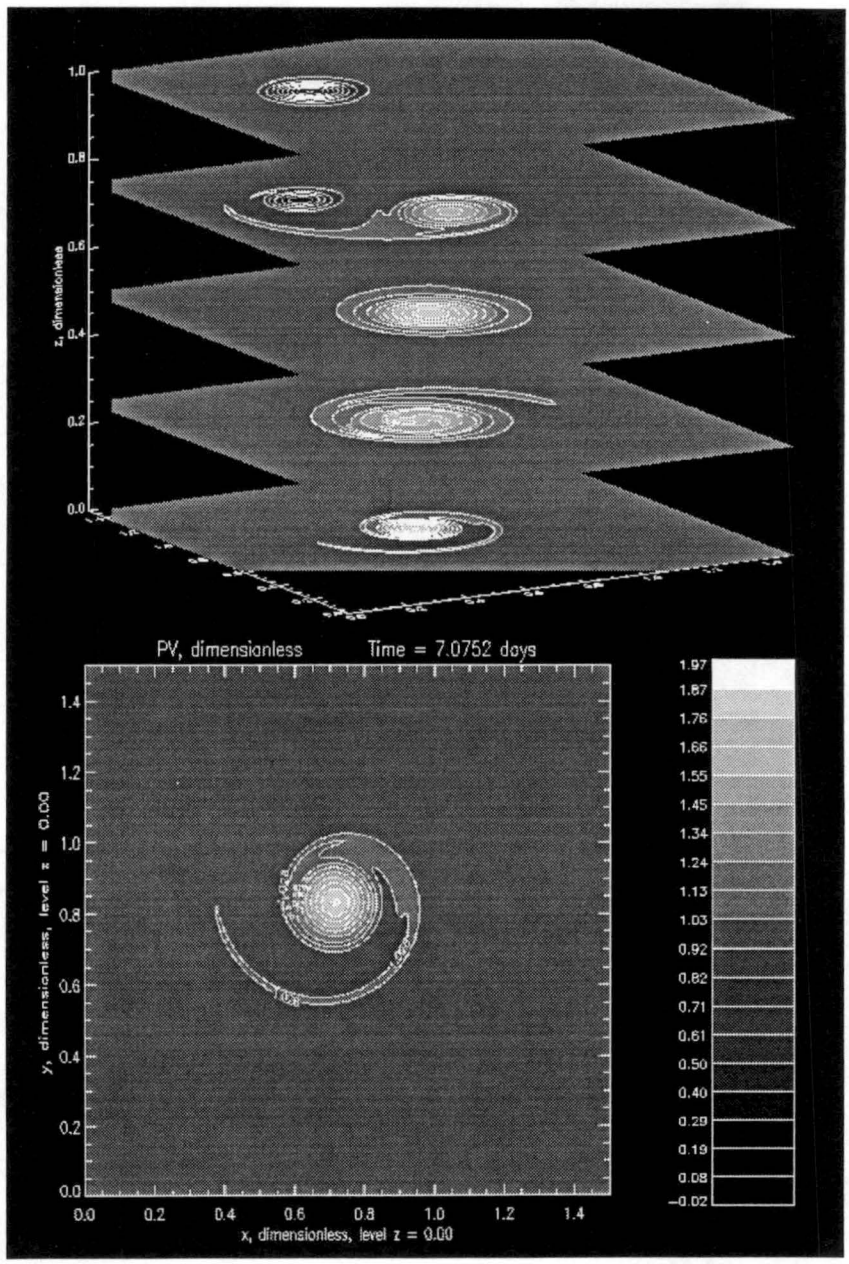

Figure 4.17: Contours of PV versus x and y on z=0, z=0.25, z=0.5, z=0.75 and z=1, as well as a plan view of contours of PV versus x and y on z=0, for the midlevel vortex with single-cluster convection at time T=7.07 days.

with

$$E = -\frac{\partial}{r\partial r}(\overline{ru'\phi'_z})$$

and

$$F = -\frac{f}{r^2}\frac{\partial}{\partial r}\left[r(\overline{rv'u'})\right].$$

Note that equation (4.6) is dimensional. E represents the contribution from eddy-heat flux forcing, and F represents the contribution from eddy-momentum flux forcing.

Neglecting for the moment the contribution from the eddy-heat fluxes, the physics responsible for the mean vertical motion can be illustrated with a simple example. Figure 4.18 shows schematically the change in the mean tangential wind $\delta\bar{v}$ induced by eddy-momentum flux forcing following the imposition of a convective PV anomaly at low levels near the undisturbed circular vortex. As we have already seen in section 4.3, a local torque is exerted on the circular vortex during the axisymmetrization process which causes a net spinup of the tangential winds. Because the secondary circulation always acts to oppose changes induced by the geostrophic flow, the mean transverse circulation consists of a radially outward flow near the $\delta\bar{v}$ maximum which increases the vortex's moment of inertia and tends to resist the spinup. Similarly, near the $\delta\bar{v}$ minimum the mean transverse circulation is radially inward. The resultant mean convergence leads to mean ascent in between the two regions, as sketched in the figure; by mass conservation, mean subsidence develops near the center of the vortex as shown. When the contribution from eddy-heat fluxes is included the dynamics are no longer so simple.

As a first look at the relative importance of heat and momentum flux contributions to the development of the warm core, azimuthal mean Eliassen-Palm (EP) flux vectors (Edmon et al. 1980) for the two-cluster relaxation experiment have been analyzed. In cylindrical coordinates the quasigeostrophic EP flux vector, derived in Appendix A, is given by

$$\mathbf{F} = \left(-\overline{rv'u'}, -\frac{f}{N^2}\overline{ru'\frac{\partial\phi'}{\partial z}} \right).$$

Figure 4.19 shows the EP flux vectors along with contours of the radial PV flux ($\overline{u'Q'} = -\frac{1}{r}\nabla\cdot\mathbf{F}$) for the two-cluster relaxation experiment at time T=0.5 τ_{eddy}. The directions of

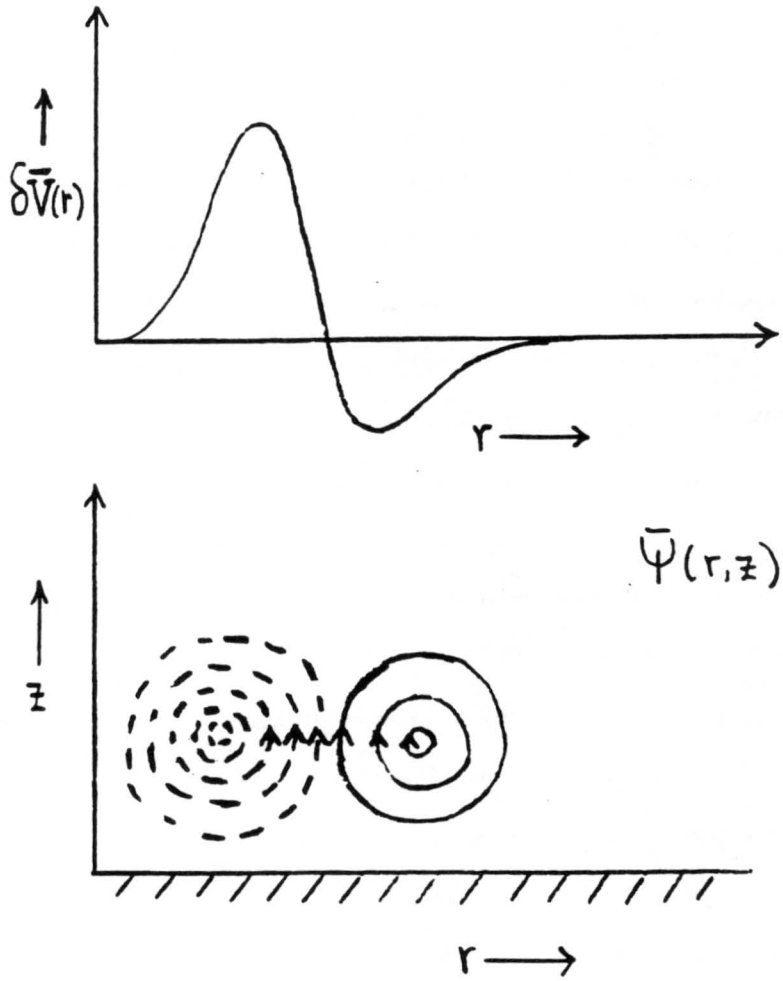

Figure 4.18: Top: change in the mean tangential wind ($\delta\bar{v}$) induced by eddy momentum flux forcing following the imposition of a convective PV anomaly at low levels near the undisturbed circular vortex. Bottom: schematic Green's function response to the Sawyer-Eliassen equation in the vicinity of a delta function source corresponding to an inward eddy momentum flux near the lower boundary of the domain. Solid and dotted lines show streamlines. Arrows show direction of the flow. In the inner core of the vortex subsidence is induced, leading to warming in that region.

the EP flux vectors indicate whether heat or momentum is being fluxed in or out of the vortex: upward arrows indicate inward heat flux and rightward arrows indicate inward cyclonic momentum flux. At low levels, for $r < 0.3$, $\overline{u'Q'}$ is negative, indicating that the PV flux is upgradient (into the vortex); for $r > 0.3$, $\overline{u'Q'}$ is positive, showing the downgradient flux of PV into the high-PV filaments at larger radii. The greater values of $\nabla \cdot \mathbf{F}$ at lower levels agree with our other diagnostics indicating that the energy transferred to the mean flow is greater at lower levels.

The degree of horizontality of the EP flux vectors gives some indication of the relative importance of eddy-momentum flux versus eddy-heat flux. However, as indicated in equation (4.6), the mean transverse streamfunction is derived from derivatives of the fluxes rather than from the fluxes themselves. For a direct comparison of the effects of momentum flux to heat flux we turn to explicit computation of the forcing terms in the Sawyer-Eliassen equation.

Analytical calculations have been carried out in order to study the relative importance of the heat flux and momentum flux contributions. Writing the perturbation geopotential relative to the barotropic mean vortex $\overline{\phi}(r)$ as

$$\phi'(r, \lambda, z, t) = \sum_{m=0}^{\infty} \sum_{n=-\infty}^{\infty}{}' e^{in\lambda} \hat{\phi}_{mn}(r, t) \cos m\pi z,$$

where $\hat{\phi}_{mn}$ is the Fourier coefficient for the m'th vertical and n'th azimuthal mode and the prime on the sum denotes omission of the $n = 0$ component, it can be shown that if only one vertical mode and one azimuthal mode are present the resultant heat flux is identically zero. To give a nonzero heat flux more than one vertical or azimuthal mode must be involved.

The relative importance of the heat flux and momentum flux contributions have been studied using the quasigeostrophic model. A simulation initialized with the two-cluster convective anomaly was studied with resultant fields output every 0.125 τ_{eddy} in order to study the rapid azimuthal shearing of the asymmetry. At each output time the two forcing terms, $\partial E/\partial r$ and $-\partial F/\partial z$, were calculated and plotted. The results for some selected times are shown in Figure 4.20. We see from Figure 4.20 that at early times

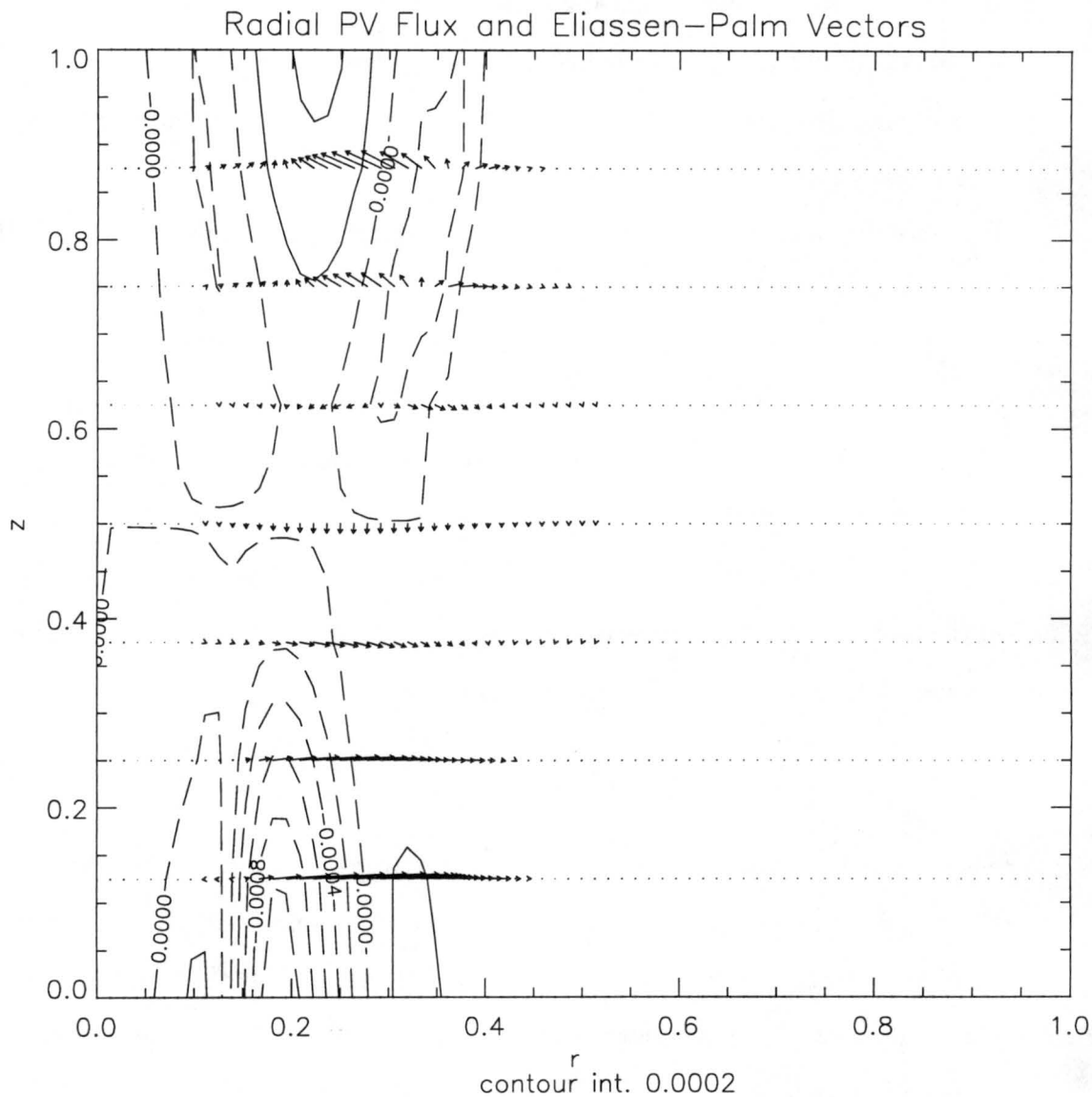

Figure 4.19: Eliassen-Palm flux vectors and mean radial potential vorticity flux ($\overline{u'Q'} = -\frac{1}{r}\nabla \cdot \mathbf{F}$) for the pulsed two-cluster convective anomaly at T = 0.5. To convert $\mathbf{F}$ to dimensional units, multiply the horizontal component by 10^{10} m^3s^{-2} and the vertical component by 10^8 m^3s^{-2}.

the momentum flux term $-\partial F/\partial z$ dominates the heat flux term $\partial E/\partial r$ everywhere. The effect of the momentum flux is best seen by looking at $-\partial F/\partial z$ at T=0.375 in Figure 4.20. The momentum flux forcing at low levels inside the radius of maximum winds is strongly positive. The elliptic operator in equation (4.6) tends to reverse the sign of the operand, so that in the region where $-\partial F/\partial z$ is strongly positive, $\bar{\psi}$ is strongly negative. It follows that $\bar{w}$ is negative near the center of the vortex at low levels; thus there is subsidence in that region as expected.

All throughout this process the heat flux term is non-zero; by T = 0.375 the heat flux becomes a significant contribution to the forcing at upper levels. Nevertheless the maximum warming occurs in the middle to lower levels where the momentum flux is dominant.

4.7 Nonlinear Feedback in the Axisymmetrization Process

As we will see in the following chapter, it is of interest to study the dependence of the maximum spinup $\delta\bar{v}_{max}$ on the asymmetry amplitude. In the quasilinear nondivergent regime $\delta\bar{v}$ scales as $\eta^2 v_{max}$, where v_{max} is the maximum wind of the basic state vortex, and η is the strength of the asymmetry relative to the basic state vortex (MK). Using $\eta = Q'/Q_{max}$ where Q' is the maximum magnitude of the PV anomaly and Q_{max} is the maximum PV of the basic state, and recalling that the invertibility relation is linear, we find that $\delta\bar{v} \sim Q'^2/v_{max}$. In our experiments Q'/Q_{max} is not small, but this scaling may nevertheless be approximately valid. Experiments were performed to test the dependence of $\delta\bar{v}_{max}$ and the maximum temperature change $\delta\bar{T}_{max}$ on Q' and v_{max}.

Figure 4.21 shows the results of these tests, along with the predicted maximum $\delta\bar{v}$ and maximum $\delta\bar{T}$ assuming linear and quadratic scaling in Q'. Note that, since the upper levels do not axisymmetrize, one obtains small fluctuations in the azimuthal mean quantities for the single-cluster experiments as the low-level center of the system moves. For the two-cluster case at the tested amplitudes the scaling of $\delta\bar{v}_{max}$ is intermediate between linear and quadratic. However, the temperature change $\delta\bar{T}_{max}$ has a greater than quadratic dependence on Q'. For the single-cluster case, the dependence of $\delta\bar{v}_{max}$ is greater than

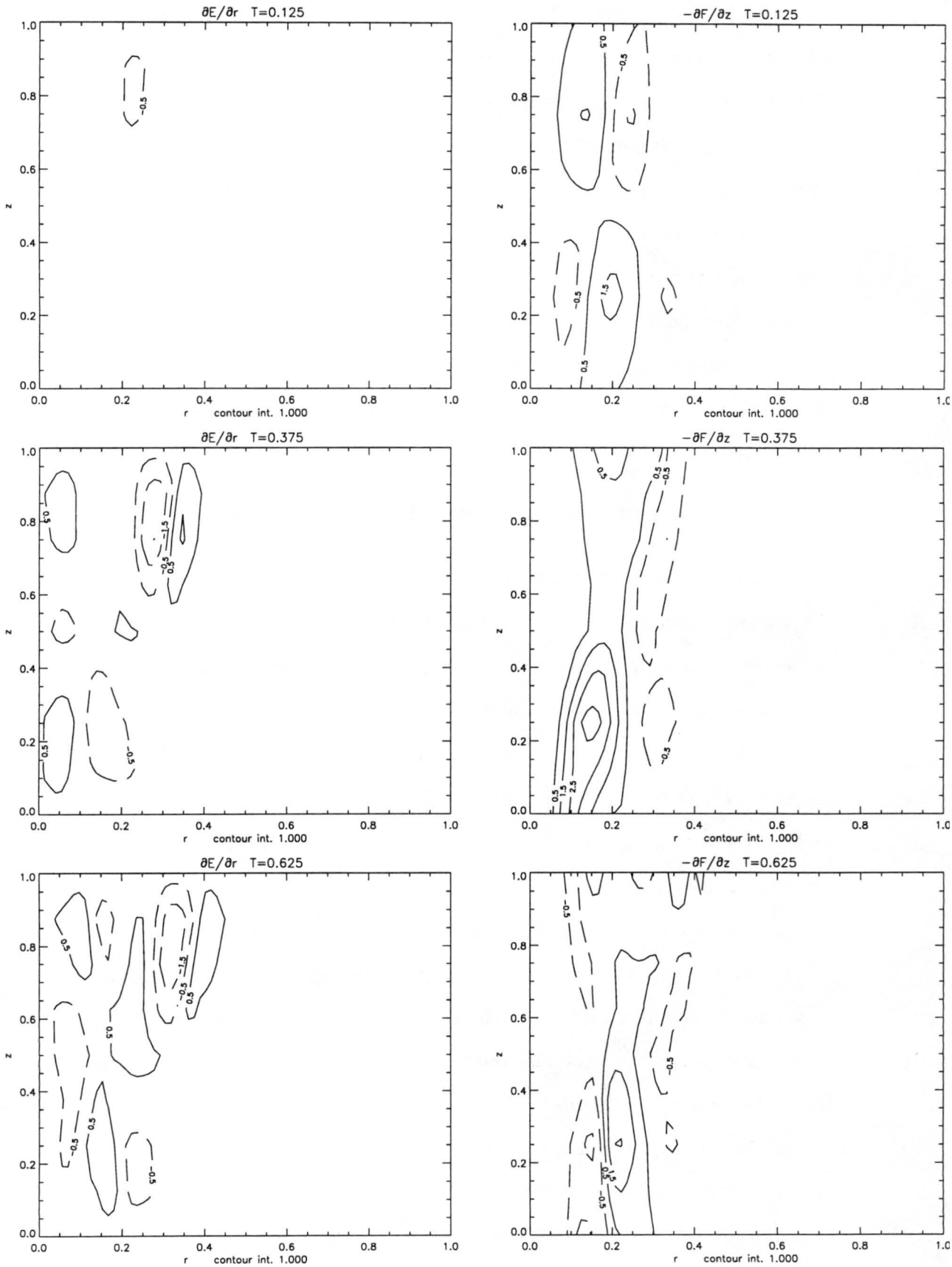

Figure 4.20: Momentum flux and heat flux terms on the right-hand side of the Sawyer-Eliassen equation as a function of time for the two-cluster convective relaxation experiment. To obtain the forcing terms in s^{-3}, multiply by 10^{-13}.

quadratic, but the variation of the temperature change with amplitude is quite small. For the single-cluster experiments, the largest spinup occurs inside the RMW, at $r \approx 150$ km, due to the ability of the wavenumber one component to transport like-sign PV all the way to the center of the vortex.

The dependence of $\delta\bar{v}_{max}$ and $\delta\bar{T}_{max}$ on v_{max} was also tested. For the double cluster experiment $\delta\bar{v}_{max}$ is approximately inversely proportional to v_{max}, for an increase of 20 % in v_{max}. For the single-cluster case, an increase of 20 % in v_{max} results in a 24 % decrease in $\delta\bar{v}_{max}$. For both cases $\delta\bar{T}_{max}$ is essentially unaffected by a change in vortex strength. We have not yet developed a simple scaling argument which predicts the dependence of $\delta\bar{T}_{max}$ on anomaly amplitude and vortex strength.

These results are indicative of nonlinear feedback in the dynamics. From the dimensional vertical vorticity equation for QG dynamics

$$\frac{\partial\bar{\zeta}_g}{\partial t} = -\frac{1}{r}\frac{\partial}{\partial r}(\overline{ru'\zeta'_g}) - \frac{f}{r}\frac{\partial}{\partial r}(r\bar{u}_a), \tag{4.7}$$

some type of nonlinear spinup effect is expected.

On the face of it one might claim that the spinup in these experiments occurs simply because the azimuthal mean radial secondary circulation is converging the convectively generated relative vorticity into the storm's inner core. This idea is incorrect for two reasons. First, as seen from equation (4.7), in QG theory the azimuthal mean secondary circulation (which is solely ageostrophic) converges only planetary, not relative vorticity. Second, most of the spinup occurs in the inner core of the storm where the azimuthal mean radial circulation at low levels is outward (hence divergent). From the PV viewpoint, since potential vorticity is advected solely by the geostrophic wind, its advection into the core occurs purely through eddy transports.

4.8 Amplitude Sensitivity and Wave-Induced Discrete Vortex Modes

In all the experiments described thus far, the upper-level PV anomalies do not axisymmetrize. In addition to the fact that the upper-level anomalies exist in favorable shear, we believe that the disruption of axisymmetrization at upper levels can be traced to the

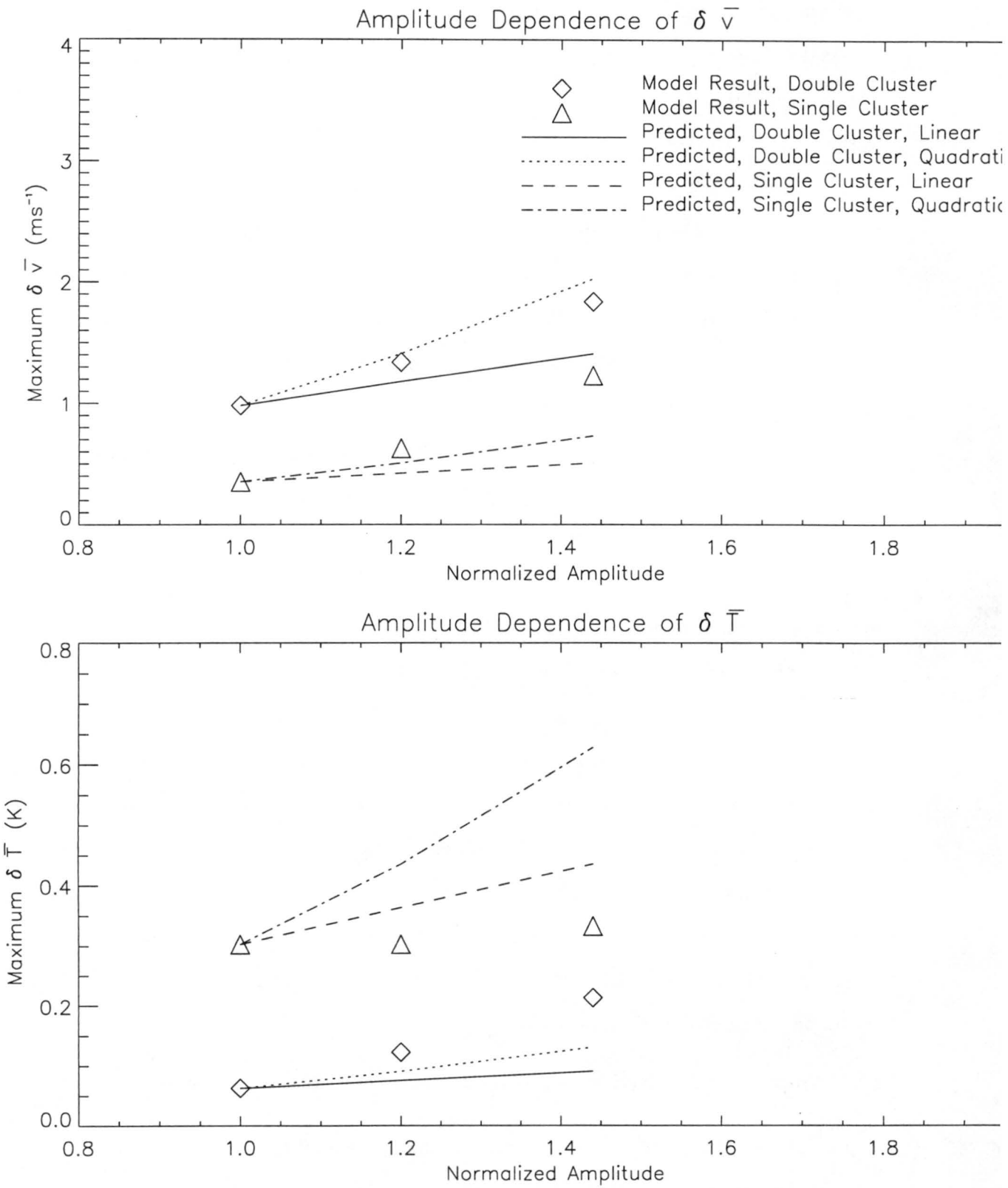

Figure 4.21: Maximum $\delta\bar{v}$ and maximum change in temperature as a function of anomaly amplitude for the double cluster and single cluster relaxation experiments. Model results are compared with predictions assuming linear and quadratic scaling. The amplitude is displayed in units of the nominal anomaly pulse amplitude. $\delta\bar{v}$ is in ms^{-1} and $\delta\bar{T}$ in K.

existence of discrete neutral or unstable vortex Rossby modes propagating azimuthally around the vortex center. For linear waves neutral nonsingular modes require a vanishing radial PV gradient somewhere in the flow (Pedlosky 1987; section 7.8), while unstable modes require $\partial\bar{q}/\partial r$ to change sign at least once (Gent and McWilliams 1986). To investigate these ideas, we studied smaller-amplitude disturbances which permitted us to enter a quasi-linear regime.

When the amplitude of the anomalies was decreased by a factor of five from the nominal case, we still obtained a weak wave-induced sign change of the azimuthal radial PV gradient at upper levels near $r = 350$ km. The time evolution of the upper-level azimuthal mean PV and the asymmetric PV for this experiment are shown in Figure 4.22. Under these conditions one can discern a persistent upper-level wavenumber two disturbance after the axisymmetrization at low levels is complete. Despite the presence of differential rotation at all levels, the disturbance retained its shape as it propagated cyclonically around the vortex.

In order to verify the fact that this mode's existence depended on the sign change of the azimuthal mean radial PV gradient, we moved the anomalies inward to a position 150 km from the center of the vortex. This change had the effect of superposing the anomalies on a larger value of the basic state PV so that the basic state $\partial\bar{q}/\partial r$ dominated the wave-induced radial PV gradient. The time evolution of the upper-level azimuthal mean PV and the asymmetric PV for this experiment are shown in Figure 4.23. In this configuration we observe axisymmetrization at all levels, verifying the disappearance of the discrete or weakly unstable baroclinic modes.

The existence of wave-induced discrete neutral or weakly unstable baroclinic vortex modes raises intriguing possibilities about their ability to orchestrate further convective bursts near the RMW and sustain intensification. A thorough investigation of these ideas requires a self-consistent cumulus convection model which is beyond the scope of this paper. This topic, as well as further investigation of the underlying dynamics of the discrete vortex Rossby modes, remains for future work.

We also examined the effect on the low-level axisymmetrization of significantly increasing the anomaly amplitude. Figure 4.24 shows the evolution of the azimuthal mean

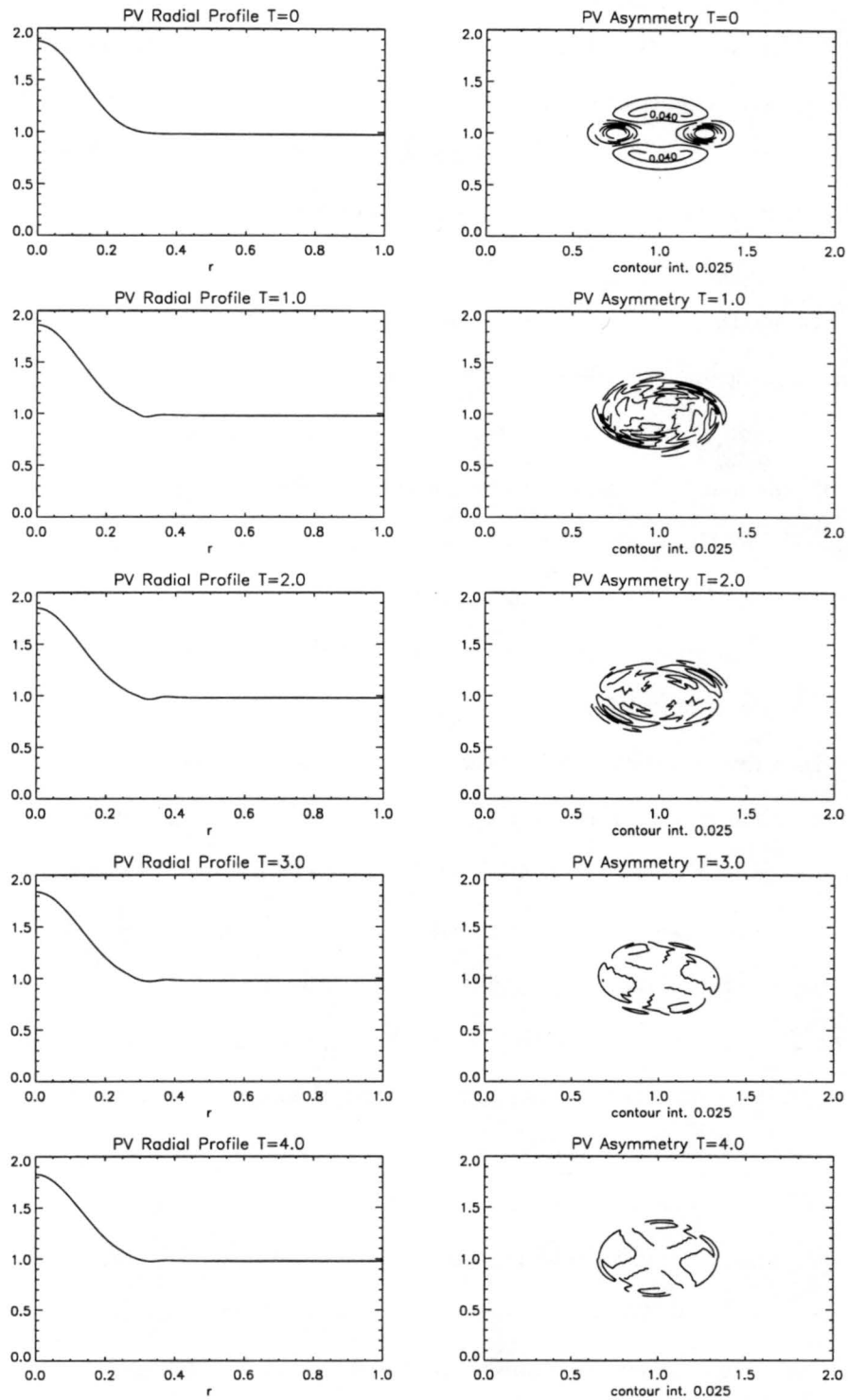

Figure 4.22: Time evolution of the azimuthal mean PV and asymmetric PV at the highest model level (z=1) for a two-cluster convective experiment with anomaly amplitudes a factor of 5 smaller than nominal (at T = 0, 1, 2, 3, 4). Anomalies are 0.25 (250 km) from the basic state vortex center.

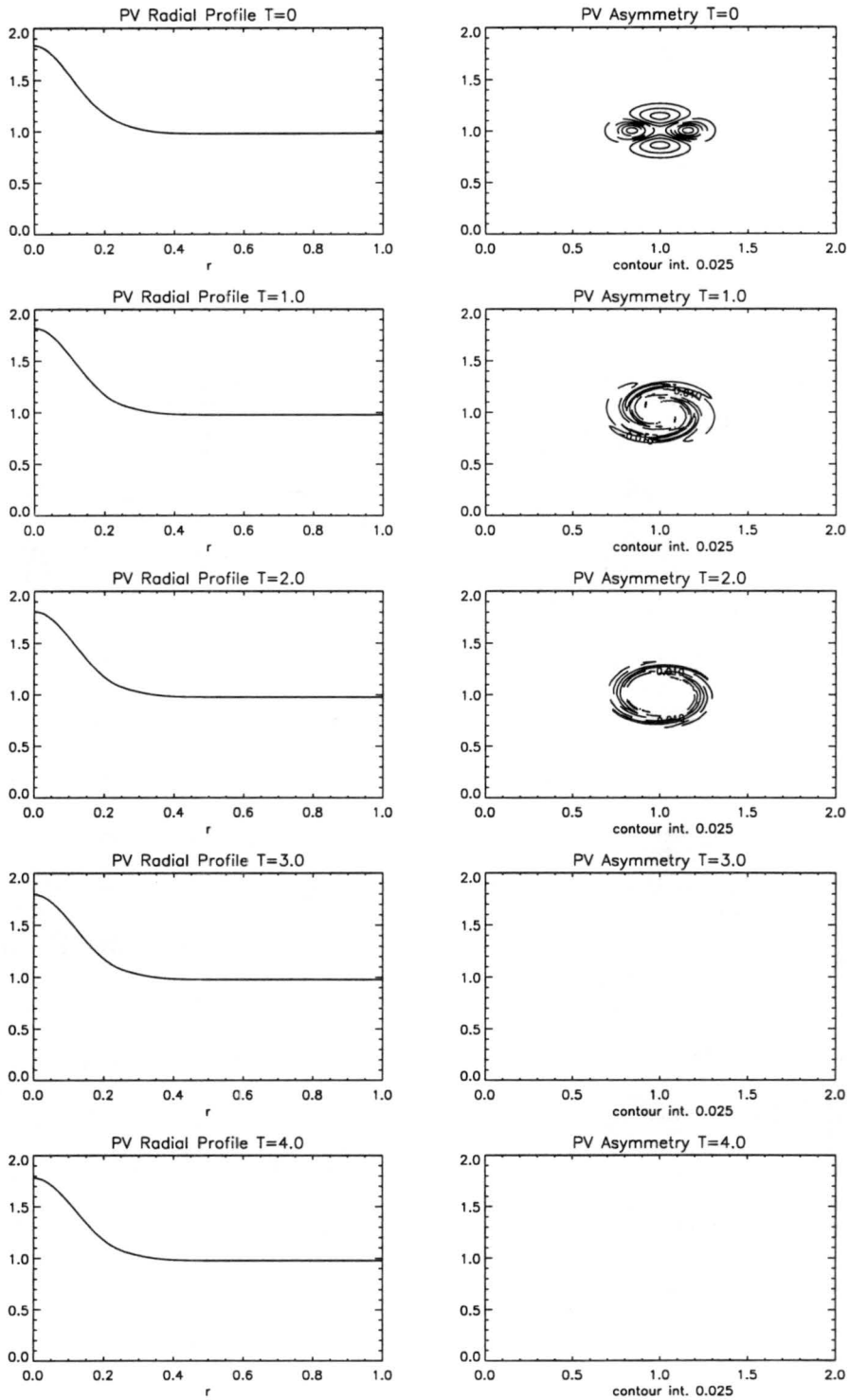

Figure 4.23: Time evolution of the azimuthal mean PV and asymmetric PV at the highest model level (z=1) for a two-cluster convective experiment with anomaly amplitudes a factor of 5 smaller than nominal (at T = 0, 1, 2, 3, 4). Anomalies are 0.15 (150 km) from the basic state vortex center.

PV and asymmetric PV on the lowest level for a two-cluster relaxation experiment in which the anomaly amplitude was increased by a factor of 3 over its nominal value. By T=3, the axisymmetrization is virtually complete except for the presence of a small wavenumber two persistent mode. The maximum spinup in this experiment is 7 ms^{-1}, yielding a final $\overline{v}_{max}$ of 11.5 ms^{-1}.

4.9 Summary

In this chapter we discussed the results of vortex axisymmetrization relaxation experiments. In combination with a basic state barotropic circular vortex, three PV anomaly cases were considered: a barotropic wavenumber two anomaly, a three-dimensional two-cluster anomaly, and a three-dimensional single-cluster anomaly, the latter two of which were intended to simulate tropical convection.

The barotropic wavenumber two run showed many expected features. The outer positive anomalies merged with the central vortex as the system symmetrized. Steepening of the radial PV profile was observed. Wavelike disturbances in the asymmetric vorticity field, identified as vortex Rossby waves, were visible. As the axisymmetrization progresses, regions of both positive and negative azimuthal mean radial vorticity gradient are evident. Thus Rossby wave packets can propagate either inward or outward in different radial regions. Spinup of the mean vortex was nevertheless a robust feature of these experiments, in agreement with the predictions of MK. Lagrangian trajectory analyses of the barotropic wavenumber two case agreed well with our other interpretations, showing that positive anomaly particles pool near the center of the vortex or move outward into positive PV filaments, whereas negative anomaly particles remain near the same radius or move outward.

The two-cluster convective run showed many features similar to the wavenumber two barotropic run, including axisymmetrization of the positive PV anomalies and the presence of wavelike disturbances in the asymmetries. At low levels, pooling of PV near the center of the vortex was observed. The Lagrangian trajectories at the lowest level confirmed the PV pooling effect. A spinup of approximately 1 ms^{-1} over 2.9 days was observed. As we

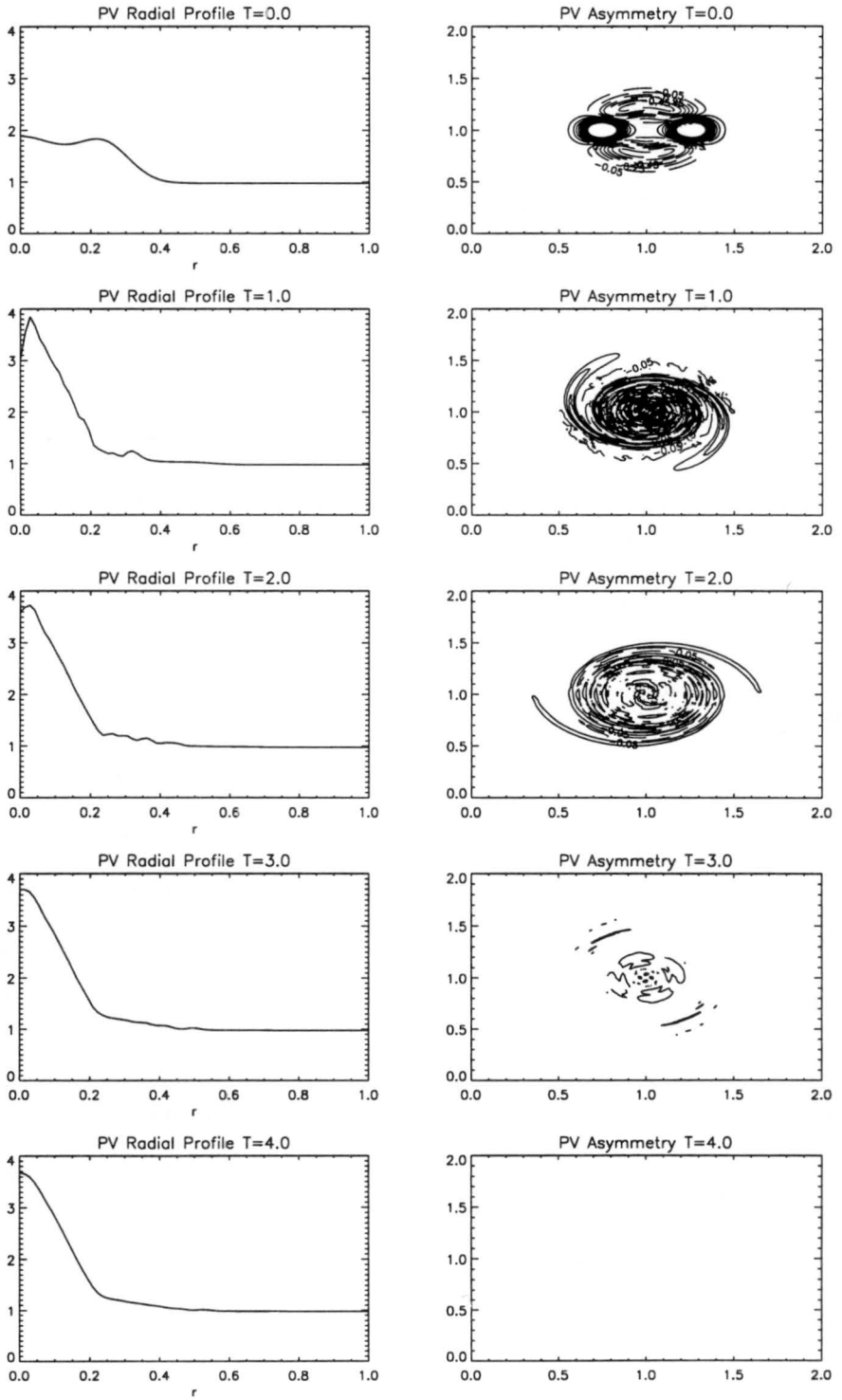

Figure 4.24: Evolution of the azimuthal mean PV and asymmetric PV on the lowest model level (z=0) for a two-cluster relaxation experiment with PV anomalies 3 times larger than the nominal amplitude. Contour interval for the asymmetry plots is 0.3.

will see in the following chapter, repeated pulses of convectively-generated PV near the radius of maximum winds can result in a spinup on the order of 10 ms^{-1} in 3.6 days.

We also considered the case of a single-cluster convective anomaly. The most important feature of this case was that, in contrast to the two-cluster cases, PV particles from the positive anomaly were transported all the way into the center of the vortex. Spinup also occurred for the single-cluster anomaly.

Finally, we considered the case of a midlevel vortex with convective forcing, of interest because mesoscale convectively-generated vortices occur at midlevels. The positive PV anomaly at low levels was pulled approximately 200 km to a position underneath the main vortex and subsequently remained aligned with it. In contrast, the negative PV anomaly at upper levels was expelled laterally from the axis of the now-aligned vortex system. This experiment illustrates that a midlevel vortex, in the process of aligning with a near-surface PV anomaly associated with peripheral convection, appears to build downward to the surface.

During the relaxation experiments warming of the vortex core was observed. Both eddy-heat and eddy-momentum fluxes contributed to the warming.

The maximum spinup $\delta\bar{v}_{max}$ in the relaxation experiments showed a greater than linear dependence on the asymmetry amplitude, indicating the presence of nonlinear feedback in the spinup process. The persistence of upper-level PV anomalies in these experiments appeared to be due to discrete neutral or unstable vortex Rossby modes propagating azimuthally around the vortex center. In a configuration in which the anomalies did not bring about a sign change in the radial PV gradient, axisymmetrization was observed at all levels.

Chapter 5

THREE-DIMENSIONAL VORTEX DYNAMICS UNDER CONVECTIVE FORCING

5.1 Pulsed Convective Studies

In the previous chapter, we described studies of the axisymmetrization of a vortex forced by initial asymmetric PV anomalies. We examined various aspects of this problem, and demonstrated that the PV anomalies cause vortex spinup.

For a more realistic model of cyclogenesis, we should incorporate the fact that convection is not simply an initial forcing condition on the vortex; convective activity is often ongoing. Convection in a tropical cloud cluster typically occurs in bursts of cumulus activity, as shown in Figure 5.1 from Zehr (1992). The figure shows a time series of convective activity in a tropical cloud cluster which eventually became Typhoon Abby in 1983. The level of convection is indicated by the fraction of the cloud cluster area with IR brightness temperature T_B less than $-65°$ C, indicative of deep cumulus convection. This observational method is described in greater detail in Chapter 6.

To simulate this multiple-burst effect, "pulses" of convective activity in the form of small-scale PV anomalies were added to the PV field at intervals (typically 0.5 τ_{eddy}, half the initial eddy turnover time of the vortex, or about 1.5 days) during the timestepping process. A pulse consisted of a PV anomaly having the same shape as the initial convective anomaly. Although the convective bursts shown in Figure 5.1 are of extended duration, this feature is impractical to simulate in our model. Rather, our PV pulses occur all at once at the chosen timestep. In the quasigeostrophic model the wind and height fields adjust instantaneously to the PV field in accord with the invertibility relation (equation (3.4)). Recall that gravity-inertia waves are excised in the balanced model. Model runs

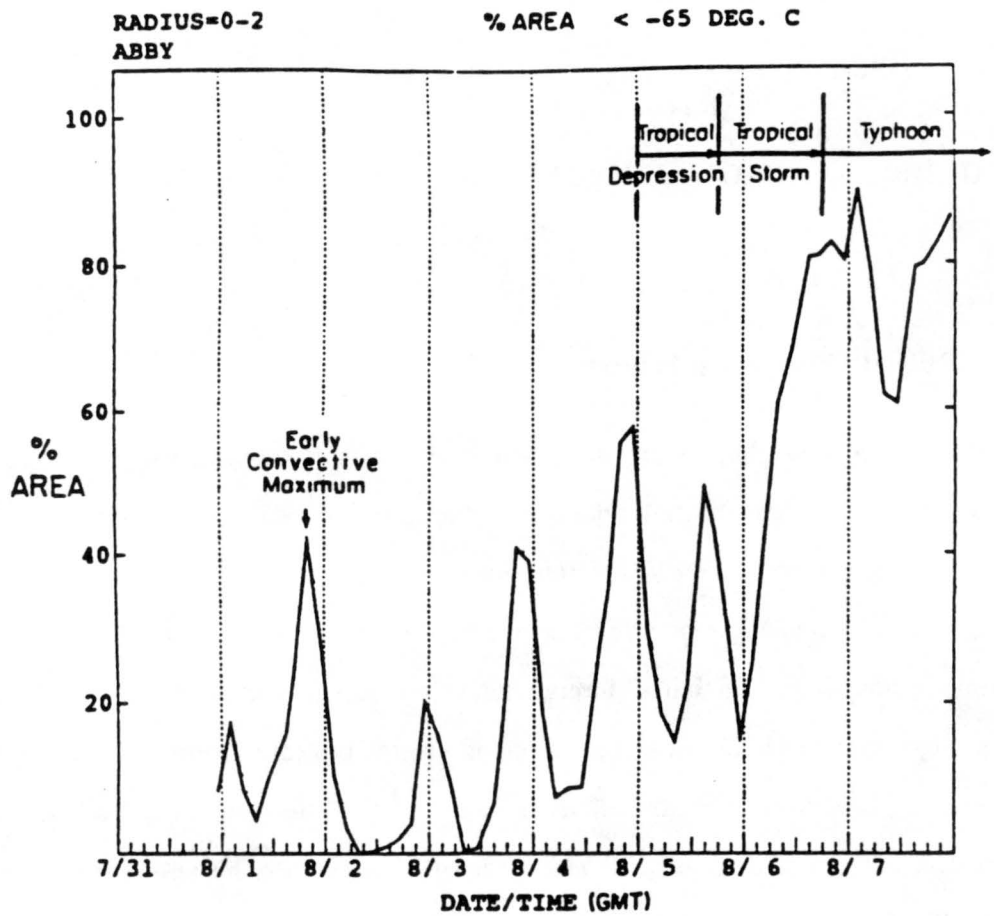

Figure 5.1: Example of a profile of convective activity for a tropical cyclone. The plot shows a time series of the percentage of the area of a tropical cloud cluster with brightness temperature T_B less than $-65°$ C, indicative of deep convection (see section 4.1). (Typhoon Abby, 1983) (from Zehr 1992).

thus consisted of an initial vortex and asymmetric PV anomaly, which were pulsed with additional asymmetric PV anomalies each 0.5 τ_{eddy}. The pulse was applied just after the model fields were written out. Since the runs were 2.5 τ_{eddy} in duration, there were typically 4 pulses in addition to the initial anomaly. Because the local shear time (see section 3.3) $\tau_{shear} = 0.2\ \tau_{eddy}$, applying a pulse each 0.5 τ_{eddy} just after the data was written out assured that the mean fields had stabilized subsequent to the pulse by the next output time.

Since the PV pulses had a z-dependence of $\cos \pi z$, as much negative as positive PV was added within the domain by each pulse, ensuring that the total PV of the fluid did not change. This is consistent with the general requirement noted in Chapter 3 that, in the absence of friction and heat fluxes on boundaries, convection merely redistributes PV such that its mass-weighted integral is invariant.

In most of the simulations described here, the pulses grew in amplitude, with the amplitude A_k of the k'th pulse given by

$$A_k = (1 + \epsilon)^k A_0 \tag{5.1}$$

where A_0 is the initial pulse amplitude and $\epsilon = 0.2$. The amplitude of the convective maximum was increased to simulate the increasing relative vorticity being converged – a primitive equation effect not captured in the strict implementation of our quasigeostrophic model which only converges planetary vorticity explicitly. The time rate of change of the potential vorticity is given by equation (3.15). Thus the amplitude of the first pulse is given by $A_1 = (1 + \epsilon)A_0$, where ϵ represents the contribution of the relative vorticity; similarly $A_2 = (1 + \epsilon)A_1 = (1 + \epsilon)^2 A_0$, and so forth. As we will see below, if the pulse amplitude does not increase, considerably less spinup is achieved.

Figure 5.2 shows the azimuthal mean PV fields and azimuthal mean tangential winds at the lowest level as a function of time for a pulsed experiment with a two-cluster convective anomaly, with pulse amplitude increasing according to equation (5.1). The vortex tangential winds increase by 10 ms^{-1}, yielding a final maximum tangential wind of 16 ms^{-1}. A plot of the change in tangential velocity $\delta\bar{v}$ at $z = 0$ after 2.5 τ_{eddy} is shown in Figure 5.3(a).

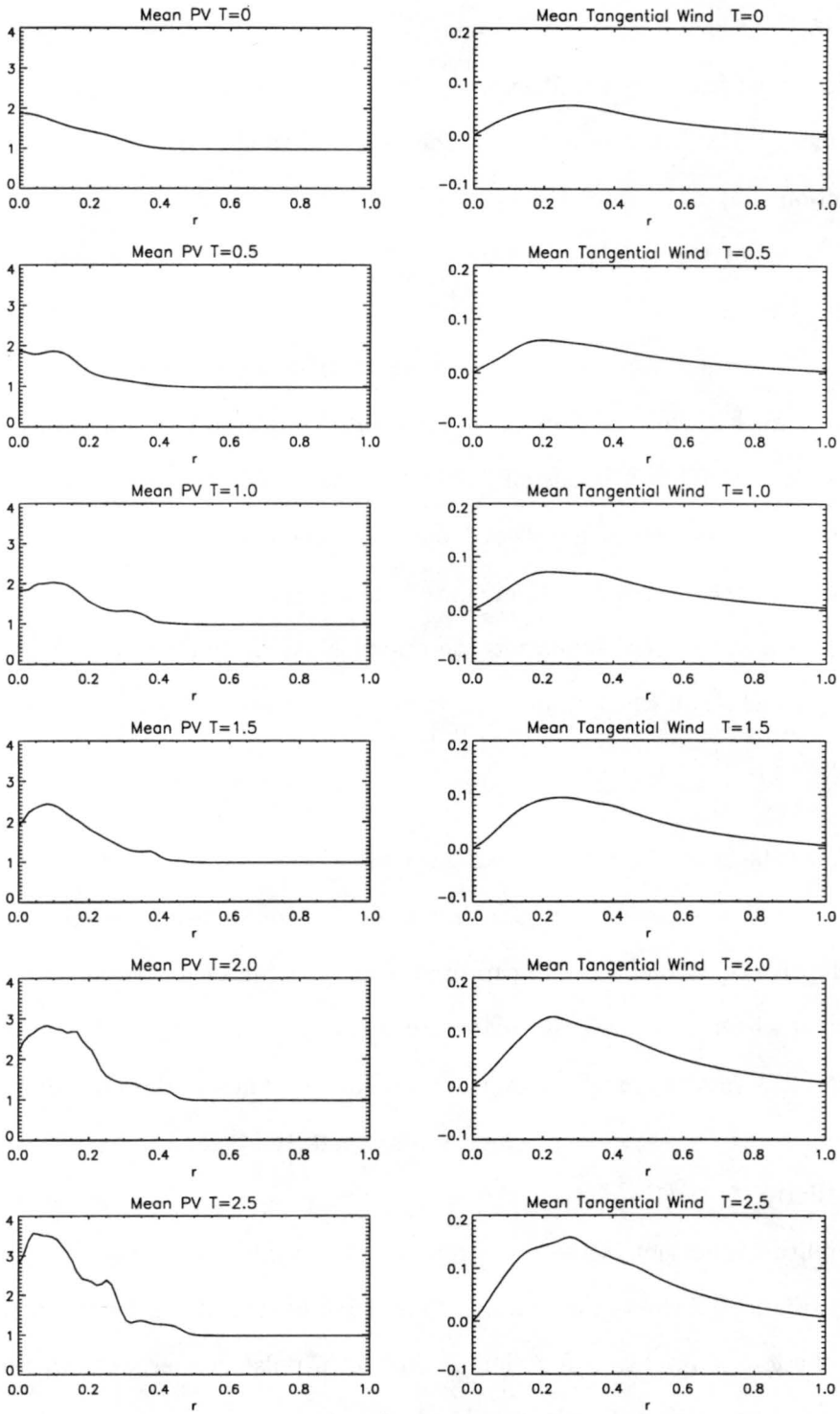

Figure 5.2: Time evolution of the azimuthal mean PV field ($\bar{Q}$) and azimuthal mean tangential wind ($\bar{v}$) at $z = 0$ for a two-cluster pulsed PV asymmetry. To obtain the tangential wind in ms^{-1}, multiply the nondimensional velocity by 100.

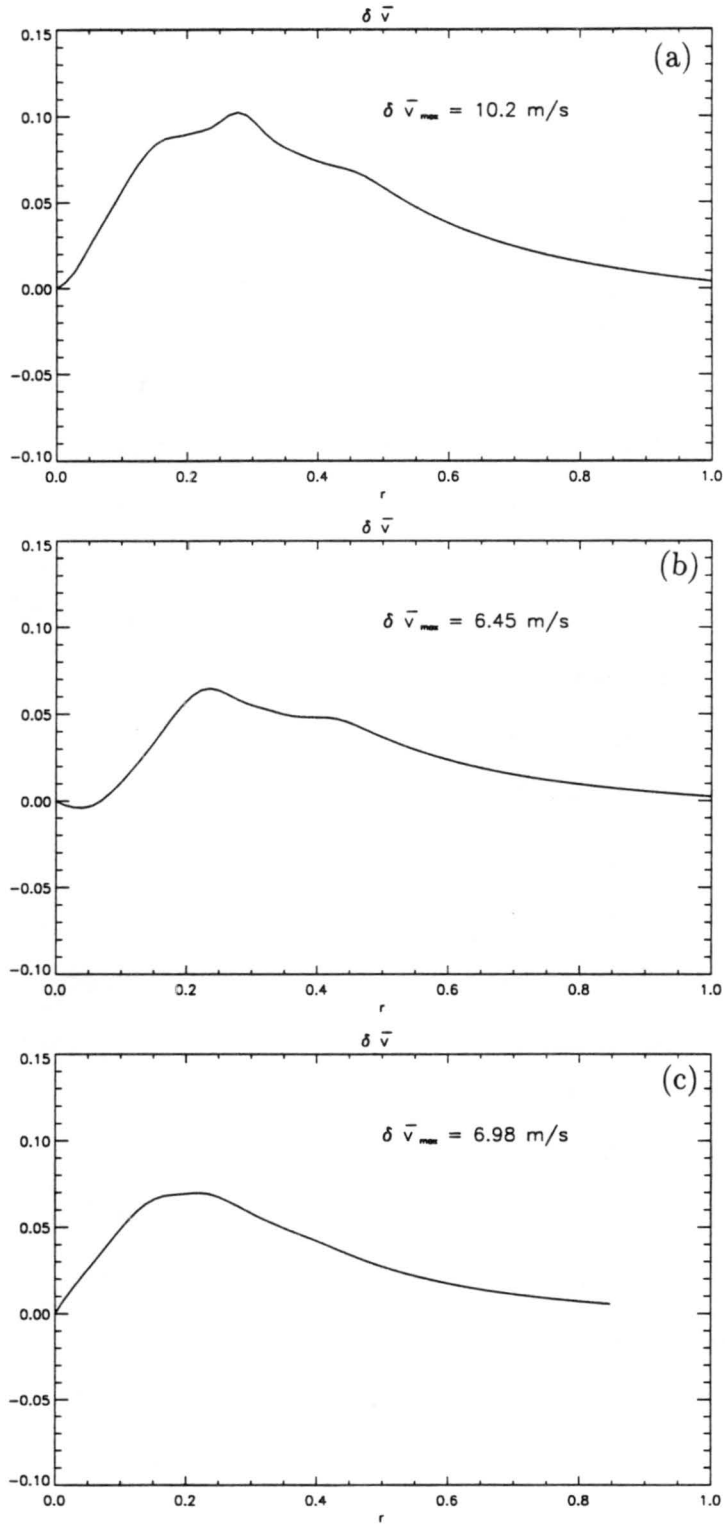

Figure 5.3: (a) Change in azimuthal mean tangential wind ($\delta\bar{v}$) at $z = 0$ after 2.5 τ_{eddy} for the two-cluster pulsed PV asymmetry. (b) Change in mean tangential wind ($\delta\bar{v}$) at $z = 0$ after 2.5 τ_{eddy} for the two-cluster pulsed PV asymmetry with constant pulse amplitude. (c) Change in mean tangential wind ($\delta\bar{v}$) at $z = 0$ after 2.5 τ_{eddy} for the single-cluster pulsed PV asymmetry. To obtain $\delta\bar{v}$ in ms^{-1}, multiply the nondimensional quantity by 100.

Figure 5.4 shows the azimuthal mean potential vorticity, flow potential temperature, flow geopotential and tangential wind plotted as a function of r and z at T = 2.5 for the two-cluster pulsed asymmetry. Anticyclonic flow at upper levels is evident. Another feature of interest is the strong ($\approx$ 5K) warm core which forms at the center of the vortex (one non-dimensional temperature unit corresponded to 30 K). In section 5.3 the formation of the warm core is discussed in detail.

Figure 5.5 shows the azimuthal mean PV fields and azimuthal mean tangential winds for an experiment in which the pulse amplitude did not grow with time ($\epsilon = 0$ in equation (5.1)). Because the successive pulses of fixed PV tend to contribute a fixed value of PV to the vortex, in this case less spinup was obtained. Since the fluid is incompressible, particles can replace but not overlap each other. Thus as the high PV particles are attracted toward the center, they tend to pile up at the outside radius of the inner PV maximum, leading to a broadening of the inner PV maximum with time. A plot of $\delta\bar{v}$ at the bottom model level for this experiment is shown in Figure 5.3(b).

Experiments with single-cluster pulsed convective forcing were also performed. Figure 5.3(c) shows $\delta\bar{v}$ for one such experiment. A spinup of approximately 7.0 ms^{-1} is obtained. As in the unpulsed axisymmetrization experiments, the single cluster anomaly gives less spinup than the two-cluster anomaly. If the low-level spinup scaled linearly with the amount of positive PV injected, the single-cluster anomaly would be expected to contribute only 50 % as much PV to the vortex as the double cluster does. Actually, it contributes considerably more than 50 %; the single-cluster anomaly appears to be more efficient at the spinup process. This greater efficiency is likely a manifestation of the nonlinear feedback effect discussed in section 4.7.

Figure 5.6 shows the time evolution of the asymmetric PV fields on the highest and lowest levels for the pulsed single-cluster asymmetry. At low to middle levels the positive anomalies are attracted into the main vortex during the symmetrization process. At high levels the negative anomalies are repelled from the main vortex; the anomalies rotate around the parent vortex and little or no axisymmetrization occurs.

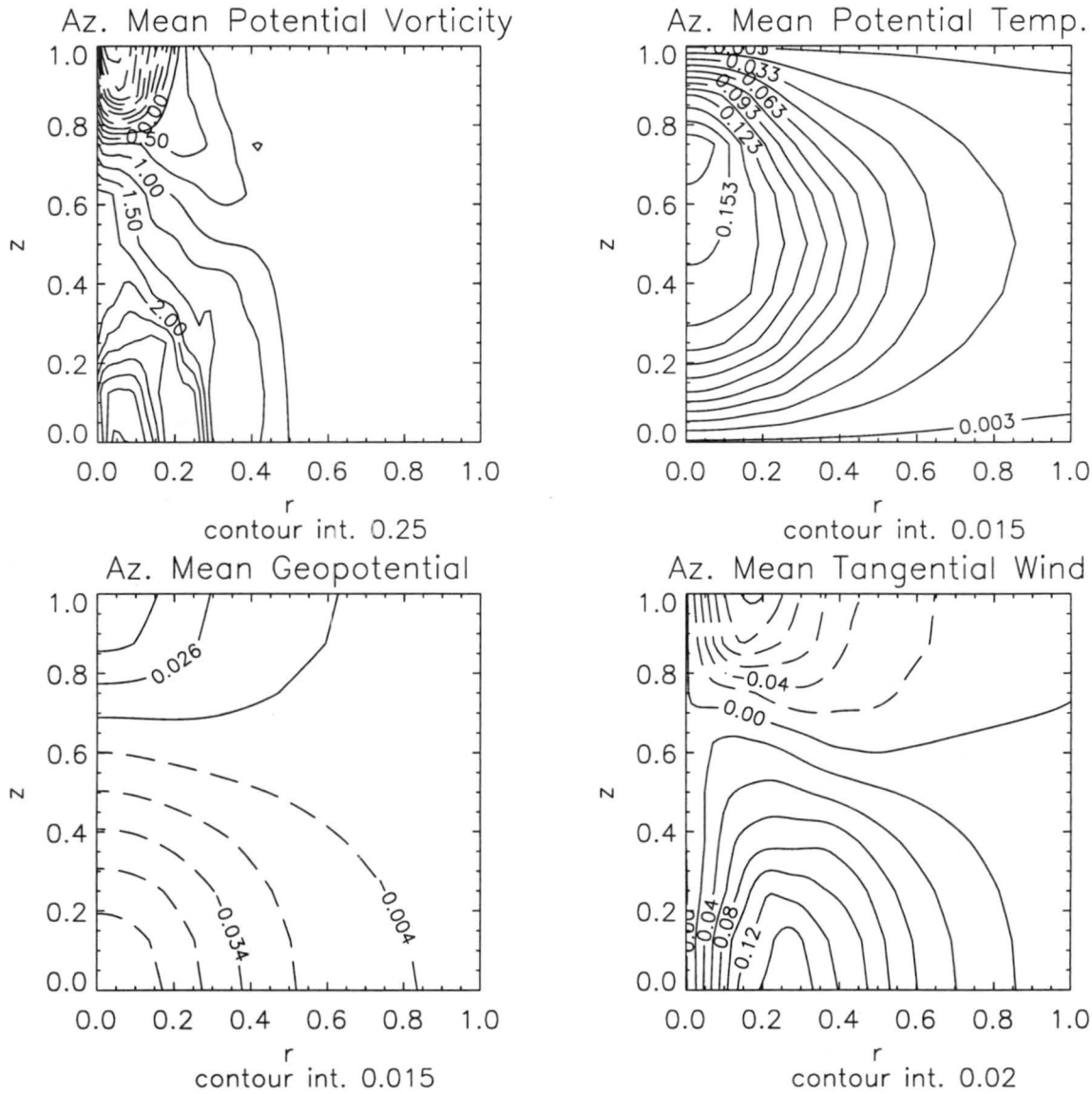

Figure 5.4: Azimuthal mean total potential vorticity $\bar{Q}(r,z)$, flow potential temperature $\bar{\theta}(r,z)$, flow geopotential $\bar{\phi}(r,z)$ and tangential wind $\bar{v}(r,z)$ for the pulsed two-cluster convective anomaly, contoured as a function of r and z, at T = 2.5. To obtain potential vorticity in PVU (10^{-6} m^2 s^{-1} K kg^{-1}), multiply the nondimensional quantity by 0.3, where a mean tropospheric density of 1.0 kg m^{-3} has been assumed. To obtain temperatures in K, multiply the nondimensional quantity by 30. To obtain geopotential in J kg^{-1}, multiply the nondimensional quantity by 10^4. To obtain velocities in ms^{-1}, multiply the nondimensional quantity by 100.

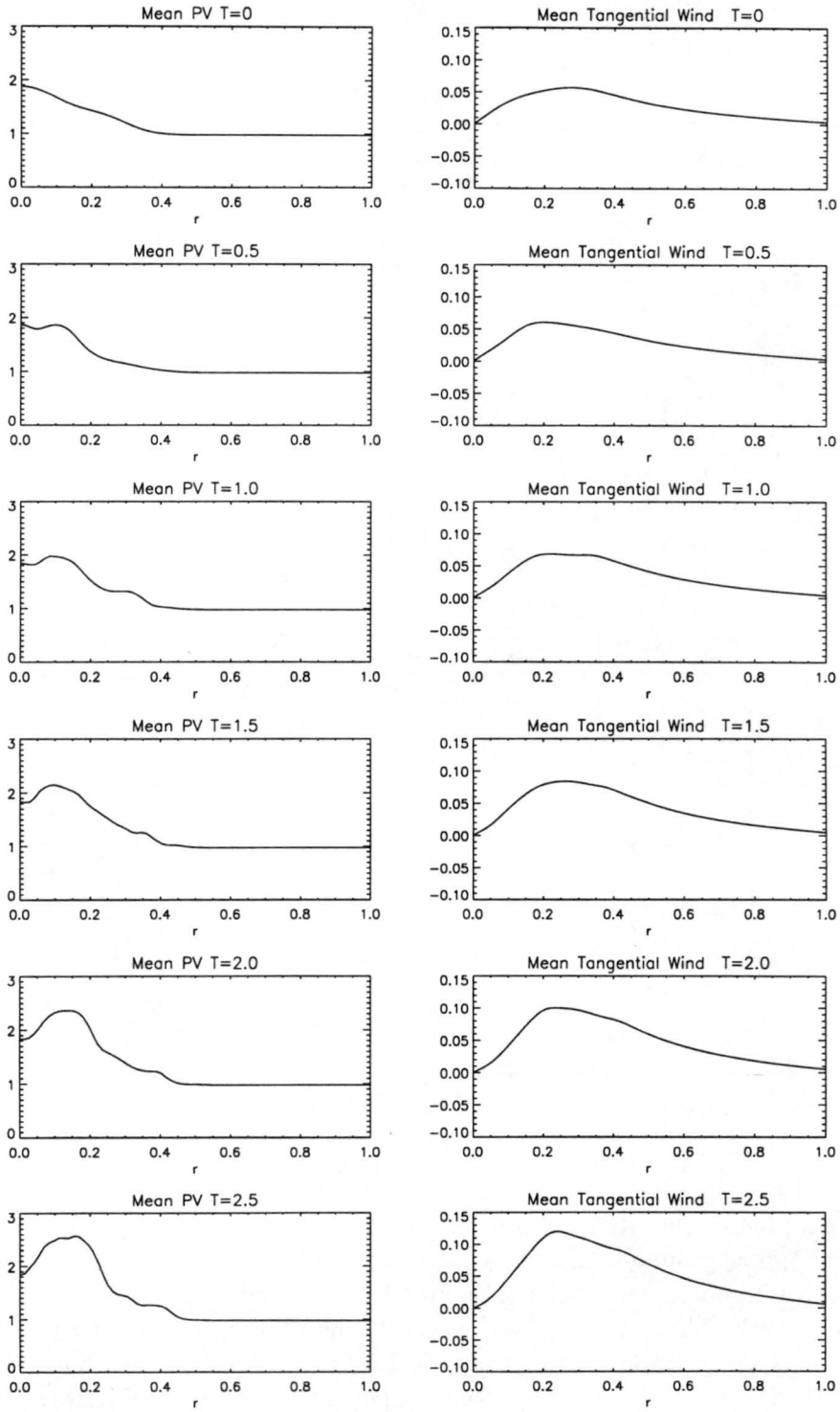

Figure 5.5: Time evolution of the azimuthal mean PV ($\bar{Q}$) and azimuthal mean tangential wind ($\bar{v}$) at $z = 0$ for a two-cluster pulsed PV asymmetry with constant pulse amplitude. To obtain the tangential wind in ms^{-1}, multiply the nondimensional velocity by 100.

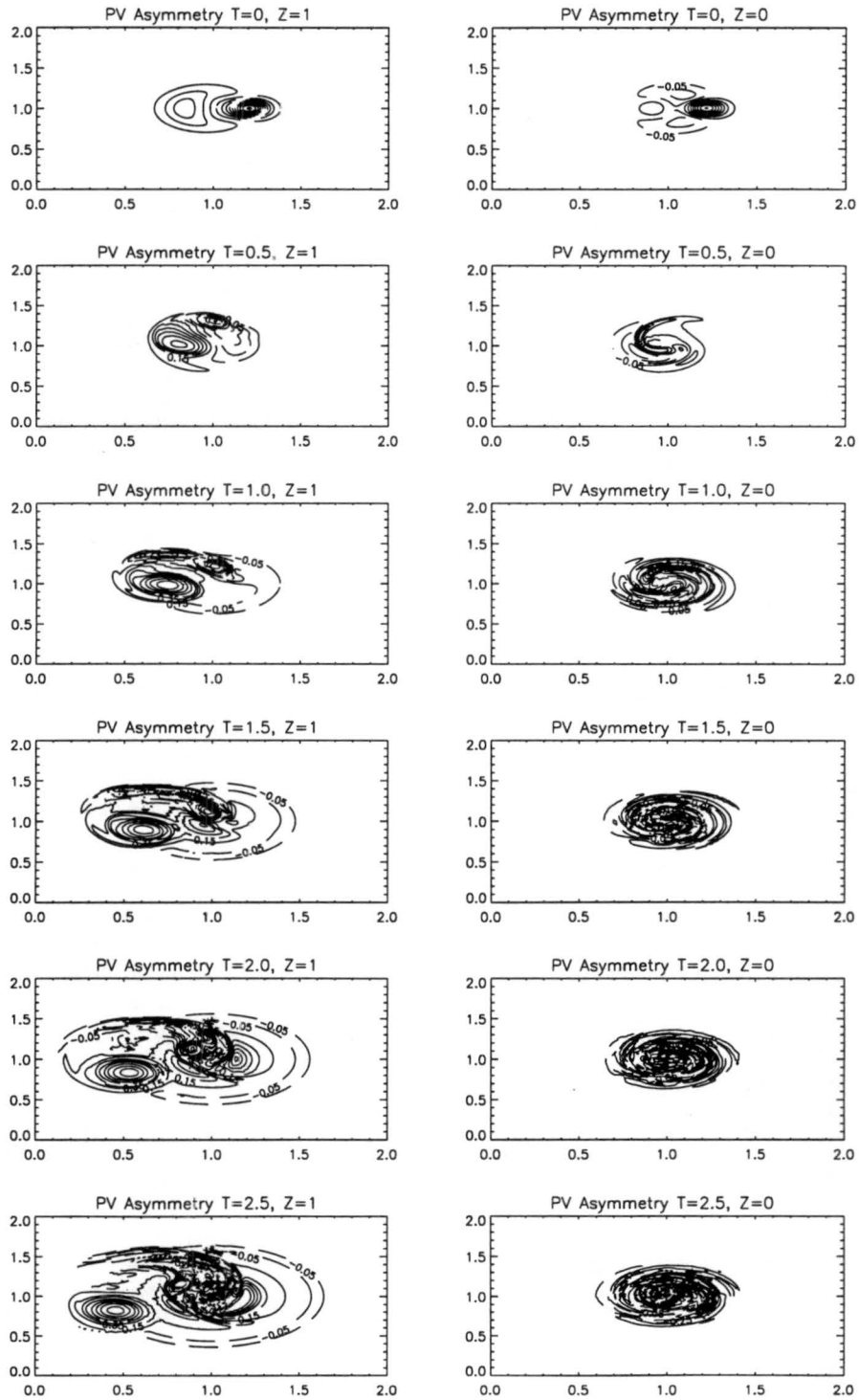

Figure 5.6: PV asymmetry fields as a function of time at $z = 0$ and $z = 1$ for the standard pulsed single-cluster convective anomaly. These z values correspond to the lower and upper boundaries, respectively. Contour interval is 0.1.

Run Type	Maximum $\delta\bar{v}$ (ms^{-1})
Nominal 2-cluster convective pulsed	10.2
2-cluster, constant pulse amplitude	6.4
2-cluster, anomalies at 400 km	4.9
2-cluster, scrambled	10.3
2-cluster, high frequency	9.4
Nominal 1-cluster convective pulsed	7.0
1-cluster high frequency	8.9

Table 5.1: Sensitivity tests of the quasigeostrophic model under convective forcing.

Figure 5.7 shows $r - z$ mean fields for the pulsed experiment with the single-cluster convective anomaly. An upper-level anticyclone and warm core can also be seen in this figure.

5.2 Sensitivity Tests

Recognizing the chaotic nature of cumulus convection, it is important to demonstrate that the hypothesis proposed here is not sensitive to details of how convection is represented in our model. Strictly speaking, this problem should be studied with a full physics model capable of adequately resolving cumulus convection and mesoscale dynamics. Such a study is beyond the scope of the present approach. As a substitute, we have performed some simple sensitivity tests with the quasigeostrophic model, which assure that our results are essentially independent of details of the pulsing scheme such as the pulse frequency and location. A summary of the sensitivity tests is given in Table 5.1.

The first of these tests showed that our results are actually quite sensitive to the radial location of the convection. We performed a simulation which was the same as the nominal two-cluster experiment except that the two convective anomalies were placed at 400 km, rather than 250 km, from the center of the vortex. The pulse amplitude in this run was increased according to equation (5.1). For the 400 km case, the tangential wind maximum broadened relative to the 250 km case. The maximum spinup, 4.9 ms^{-1}, occurred at a radius of approximately 350 km. These results are qualitatively consistent with the results for the relaxation experiments described in Chapter 4. Figure 5.8 shows the azimuthal mean tangential wind and $\delta\bar{v}$ for this experiment.

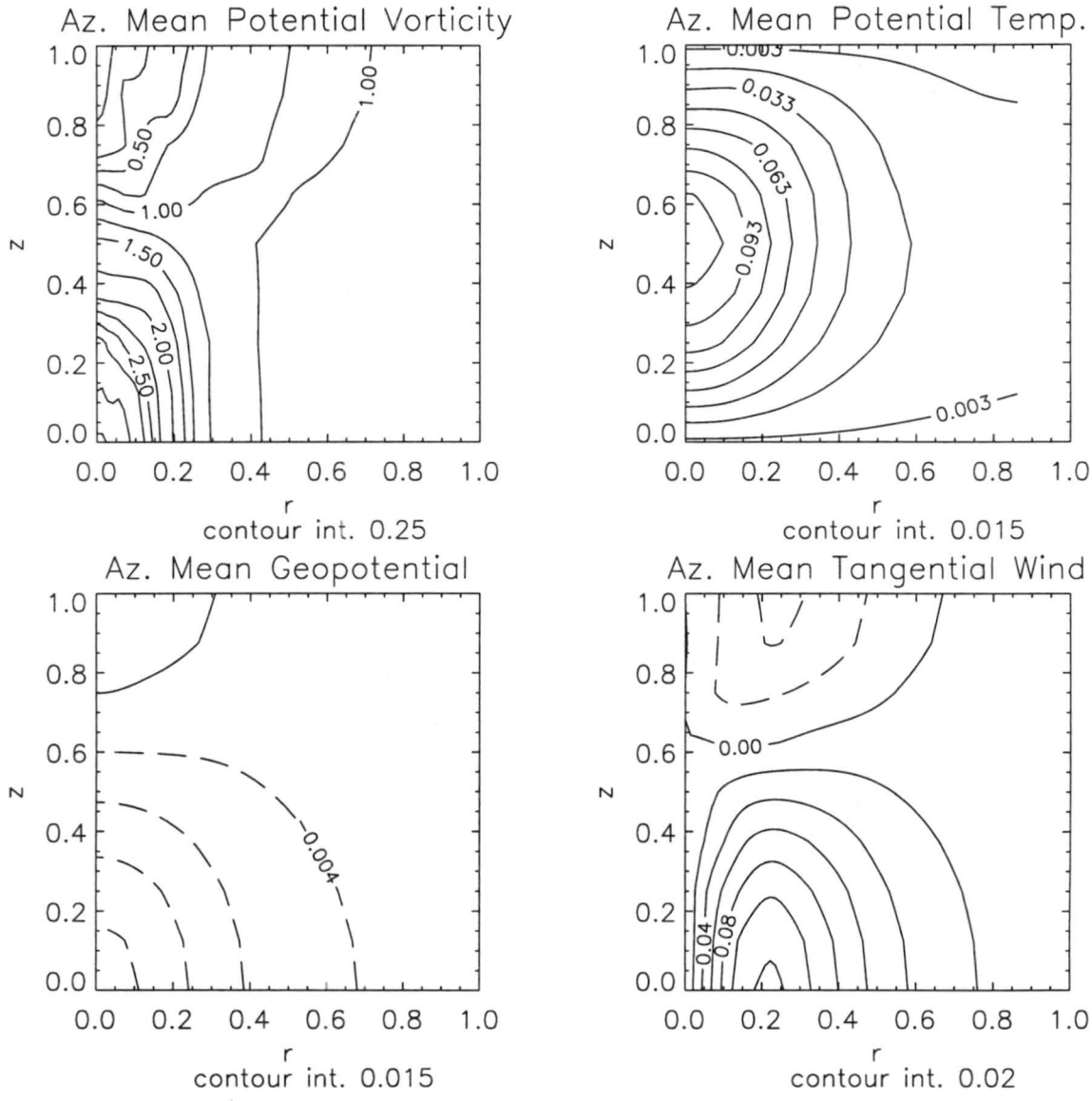

Figure 5.7: Azimuthal mean total potential vorticity $\bar{Q}(r,z)$, flow potential temperature $\bar{\theta}(r,z)$, flow geopotential $\bar{\phi}(r,z)$ and tangential wind $\bar{v}(r,z)$ for the pulsed single-cluster convective anomaly, contoured as a function of r and z, at T = 2.5. To obtain potential vorticity in PVU (10^{-6} m^2 s^{-1} K kg^{-1}), multiply the nondimensional quantity by 0.3, where a mean tropospheric density of 1.0 kg m^{-3} has been assumed. To obtain temperatures in K, multiply the nondimensional quantity by 30. To obtain geopotential in J kg^{-1}, multiply the nondimensional quantity by 10^4. To obtain velocities in ms^{-1}, multiply the nondimensional quantity by 100.

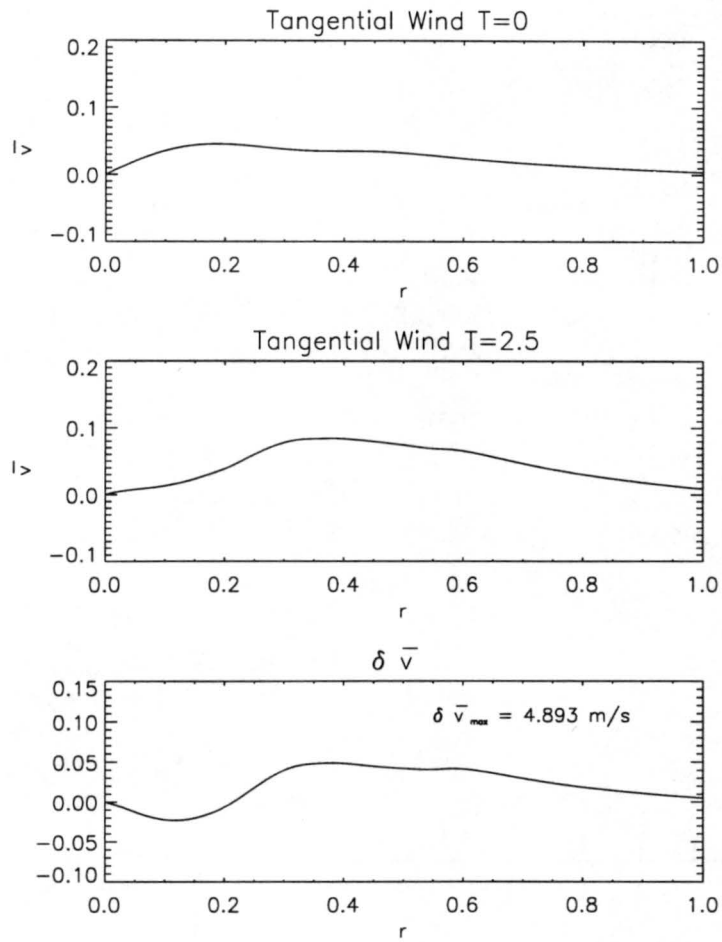

Figure 5.8: Mean tangential winds ($\bar{v}$) and change in tangential wind ($\delta\bar{v}$) at $z = 0$ for pulsed model with anomalies located at 400 km (rather than 250 km) from the vortex center. To obtain velocities in ms^{-1}, multiply the nondimensional quantity by 100.

To test for sensitivity to the pulse location when the pulse anomalies were at the same radius from the vortex but had different orientations, we created what we refer to as "scrambled" pulses. The initial two-cluster convective anomalies were located at 250 km along the x-axis as usual. However, the first secondary pulse anomalies, though also in the two-cluster configuration, were placed at 250 km along the y-axis, rotated 90° from the initial anomaly. The second pulse was rotated back 90° to the position of the initial anomaly, and thereafter the pulses alternated between these two orientations along the x and y axes. The scrambled pulse runs gave quite similar results to the normal runs, with a maximum spinup of 10.3 ms^{-1}.

The dependence of the spinup on the pulse frequency was also tested. The vortex's shear time is $5.6 \cdot 10^4$ s, while the eddy turnover time τ_{eddy} is $2.5 \cdot 10^5$ s. Since τ_{shear} is considerably less than τ_{eddy} and we normally pulse the system every 0.5 τ_{eddy}, the pulsed asymmetries tend to be sheared well before the onset of the next pulse. Thus, we expect that for a fixed total number of convective pulses, the mean tangential winds and thus the spinup should be approximately independent of the pulse frequency. To check this, we performed experiments for both the single- and the double-cluster cases with the pulse frequency doubled, but with the same total number of pulses as in the nominal runs. These experiments correspond to all of the spinup occurring in approximately 3.6 days rather than approximately 7.3. The $\delta\bar{v}$ plots for the high frequency runs are shown in Figures 5.9 and 5.10, which should be compared to Figures 5.3(a) and 5.3(c). The figures are similar and the values of maximum $\delta\bar{v}$ differ by about 1-2 ms^{-1}. Thus, as expected, the frequency of the convective pulsing in this frequency range does not significantly affect our results. In fact, if the convective anomalies were stronger, the spinup time could be considerably shorter. It should be recalled that the amplitudes used for the PV anomalies are quite conservative, given our estimate of tropical convective heating rates in section 3.7. As noted in section 4.8, in the relaxation experiments we find that axisymmetrization at middle to low levels occurs even when the PV anomaly amplitude is increased by a factor of three over its nominal value.

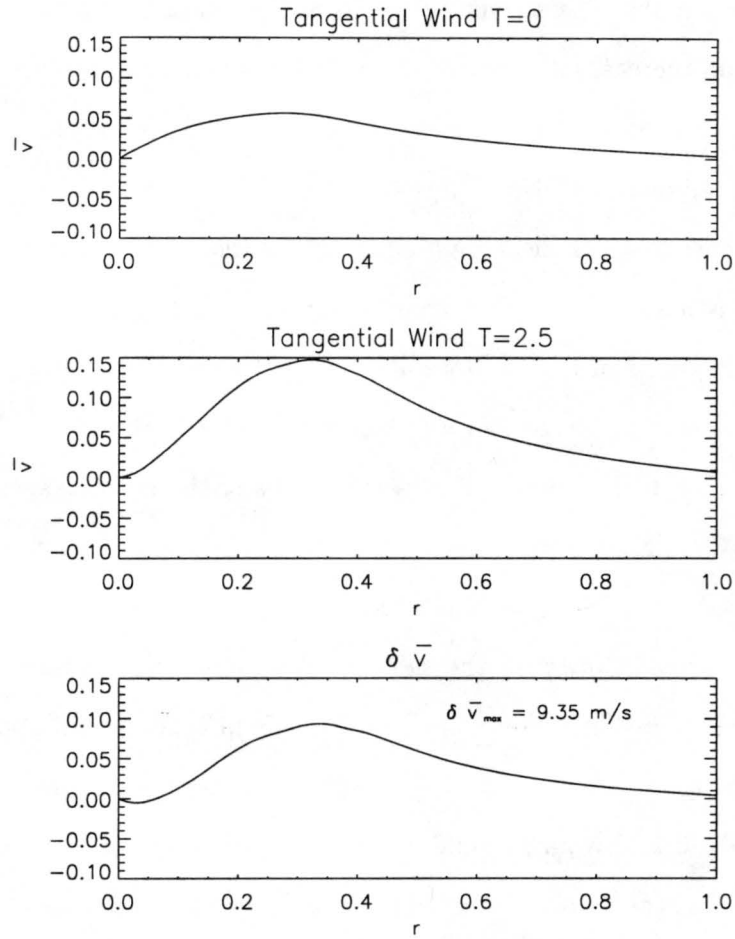

Figure 5.9: Azimuthal mean tangential winds ($\bar{v}$) and change in tangential wind ($\delta\bar{v}$) at $z = 0$ for the high frequency pulsed double-cluster experiment. To obtain velocities in ms^{-1}, multiply the nondimensional quantity by 100.

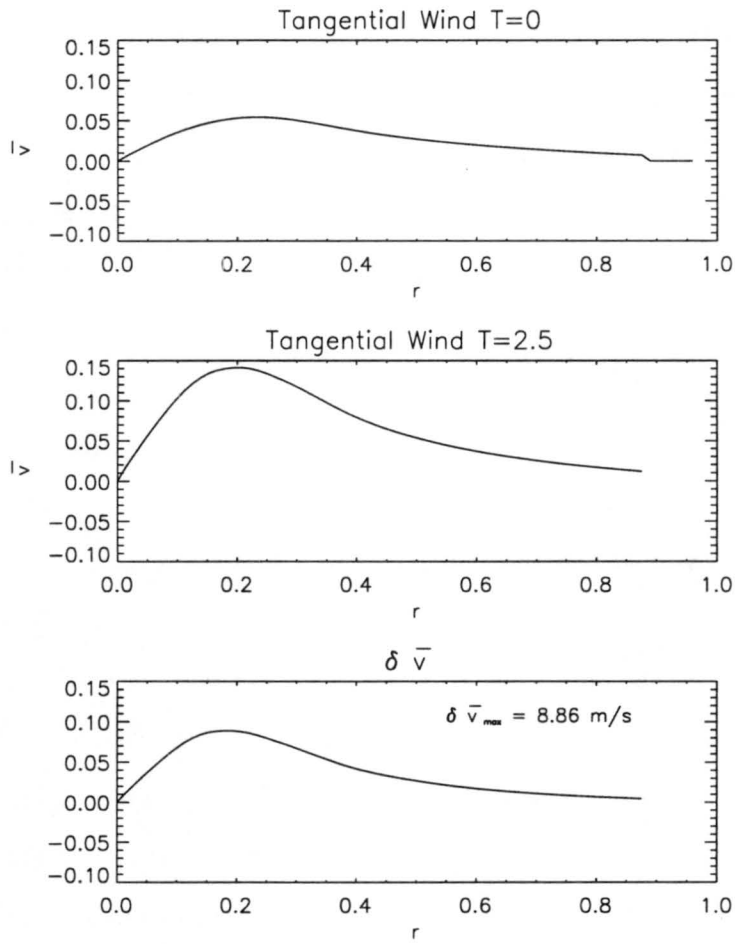

Figure 5.10: Azimuthal mean tangential winds ($\bar{v}$) and change in tangential wind ($\delta\bar{v}$) at $z = 0$ for the high frequency pulsed single-cluster experiment. To obtain velocities in ms^{-1}, multiply the nondimensional quantity by 100.

5.3 Warm Core Formation

Figure 5.11 shows the time evolution of the azimuthal mean potential temperature deviation from the resting atmosphere for the nominal two-cluster pulsed convective anomaly. As before, one non-dimensional temperature unit corresponds to 30 K. The azimuthal mean vortex has an initial warm core of approximately 0.5 K at z=0.5. The warm anomaly arises from the wavenumber zero component of the imposed asymmetry. The asymmetry induces a negative vertical shear which is maximum at $z = 0.5$. Thus thermal wind balance implies the initial warm core.

In the course of the experiment, which corresponds to 2.5 τ_{eddy} or about 7.3 days, the warm core intensifies to a 5 K level. As demonstrated above, our model can actually achieve full spinup in 1.25 τ_{eddy} or about 3.6 days. Thus we can demonstrate the buildup of a 5 K warm core on a reasonable time scale for tropical cyclogenesis. This is a significant result, as it links the formation of a warm core to the axisymmetrization process.

To investigate the mechanisms responsible for the warm core structure under multiple pulsing, we consider first the azimuthal mean vertical velocity deduced from the thermodynamic equation (3.5). Normally, in multiple-pulsed runs the pulsing occurs each 0.5 τ_{eddy}, just after the model fields and azimuthal averages are written out. Since the shear time $\tau_{shear} = 0.2\ \tau_{eddy}$, with the conventional pulsing scheme the mean field quantities have stabilized subsequent to the pulse before they are output. In order to focus on the relaxation process, we performed an additional experiment with the pulses occurring 0.5 τ_{shear} before each 0.5 τ_{eddy} output time. Thus, the outputs occurred during rather than after the symmetrization process.

Figure 5.12 shows the mean azimuthal vertical velocity on z-surfaces 0.75, 0.5 and 0.25 at T = 0.5 - 2.5. One nondimensional unit of $\bar{w}$ corresponds to 1.0 ms^{-1}. For T = 0.5 - 1.0 most of the vertical velocities are of order 0.01-0.02 cms^{-1}. These vertical velocities are too small to account for the observed temperature increase of the vortex by mean subsidence warming alone during this period. Recalling the thermodynamic equation in dimensional form,

$$\frac{\partial \theta}{\partial t} = -\mathbf{u} \cdot \nabla \theta - \frac{\theta_0}{g} N^2 w, \tag{5.2}$$

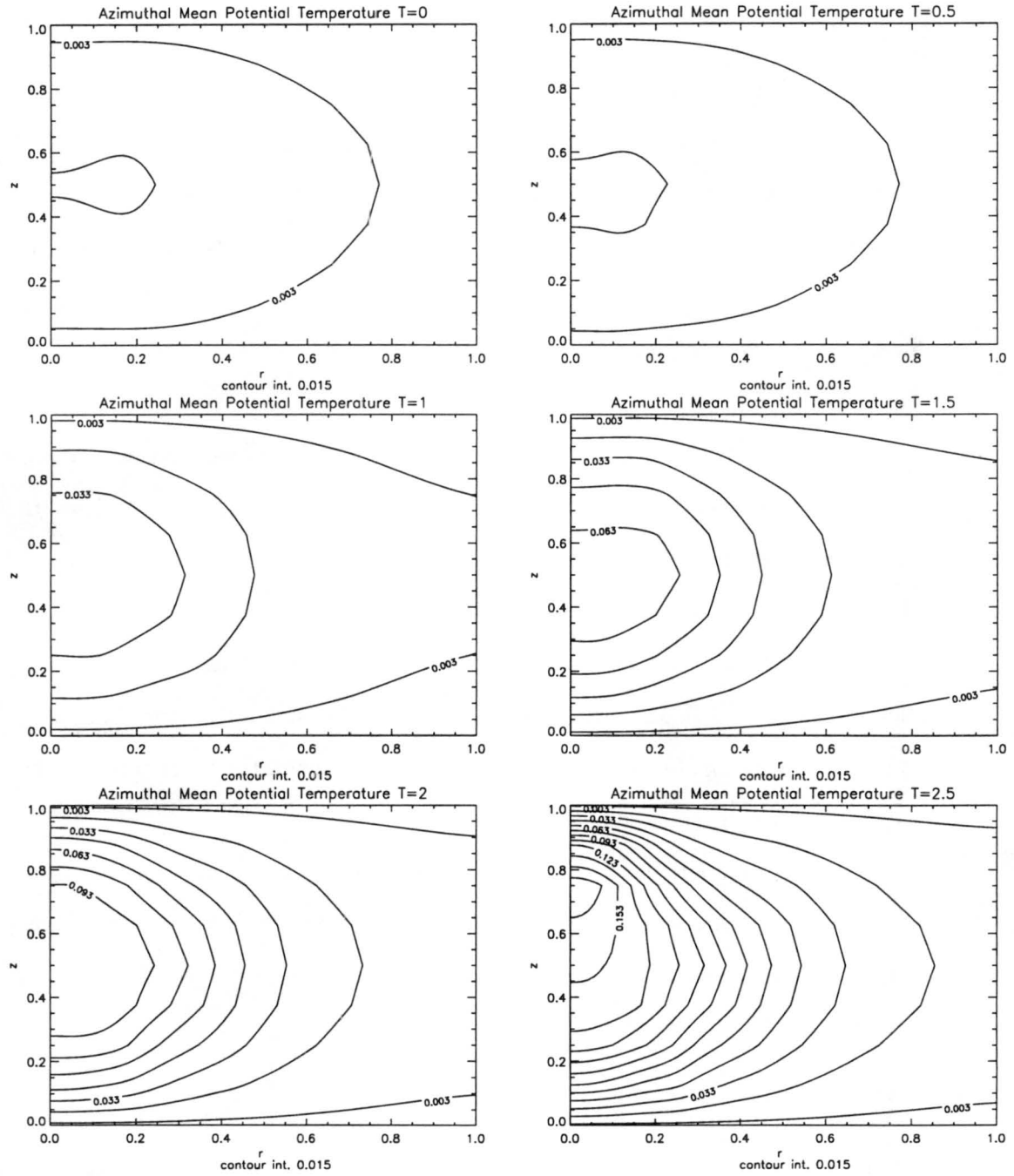

Figure 5.11: Time evolution of the azimuthal mean potential temperature deviation from the resting atmosphere for the nominal pulsed two-cluster convective experiment. One nondimensional temperature unit corresponds to 30 K.

in 1.0 τ_{eddy} the expected temperature change of the vortex core due to such mean subsidence is

$$\Delta\theta \approx \frac{\theta_0}{g} N^2 w \tau_{eddy} \approx 0.075 - 0.15 \text{ K}$$

The observed mean warming in the first τ_{eddy} is approximately 2 K.

By T=1.0, however, the z=0.25 level shows a subsidence of nearly 0.1 cms^{-1}. Vertical velocities at the other displayed levels remain small until T=2.0, when we observe mean subsidence at all levels within the radius of maximum winds with maximum vertical velocities in the range 0.1 - 0.4 cms^{-1}. Subsidence of order 0.1 cms^{-1} then persists at all levels in the inner core through T=2.5. Thus, we expect subsidence warming to be more significant at later times during the run.

The results for $\bar{w}$ are consistent with the plots of the Sawyer-Eliassen forcing terms, which are shown in Figure 5.13. For example, at T=1.5 at the z=0.25 level the total forcing is increasing as one moves outward from r=0 to r=0.15. As noted in our earlier discussion of the Sawyer-Eliassen forcing for the simple relaxation experiment, it follows that $\overline{\psi}$ is decreasing, and therefore that $\bar{w}$ is negative; this agrees with the $\bar{w}$ plots which show significant subsidence in the inner core at this level. On the other hand, at z=0.75 at the same time the forcing is essentially constant through the inner core; consequently, the vertical velocities are small at the upper level.

At T=2.0, the forcing at z=0.25 in the inner core is again increasing with radius, so we also expect subsidence in this case. Since the total forcing is significantly stronger, we predict a larger value of $\bar{w}$; the observed maximum value increases from 0.08 cms^{-1} to 0.25 cms^{-1}.

5.4 Summary

In this chapter we considered the problem of three-dimensional axisymmetrization of a vortex under convective forcing. Convection was represented by pulsed potential vorticity anomalies whose magnitude and vertical structure are consistent with observations of cumulus heating (see section 3.7). Vortex intensification proceeds by ingestion of like-sign PV anomalies into the parent vortex and expulsion of opposite-sign anomalies during

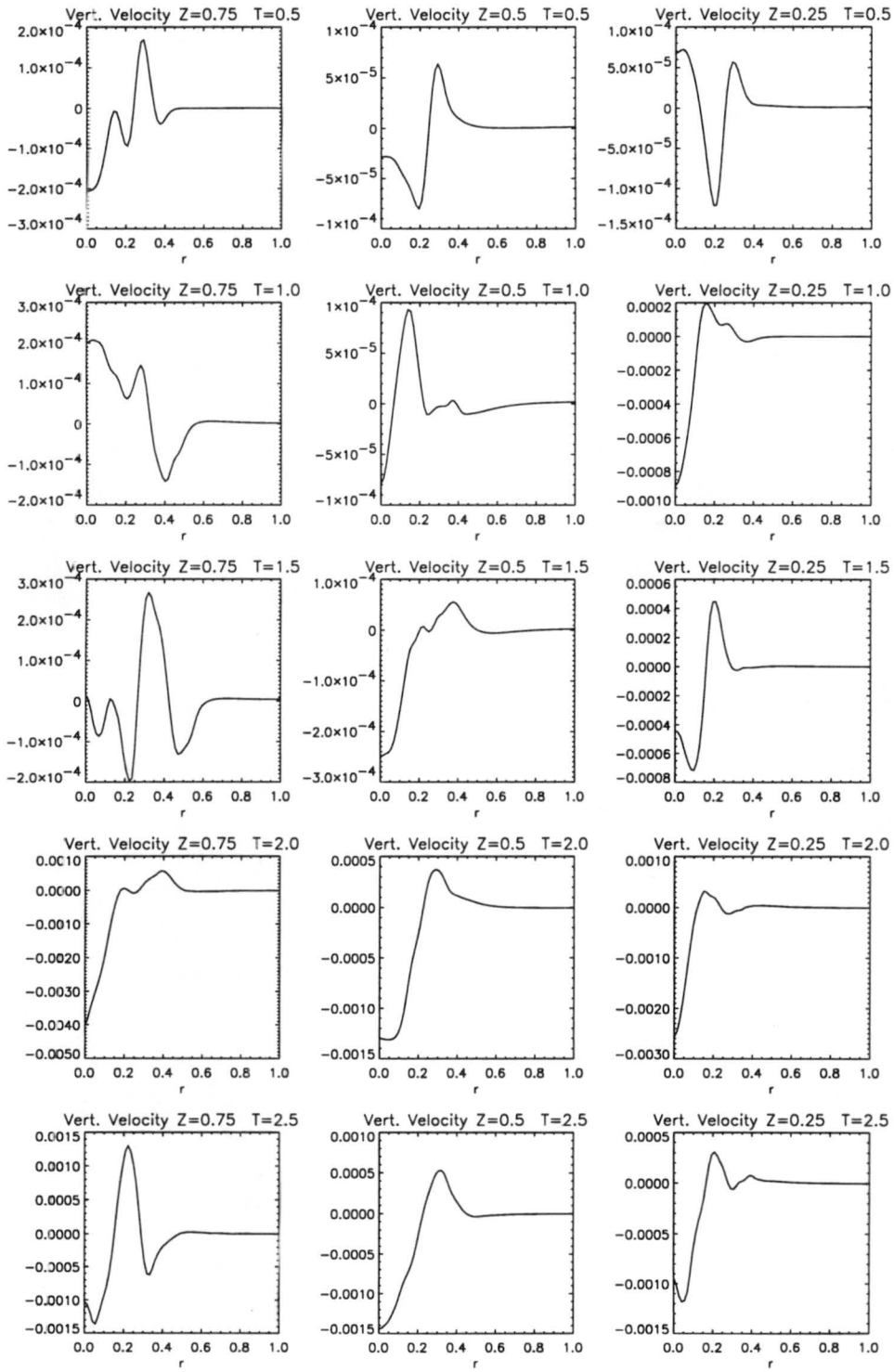

Figure 5.12: Azimuthal mean vertical velocity $\bar{w}$ at model levels z=0.75, 0.5 and 0.25 at T=0.5, 1.0,1.5, 2.0, and 2.5 for a two-cluster pulsed experiment with pulses applied 0.5 τ_{shear} before each 0.5 τ_{eddy}. One nondimensional vertical velocity unit equals one ms^{-1}.

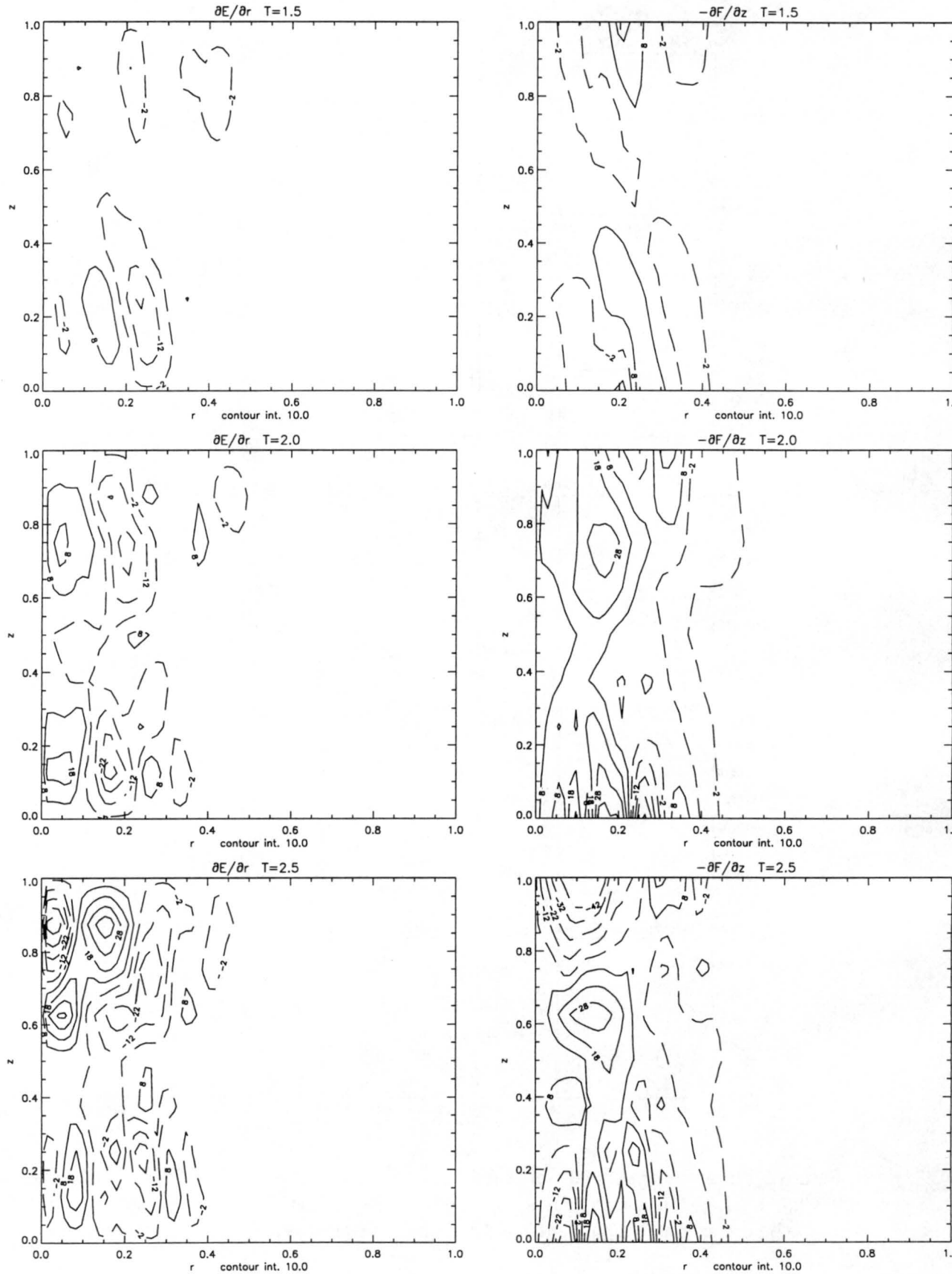

Figure 5.13: Momentum flux and heat flux forcing terms for the Sawyer-Eliassen equation as a function of time for the two-cluster convective experiment with pulses applied 0.5 τ_{shear} before each 0.5 τ_{eddy}. To obtain the forcing terms in s^{-3}, multiply by 10^{-13}.

the axisymmetrization process. Vortex spinup is sensitive to the radial location of the convection. If the convection occurs far from the main vortex the inner-core winds do not increase significantly.

Significant spinup on realistic time scales requires convergence of relative as well as planetary vorticity. A warm core develops in association with the intensification of the winds. Both eddy-heat and eddy-momentum fluxes contribute to the development of the warm core.

Chapter 6

COMPARISON WITH OBSERVATIONS

6.1 Introduction

In this chapter we discuss observations concerning tropical cyclogenesis which are relevant to our work. We examine two sets of observations: the study of Zehr (1992) based on satellite, aircraft and conventional data and the rawinsonde composite study of Lee (1986, 1989a, 1989b).

6.2 Observations of Tropical Cyclogenesis: Zehr's Results

An extensive observational study of tropical cyclogenesis in the western North Pacific is provided by Zehr (1992). The satellite data in Zehr's study consisted of digitized infrared and visible data from the Geostationary Meteorological Satellite with data available since 1977. This data set had the advantage over hard-copy satellite images that large amounts of data could be quickly analyzed with consistent and objective algorithms. In the IR data, the brightness temperature T_B measures the radiative temperature of clouds or the Earth's surface. In tropical regions horizontally large, very cold IR areas occur due to deep cumulonimbus convection and mesoscale convective systems, since clouds with very cold T_B have tops near the tropopause. The IR data were analyzed with respect to the moving center of the cyclone or disturbance. Details of the center finding algorithm are described in (Zehr 1992).

Typical satellite analysis results for the Zehr study are time series of the fraction of cloud areas with $T_B < -65°$ or $-75°$C for a given disturbance. An example is shown in Figure 5.1. Pertinent to our work is the occurrence of multiple bursts of convection, at intervals of approximately 24 hours, prior to the tropical depression designation. These

convective bursts are incorporated in our model as "pulses" of convective activity (see section 5.1).

6.3 Observations of Tropical Cyclogenesis: Lee's Rawinsonde Results

We have also examined the results of a published rawinsonde composite study of tropical cloud cluster evolution and cyclogenesis in the western North Pacific (Lee 1986, Lee 1989a, Lee 1989b). This study was a major improvement over previous ones in that it used 21 years of data rather than the 10 year set used previously (Zehr 1976; McBride 1979, 1981a,1981b; and McBride and Zehr 1981). The increase in data allowed the use of stricter composite criteria and better estimates of time rates of change (crucial to the results here). Also, better satellite data were available for selecting non-genesis cloud clusters for study, and finding the centers of the clusters.

In his study, Lee compared a composite of 341 selected developing cyclones to 332 "nonpersistent nongenesis" and 328 "persistent nongenesis" tropical cloud clusters. The nongenesis clusters were required to be at least 4° in diameter and not elongated in shape, located in the region of interest, and not associated with a cyclone or precyclone system. Clusters which could be observed only within one 24-hour time period were defined as non-persistent nongenesis (NN) clusters, and those which were visible for two or more days were termed persistent nongenesis (PN) clusters. Developing cyclones are signified by GN. Determination of center positions for the nongenesis and genesis cases is described in (Lee 1986, Lee 1989a).

To study time evolution, composites for the developing cyclones were formed for various evolutionary time stages. The cyclone system was selected for inclusion in the composites when it was identified as a tropical depression. This was defined as evolutionary Stage 3. Stage 3 included the first two 12-hour time periods following identification as a tropical depression. Stage 4 included the two 12-hour periods immediately after Stage 3, Stage 2 included the 24 hours immediately before Stage 3, and Stage 1 included the 24 hours prior to Stage 2.

Extensive comparisons were made between the genesis and nongenesis composites. Here we will discuss only those comparisons which are directly relevant to our results.

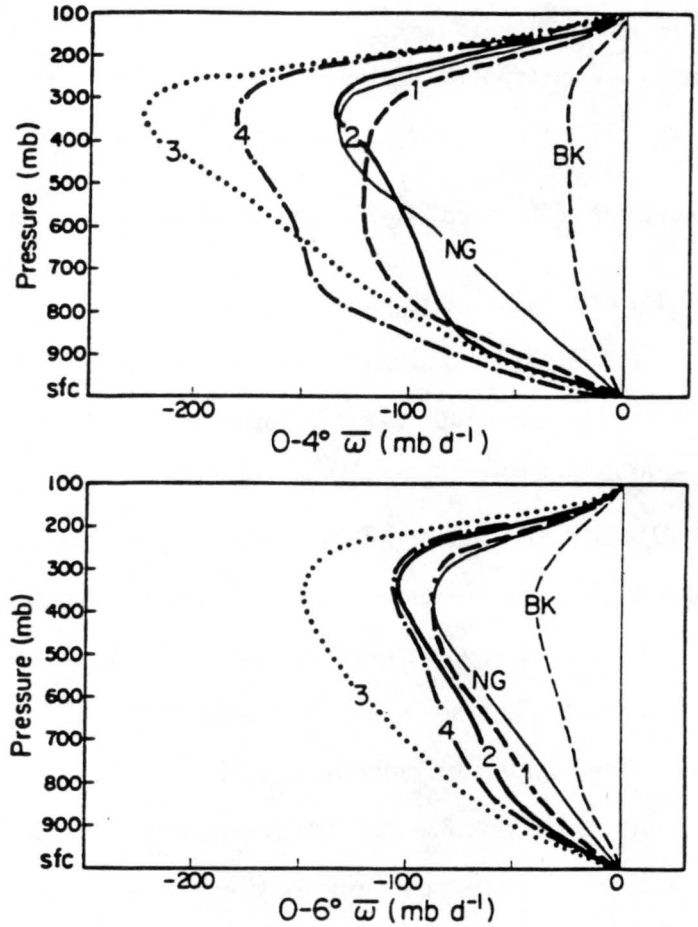

Figure 6.1: Azimuthal mean vertical motion ($\bar{\omega}$) averaged over 0°- 4° and 0°-6° radius for genesis Stages 1-4 and for the nongenesis case (NG). BK is a background profile. (From Lee 1989a)

Azimuthal mean vertical motions ($\bar{\omega}$) averaged over 0°- 4° and 0°-6° radius were derived using the kinematic method by assuming zero vertical motion at the surface and 100 mb. The vertical motion profiles are shown in Figure 6.1. The $\bar{\omega}$ distributions for nongenesis and genesis (Stage 2) cases were approximately the same. However, for the genesis composite between Stage 2 and Stage 3 there was a large increase in upward vertical motion, which then decreased again for Stage 4, suggesting that, in agreement with Zehr's work, an outbreak of cumulus activity occurred shortly prior to the tropical depression designation.

A cross section of the azimuthal mean tangential wind for the NN, PN and genesis cases is shown in Figure 6.2. The genesis case initially shows stronger cyclonic circulation at mid to low levels, which rapidly increases as the winds evolve in time. This is one of the major differences between the genesis and nongenesis composites.

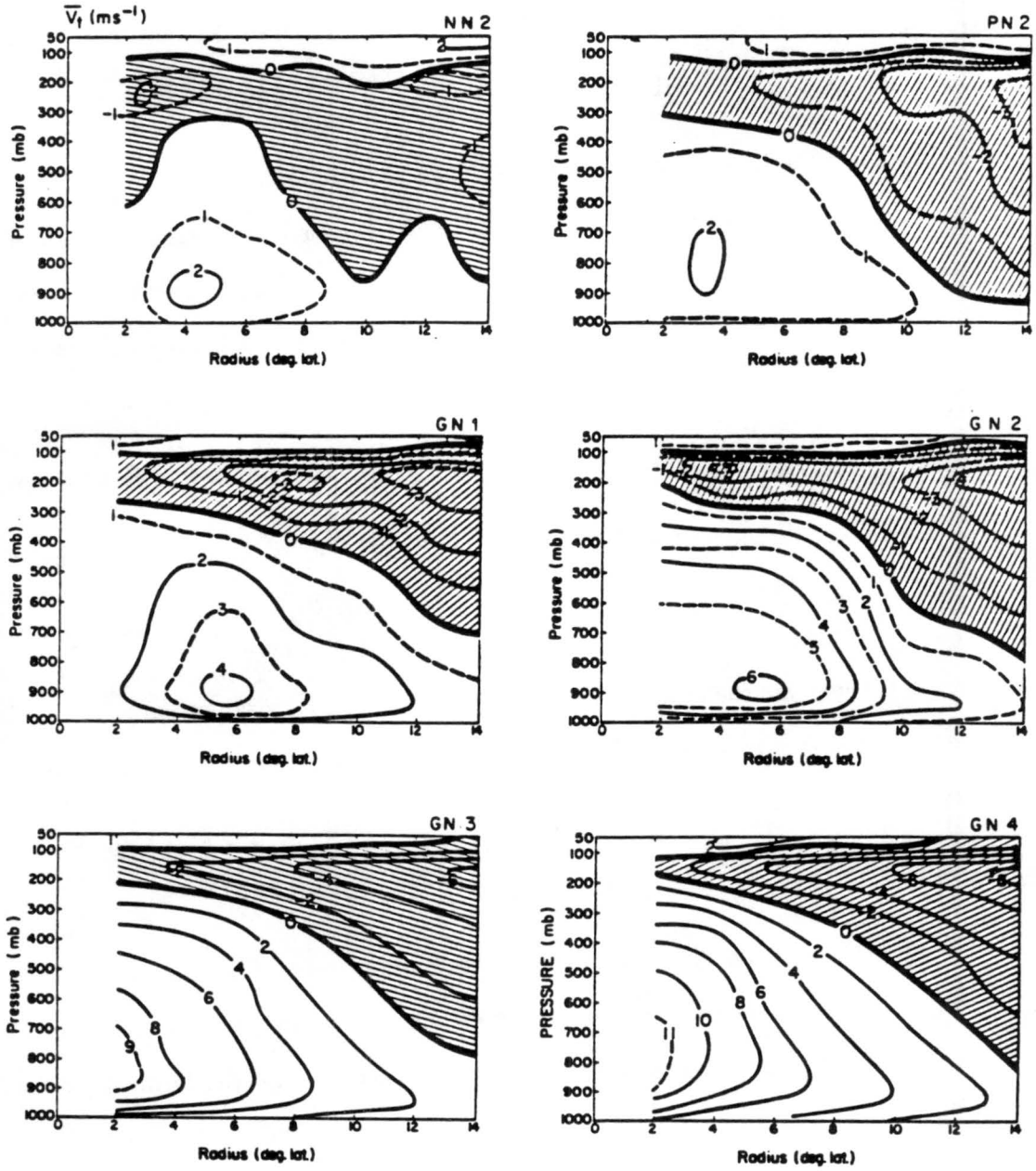

Figure 6.2: Cross sections of the azimuthal mean tangential wind in ms^{-1} for genesis Stages 1-4 and for the NN and PN composites at Stage 2 (from Lee 1989a).

As a test of the applicability of our quasigeostrophic model, it is of interest to note the Rossby numbers at the radius of maximum winds corresponding to Figure 6.2. At genesis stage 1

$$\mathrm{Ro} = \frac{4 \text{ ms}^{-1}}{(2.8 \cdot 10^{-5} \text{ s}^{-1})(5.5 \cdot 10^{5} \text{ m})} = 0.26 \ll 1;$$

for this stage of genesis the QG approximation is a good one. For genesis stage 3

$$\mathrm{Ro} = \frac{9 \text{ ms}^{-1}}{(3.5 \cdot 10^{-5} \text{ s}^{-1})(2 \cdot 10^{5} \text{ m})} = 1.3;$$

at this stage the QG approximation is no longer strictly applicable.

The source of the increase in cyclonic circulation was investigated using a tangential momentum budget analysis in a coordinate system moving with the storm system. Denoting the azimuthal mean tangential wind by $\bar{v}$, its depth-integrated time rate of change is given by

$$\int_{\text{troposphere}} \frac{\partial \bar{v}}{\partial t} dp = \text{mean terms} + \text{eddy terms} + \text{motion terms} + \text{surface friction.}$$

The mean term is the part of $\partial \bar{v}/\partial t$ which can be determined by the mean circulation:

$$\text{mean term} = \int_{\text{trop.}} \left(- \overline{u}\bar{\zeta}_r - \overline{u}\overline{f} - \overline{\omega}\frac{\partial \overline{v}}{\partial p} \right) dp.$$

Here $\bar{u}$ is the azimuthally averaged radial wind and $\bar{\zeta}_r$ is the azimuthally averaged relative vertical vorticity. The motion term signifies the spin-down of the system due to its northward motion; this can be calculated from

$$\text{motion term} = \int_{\text{trop.}} -\overline{c_r f} dp,$$

where c_r is the radial component of the system motion and the bar denotes an azimuthal average. Details of how the system motion is estimated are given in Lee's papers. Following Frank (1977) the surface term is estimated using Deacon's empirical formula for the drag coefficient and various other small corrections (Lee 1989b). The mean, motion and surface friction terms can be determined from the composited data. The eddy term is calculated as the residual of the other terms; it includes any other residual effects such as data errors. It is important to note that any vertical fluxes of angular momentum are also included in Lee's eddy term.

	$\frac{\partial \bar{v}_\theta}{\partial t}$ ($ms^{-1}day^{-1}$)	=	mean terms	+ eddy terms	+motion terms	+surface friction
$1° - 5°$						
Non-Non	0	=	+0.4	-0.1	-0.2	-0.1
Per-Non	0	=	+0.4	-0.1	-0.2	-0.1
Gen-S1	+1.7	=	+0.7	+1.6 (70 %)	-0.3	-0.3
Gen-S2	+2.0	=	+1.4	+1.6 (53 %)	-0.4	-0.6
Gen-S3	+1.8	=	+2.6	+0.7 (21 %)	-0.4	-1.1
$5° - 9°$						
Non-Non	0	=	-0.1	+0.6	-0.4	-0.1
Per-Non	0	=	+0.1	+0.4	-0.4	-0.1
Gen-S1	1.2	=	+0.4	+2.0 (83 %)	-0.8	-0.4
Gen-S2	0.0	=	+0.3	+1.2 (80 %)	-0.9	-0.6
Gen-S3	0.2	=	+0.4	+1.4 (78 %)	-1.0	-0.6

Table 6.1: Lee's tangential momentum budget analysis (from Lee 1989b). Units are $ms^{-1}day^{-1}$.

Lee's tangential momentum budget results are shown in Table 6.1. It is evident that for the genesis case the contributions from the eddy terms are quite large compared to all other terms, particularly at Stages 1 and 2.

The importance of the eddy terms in the early stages of cyclogenesis is consistent with our theory, which posits large inward fluxes of eddy angular momentum on sub-synoptic scales ($1° - 5°$) subsequent to each convective burst. However, because Lee's eddy term is determined by the residual method, Lee's large eddy fluxes cannot be directly identified with our horizontal eddy fluxes; for example, vertical eddy fluxes could also contribute to Lee's residual. The importance of eddy-momentum fluxes on the larger scale ($5° - 9°$) is not inconsistent with suggested environmental influences on tropical cyclogenesis (Challa and Pfeffer 1980, 1990; Pfeffer and Challa 1981; Montgomery and Farrell 1993).

Chapter 7

SUMMARY AND CONCLUSIONS

In this work we have examined the dynamics of the interaction of moist penetrative convection with a larger-scale vortex. Convection is parameterized by its estimated net effect on the potential vorticity field. Convection could be initiated by environmental asymmetries such as those described by Challa and Pfeffer (1980,1990), Pfeffer and Challa(1981) and Montgomery and Farrell (1993), or by mesoscale processes. Here we provide an explicit explanation of how convective-scale rotational kinetic energy is transformed to kinetic energy of the large-scale vortex.

For simplicity, a three-dimensional quasigeostrophic balance model is used to elucidate the underlying dynamics. This approach has the virtue of excising gravity waves, allowing one to focus exclusively on the rotational advective dynamics. Vortex axisymmetrization proceeds by the ingestion of like-sign potential vorticity anomalies accompanied by the formation of filaments surrounding the larger-scale vortex as well as expulsion of opposite-sign PV anomalies. Our results on merger of like-sign PV anomalies are qualitatively consistent with theoretical work on vortex merger in two-dimensional Euler flow (Melander et al. 1988, Ritchie and Holland 1993) and two-layer quasigeostrophic flow (Polvani 1991). The dynamics of vortex Rossby waves are seen to usefully characterize the axisymmetrization process, in that the vortex Rossby wave theoretical predictions for the spinup magnitude and the location of wave mean-flow acceleration are in good agreement with the model results. Examination of Lagrangian trajectories, the Lorenz energy cycle and Eliassen-Palm flux diagrams give a consistent picture of the process of axisymmetrization and vortex intensification.

With reasonable assumptions about the magnitude of PV injection associated with moist penetrative convection, we obtain spinup to a 15 ms^{-1} cyclone on realistic timescales.

Simulation of a midlevel vortex with peripheral convection shows that axisymmetrization results in the spinup of a surface cyclone. A warm core vortex of order 5K forms as a natural consequence of the axisymmetrization process. In the relaxation experiments, both heat fiux and momentum flux are found to contribute to the development of the warm core. In the pulsed convective experiments, subsidence warming is initially too small to account for the observed warming; however, after the first τ_{eddy} subsidence warming is significant.

At the finite amplitudes determined consistent with our calculation of the magnitude of PV injection, the spinup obtained shows greater than linear dependence on the amplitude. This fact implies the existence of a nonlinear feedback mechanism associated with convectively forced vortex Rossby waves. Discrete neutral or weakly unstable vortex Rossby modes are observed to propagate azimuthally around the vortex center both at upper and lower levels; the possible role that these modes may play in orchestrating future convection, leading to further intensification of the vortex, requires additional study.

Numerical simulations of tropical cyclogenesis using a full physics primitive equation model (taking into account horizontal advection, vertical advection, stretching, tilting of horizontal vorticity and friction) show that the dominant contributions to the low-level vertical vorticity tendency are horizontal advection and stretching (Kurihara and Tuleya 1981). This provides evidence that our idealized model is not too idealized, i.e., that we have incorporated the fundamental processes producing the storm's vertical vorticity even though we have neglected, for example, boundary layer friction and the complex mesoscale interactions leading to tilting of horizontal vorticity. Observations (Lee 1986, 1989a, 1989b) suggest that small-scale eddy processes are important at the early stages of tropical cyclogenesis. These results are consistent with our expectations for vortex development by axisymmetrization in the presence of moist penetrative convection.

Further observations are needed, however, to confirm or falsify the theory described here. These include observations of patches of low-level cyclonic relative vorticity in association with convection near the incipient vortex, such as a mesoscale convectively-generated vortex. While one of the ultimate goals of an observational field program for tropical cyclogenesis should be to construct fine-scale PV maps, for convenience we suggest the use of

the absolute vorticity as a useful proxy for PV. A key process in our theory is the shearing of such vorticity patches by the incipient vortex. Accompanying the shearing one would like to observe the upgradient transport of vorticity into the vortex and the downgradient transport into surrounding filaments. As the dynamics of vortex Rossby waves have been shown to usefully characterize the wave, mean-flow interaction for the PV anomaly amplitudes considered here, it would be of great interest to observe wavelike features in the PV (or vorticity) field which are consistent with their local dispersion relation derived in MK. In principle, this dispersion relation can be used to distinguish vortex Rossby waves from gravity-inertia waves.

Future work will test the theoretical conclusions developed here in a fully nonlinear three-dimensional primitive equation model and an asymmetric balance model, with moist processes represented in a more realistic manner.

Appendix A

QG WAVE-MEAN FLOW DIAGNOSTICS IN CYLINDRICAL COORDINATES

A.1 Introduction

In this appendix we derive the wave-mean flow diagnostics for the three-dimensional quasigeostrophic model in cylindrical coordinates. Though the results are well known in the analogous Cartesian description of middle-latitude synoptic-scale motions, the corresponding derivation for stably stratified vortex flows at small Rossby numbers is presented here for completeness. The key results consist of the derivation of the Eliassen-Palm vector, the Sawyer-Eliassen equation, and the mean and eddy energetics equations.

A.2 Boussinesq Primitive Equations in Cylindrical Coordinates

The hydrostatic frictionless primitive equations on an f-plane with the Boussinesq approximation in cylindrical pseudo-height coordinates are:

$$\hat{r}: \quad \frac{\partial u}{\partial t} + u\frac{\partial u}{\partial r} + \frac{v}{r}\frac{\partial u}{\partial \lambda} + w\frac{\partial u}{\partial z} - fv - \frac{v^2}{r} = -\frac{\partial \Phi}{\partial r} \tag{A.1}$$

$$\hat{\lambda}: \quad \frac{\partial v}{\partial t} + u\frac{\partial v}{\partial r} + \frac{v}{r}\frac{\partial v}{\partial \lambda} + w\frac{\partial v}{\partial z} + fu + \frac{uv}{r} = -\frac{\partial \Phi}{r\partial \lambda} \tag{A.2}$$

$$\hat{z}: \quad 0 = -\frac{\partial \Phi}{\partial z} + \frac{g}{\theta_0}\Theta \tag{A.3}$$

$$\text{thermodynamic}: \quad \frac{\partial \Phi_z}{\partial t} + u\frac{\partial \Phi_z}{\partial r} + \frac{v}{r}\frac{\partial \Phi_z}{\partial \lambda} + w\frac{\partial \Phi_z}{\partial z} = \frac{g}{\theta_0}\dot{\Theta} \tag{A.4}$$

$$\text{continuity}: \quad \frac{\partial}{r\partial r}(ru) + \frac{\partial v}{r\partial \lambda} + \frac{\partial w}{\partial z} = 0 \tag{A.5}$$

Here $\dot{\Theta}$ denotes the rate of potential temperature change associated with cumulus convection after averaging over many cumulus cells, θ_0 is the potential temperature at the surface, and we recall that u, v, and w are the radial, azimuthal and vertical velocities respectively. Other notation is standard.

A.2.1 Quasigeostrophic Approximation

When the Rossby number v/fr is small compared to unity and thermal forcing evolves slowly with time, the flow evolves near a state of geostrophic balance. At zeroth order in the Rossby number, (A.1)-(A.5) with vanishing w at $z = 0, H$ are approximated by

$$fv \approx fv_g = \frac{\partial \phi}{\partial r}, \tag{A.6}$$

$$fu \approx fu_g = -\frac{\partial \phi}{r \partial \lambda}, \tag{A.7}$$

$$w = 0. \tag{A.8}$$

Flow evolution enters at first order in the Rossby number, with (A.1)-(A.5) approximated by

$$\left(\frac{\partial}{\partial t} + u_g \frac{\partial}{\partial r} + \frac{v_g}{r}\frac{\partial}{\partial \lambda}\right) u_g - f v_a - \frac{v_g^2}{r} = 0, \tag{A.9}$$

$$\left(\frac{\partial}{\partial t} + u_g \frac{\partial}{\partial r} + \frac{v_g}{r}\frac{\partial}{\partial \lambda}\right) v_g + f u_a + \frac{u_g v_g}{r} = 0, \tag{A.10}$$

$$0 = -\frac{\partial \phi}{\partial z} + \frac{g}{\theta_0}\theta, \tag{A.11}$$

$$\left(\frac{\partial}{\partial t} + u_g \frac{\partial}{\partial r} + \frac{v_g}{r}\frac{\partial}{\partial \lambda}\right) \phi_z + w N^2(z) = \frac{g}{\theta_0}\dot{\theta}, \tag{A.12}$$

$$\frac{\partial}{r \partial r}(r u_a) + \frac{\partial v_a}{r \partial \lambda} + \frac{\partial w}{\partial z} = 0, \tag{A.13}$$

where (u_a, v_a) are the ageostrophic radial and tangential velocities, respectively, and

$$N^2 = N^2(z) = \frac{g}{\theta_0}\frac{d\theta_r}{dz} \tag{A.14}$$

is the horizontally averaged static stability. θ is the flow potential temperature and θ_r is the potential temperature of the resting basic state (see Chapter 2).

The vertical vorticity equation is obtained by forming $\partial[r(A.10)]/(r\partial r) - \partial(A.9)/(r\partial\lambda)$:

$$\left(\frac{\partial}{\partial t} + u_g \frac{\partial}{\partial r} + \frac{v_g}{r}\frac{\partial}{\partial \lambda}\right) \zeta_g = -f\left(\frac{\partial}{r \partial r}(r u_a) + \frac{\partial v_a}{r \partial \lambda}\right), \tag{A.15}$$

where

$$\zeta_g = \frac{\partial}{r \partial r}(r v_g) - \frac{\partial u_g}{r \partial \lambda} = \frac{1}{f}\left[\frac{\partial}{r \partial r}\left(r \frac{\partial \phi}{\partial r}\right) + \frac{1}{r^2}\frac{\partial^2 \phi}{\partial \lambda^2}\right]. \tag{A.16}$$

Forming the combination $\partial\left[(A.12) \times \frac{f}{N^2}\right]/\partial z$ + (A.15) and using (A.13) to eliminate the divergence term yields the quasigeostrophic potential vorticity equation with a heat source

$$\left(\frac{\partial}{\partial t} + u_g\frac{\partial}{\partial r} + \frac{v_g}{r}\frac{\partial}{\partial \lambda}\right)\left[\zeta_g + \frac{\partial}{\partial z}\left(\frac{f}{N^2}\frac{\partial \phi}{\partial z}\right)\right] = \frac{g}{\theta_0}\frac{\partial}{\partial z}\left(\frac{f\dot{\theta}}{N^2}\right). \tag{A.17}$$

The bracketed quantity represents the quasigeostrophic potential vorticity minus f and will be denoted by Q_g.

A.2.2 Wave - Mean Flow Diagnostics

Let

$$\{u_g, v_g, \zeta_g, \phi, Q_g\} = \{\overline{u}_g(r,z,t), \overline{v}_g(r,z,t), \overline{\zeta}_g(r,z,t), \overline{\phi}(r,z,t), \overline{Q}_g(r,z,t)\}$$

$$+ \{u'_g(r,\lambda,z,t), v'_g(r,\lambda,z,t), \zeta'_g(r,\lambda,z,t), \phi'(r,\lambda,z,t), Q'_g(r,\lambda,z,t)\}, \tag{A.18}$$

where

$$\overline{(\,)} = \frac{1}{2\pi}\int_0^{2\pi}(\,)d\lambda \tag{A.19}$$

denotes an azimuthal average.

Mean PV Equation

From the definitions of u_g and Q_g

$$\overline{u}_g = -\overline{\frac{1}{fr}\frac{\partial \phi}{\partial \lambda}} = 0, \tag{A.20}$$

$$\overline{Q}_g = \overline{\zeta}_g + \frac{\partial}{\partial z}\left(\frac{f}{N^2}\frac{\partial \overline{\phi}}{\partial z}\right) = \frac{\partial}{r\partial r}(r\overline{v}_g) + \frac{\partial}{\partial z}\left(\frac{f}{N^2}\frac{\partial \overline{\phi}}{\partial z}\right). \tag{A.21}$$

Substituting (*A*.18) into (*A*.17) and azimuthally averaging yields the azimuthal mean PV equation:

$$\frac{\partial \overline{Q}_g}{\partial t} = -\frac{\partial}{r\partial r}(r\overline{u'_g Q'_g}) + \frac{g}{\theta_0}\frac{\partial}{\partial z}\left(\frac{f\overline{\dot{\theta}}}{N^2}\right), \tag{A.22}$$

where $\mathbf{u_g}\cdot\nabla_\mathbf{h}(\,) = \nabla_\mathbf{h}\cdot[\mathbf{u_g}(\,)]$ has been used.

Since $\overline{u'_g\zeta'_g} = 1/r^2\partial(\overline{r^2u'_gv'_g})/\partial r$, it follows that

$$\overline{u'_gQ'_g} = \overline{u'_g\zeta'_g} + \overline{u'_g\frac{\partial}{\partial z}\left(\frac{f}{N^2}\frac{\partial \phi'}{\partial z}\right)} \tag{A.23}$$

$$= \frac{1}{r^2}\frac{\partial}{\partial r}(r^2\overline{u'_g v'_g}) + \frac{\partial}{\partial z}\left(\frac{f}{N^2}\overline{u'_g\frac{\partial\phi'}{\partial z}}\right) \tag{A.24}$$

$$= \frac{1}{r}\left(\frac{\partial}{r\partial r}\left[r(\overline{rv'_g u'_g}\right] + \frac{\partial}{\partial z}\left[\frac{f}{N^2}r\overline{u'_g\phi'_z}\right]\right) \tag{A.25}$$

$$= -\frac{1}{r}\nabla\cdot\mathbf{F}, \tag{A.26}$$

where

$$\mathbf{F} = \left(-\overline{rv'_g u'_g}, -\frac{f}{N^2}r\overline{u'_g\phi'_z}\right) \tag{A.27}$$

is the Eliassen-Palm (EP) flux vector. In terms of $\mathbf{F}$ the mean PV equation (A.22) is

$$\frac{\partial\overline{Q}_g}{\partial t} = \frac{\partial}{r\partial r}\left(\nabla\cdot\mathbf{F}\right) + \frac{g}{\theta_0}\frac{\partial}{\partial z}\left(\frac{f\overline{\dot{\theta}}}{N^2}\right). \tag{A.28}$$

Mean Momentum and Temperature Equations

Azimuthal mean tangential momentum and temperature equations result on substituting (A.18) into equations (A.10) and (A.12), respectively, and azimuthally averaging. The result is

$$\frac{\partial\overline{v}_g}{\partial t} = -\overline{u'_g\zeta'_g} - f\overline{u}_a, \tag{A.29}$$

$$\frac{\partial\overline{\phi}_z}{\partial t} = -\frac{\partial}{r\partial r}\left[r\overline{u'_g\phi'_z}\right] - N^2\overline{w} + \frac{g}{\theta_0}\overline{\dot{\theta}}, \tag{A.30}$$

where

$$\{\overline{u}_a, \overline{w}, \overline{\dot{\theta}}\} = \frac{1}{2\pi}\int_0^{2\pi}\{u_a, w, \dot{\theta}\}d\lambda. \tag{A.31}$$

Mean Transverse Circulation Equation

A diagnostic equation for the azimuthal mean transverse circulation (mean secondary circulation) $(\overline{u}_a, \overline{w})$ is deduced by requiring that the mean vortex remain in a state of thermal wind balance. The thermal wind equation for the mean vortex is

$$f\frac{\partial\overline{v}_g}{\partial z} = \frac{\partial}{\partial r}\left(\frac{\partial\overline{\phi}}{\partial z}\right). \tag{A.32}$$

Differentiating (A.32) with respect to time and substituting (A.29) and (A.30) yields

$$N^2\frac{\partial\overline{w}}{\partial r} - f^2\frac{\partial\overline{u}_a}{\partial z} = f\frac{\partial}{\partial z}\overline{u'_g\zeta'_g} - \frac{\partial}{\partial r}\left[\frac{\partial}{r\partial r}\left(r\overline{u'_g\phi'_z}\right)\right] + \frac{g}{\theta_0}\frac{\partial\overline{\dot{\theta}}}{\partial r} \tag{A.33}$$

$$= f\frac{\partial}{\partial z}\left(\frac{1}{r^2}\frac{\partial}{\partial r}\left[r(r\overline{v'_g u'_g})\right]\right) - \frac{\partial}{\partial r}\left(\frac{\partial}{r\partial r}(r\overline{u'_g\phi'_z})\right) + \frac{g}{\theta_0}\frac{\partial\overline{\dot{\theta}}}{\partial r} \tag{A.34}$$

$$\equiv -\frac{\partial F}{\partial z} + \frac{\partial E}{\partial r}, \tag{A.35}$$

where $F = -f\overline{u_g'\zeta_g'}$ and $E = \frac{g}{\theta_0}\bar{\theta} - \frac{\partial}{r\partial r}(\overline{ru_g'\phi_z'})$. Defining a transverse streamfunction $\overline{\psi}$: $\overline{w} = \frac{\partial}{r\partial r}\overline{\psi}$, $\overline{u}_a = -\frac{1}{r}\frac{\partial \overline{\psi}}{\partial z}$, the transverse circulation equation is given by

$$N^2 \frac{\partial}{\partial r}\left(\frac{\partial}{r\partial r}\overline{\psi}\right) + \frac{f^2}{r}\frac{\partial^2 \overline{\psi}}{\partial z^2} = \frac{\partial E}{\partial r} - \frac{\partial F}{\partial z}. \tag{A.36}$$

Equation (A.36) is called the Sawyer-Eliassen equation.

By requiring that the volume integral of the relative angular momentum ($\rho r\bar{v}_g$) remains unchanged, it follows (from (A.29) and the boundary condition that $\bar{w}$ must vanish on the top and bottom boundaries) that the streamfunction $\overline{\psi}(r, H) = \overline{\psi}(r, 0)$. Without loss of generality, since only derivatives of $\overline{\psi}$ are physically significant, we can take $\overline{\psi} = 0$ on the boundaries.

A.2.3 The Lorenz Energy Cycle

Budgets for integrated mean kinetic, eddy kinetic, mean available and eddy available energies may be derived in a straightforward manner beginning with the quasigeostrophic total kinetic energy equation assuming frictionless flow

$$\frac{\partial}{\partial t}\left(\rho\frac{u_g^2 + v_g^2}{2}\right) + \nabla_h \cdot \left(\rho\mathbf{u_g}\frac{u_g^2 + v_g^2}{2}\right) + \nabla \cdot (\rho\mathbf{u_a}\phi) - \rho w\phi_z = 0, \tag{A.38}$$

and total available potential energy assuming adiabatic flow (i.e. in between convective pulses)

$$\frac{\partial}{\partial t}\left(\frac{\rho\phi_z^2}{2N^2}\right) + \nabla_h \cdot \left(\rho\mathbf{u_g}\frac{\phi_z^2}{2N^2}\right) + \rho w\phi_z = 0. \tag{A.39}$$

In (A.38) $\mathbf{u_a} = (u_a, v_a, w)$ and ρ is a constant average density for the troposphere. Equation (A.38) is obtained by forming $u_g \times (A.9) + v_g \times (A.10)$ and making use of (A.13) and the fact that the geostrophic wind is horizontally nondivergent. Equation (A.39) is obtained in a similar fashion after forming $\phi_z \times (A.12)$.

The integrated mean kinetic and eddy kinetic energy equations are then obtained as follows. Forming $\rho\overline{v}_g \times (A.29)$ and integrating over the entire fluid ($0 \leq \lambda \leq 2\pi$; $0 \leq z \leq H$; $0 \leq r \leq \infty$) gives the equation for integrated mean kinetic energy $\overline{K}$:

$$\frac{d\bar{K}}{dt} = [\bar{P} \cdot \bar{K}] + [K' \cdot \bar{K}], \tag{A.40}$$

where

$$\bar{K} = \left\langle \frac{1}{2}\rho\bar{v}_g^2 \right\rangle, \tag{A.41}$$

$$[\bar{P}\cdot\bar{K}] = \langle \rho\bar{w}\bar{\phi}_z \rangle, \tag{A.42}$$

and

$$[K'\cdot\bar{K}] = \left\langle \rho r\overline{u_g'v_g'}\frac{d\bar{\Omega}}{dr} \right\rangle. \tag{A.43}$$

Here $\bar{\Omega} = \bar{v}/r$ is the azimuthal mean angular velocity of the fluid and the bracket denotes a volume integral over the entire fluid. Substituting (A.18) into (A.38), azimuthally averaging, and then subtracting (A.40) from the averaged result, one obtains the equation for the integrated eddy kinetic energy K':

$$\frac{dK'}{dt} = [P'\cdot K'] - [K'\cdot\bar{K}], \tag{A.44}$$

where

$$K' = \left\langle \frac{1}{2}\rho(\overline{u_g'^2 + v_g'^2}) \right\rangle \tag{A.45}$$

and

$$[P'\cdot K'] = \langle \rho\overline{w'\phi_z'} \rangle.$$

The equations for integrated mean available and eddy available potential energy are obtained in a similar fashion. The equation for integrated mean available potential energy $\bar{P}$ is

$$\frac{d\bar{P}}{dt} = -[\bar{P}\cdot\bar{K}] + [P'\cdot\bar{P}], \tag{A.46}$$

while the equation for integrated eddy available potential energy P' is

$$\frac{dP'}{dt} = -[P'\cdot K'] - [P'\cdot\bar{P}]. \tag{A.47}$$

In (A.46) and (A.47)

$$\bar{P} = \left\langle \frac{1}{2}\rho\frac{\bar{\phi}_z^2}{N^2} \right\rangle, \tag{A.48}$$

$$P' = \left\langle \frac{1}{2}\rho\frac{\overline{\phi_z'^2}}{N^2} \right\rangle, \tag{A.49}$$

and

$$[P'\cdot\bar{P}] = \left\langle \frac{\rho f}{N^2}\frac{\partial\bar{v}_g}{\partial z}\overline{u_g'\phi_z'} \right\rangle. \tag{A.50}$$

As confirmation that the above is consistent with total energy conservation for adiabatic frictionless flow, we note that (A.40) + (A.44) + (A.46) + (A.47) yields

$$\frac{d}{dt}[\bar{K} + K' + \bar{P} + P'] = 0. \tag{A.51}$$

REFERENCES

Abramowitz, M., and I. A. Stegun, 1972: Handbook of mathematical functions. Dover Publications.

Arakawa, A., 1966: Computational design for long-term numerical integration of the equations of fluid motion: Two-dimensional incompressible flow. Part I. *Journal of Computational Physics*, **1**, 119-143.

Bartels, D. L., and R. A. Maddox, 1991: Midlevel cyclonic vortices generated by mesoscale convective systems. *Mon. Wea. Rev.*, **119**, 104-117.

Bosart, L.F., and F. Sanders, 1981: The Johnstown flood of July 1977: A long-lived convective storm. *J. Atmos. Sci.*, **38**, 1616-1642.

Burden, R. L., and J. D. Faires, 1989: Numerical analysis. PWS-KENT Publishing Company.

Challa, M., and R. L. Pfeffer, 1980: Effects of eddy fluxes of angular momentum on model hurricane development. *J. Atmos. Sci.*, **37**, 1603-1618.

Challa, M., and R. L. Pfeffer, 1990: Formation of Atlantic hurricanes from cloud clusters and depressions. *J. Atmos. Sci.*, **47**, 909-927.

Charney, J. G., 1948: On the scale of atmospheric motions. *Geophys. Publ.*, **17**, 1-17.

Edmon, H. J., Jr., B. J. Hoskins and M. E. McIntyre, 1980: Eliassen-Palm cross sections for the troposphere. *J. Atmos. Sci.*, **37**, 2600-2616.

Emanuel, K. A., 1989: The finite-amplitude nature of tropical cyclogenesis. *J. Atmos. Sci.*, **46**, 3431-3456.

Frank, W. M., 1977: The structure and energetics of the tropical cyclone: II. Dynamics and energetics. *Mon. Wea. Rev.*, **105**, 1136-1150.

Frank, W. M., 1987: Tropical cyclone formation. *A Global View of Tropical Cyclones*, R. L. Elsberry, W. M. Frank, G. J. Holland, J. D. Jarrell, and R. L. Southern, Eds., Office of Naval Research, 185 pp.

Fritsch, J. M., J. D. Murphy, and J. S. Kain, 1994: Warm core vortex amplification over land. *J. Atmos. Sci.*, **51**, 1780-1807.

Gallus, W. A., Jr., and R. H. Johnson, 1991: Heat and moisture budgets of an intense midlatitude squall line. *J. Atmos. Sci.*, **48**, 122-146.

Gazdag, J., 1976: Time-differencing schemes and transform methods. *J. Comp. Physics*, **20**, 196-207.

Gent, P. R., and J. C. McWilliams, 1986: The instability of barotropic circular vortices. *Geophys. Astrophys. Fluid Dynamics*, **35**,209-233.

Gray, W. M., 1968: Global view of the origin of tropical disturbances and storms. *Mon. Wea. Rev.*, **96**, 669-700.

Guinn, T. A., and W. H. Schubert, 1993: Hurricane spiral bands. *J. Atmos. Sci.*, **50**, 3380-3403.

Harr, P. A., M. S. Kalafsky, and R. L. Elsberry, 1996: Environmental conditions prior to formation of a midget tropical cyclone during TCM-93. *J. Atmos. Sci.*, **124**, 1693-1710.

Held, I. M., and P. J. Phillips, 1987: Linear and nonlinear barotropic decay on the sphere. *J. Atmos. Sci.*, **44**, 200-207.

Hertenstein, R. F. A., 1996: Evolution of potential vorticity associated with mesoscale convective systems. Paper 599, Dept. of Atmospheric Science, Colorado State University, 170 pp.

Holton, J. R., 1992: An introduction to dynamic meteorology. Academic Press, Inc.

Hoskins, B. J., and F. P. Bretherton, 1972: Atmospheric frontogenesis models: mathematical formulation and solution. *J. Atmos. Sci.*, **29**, 11-37.

Hoskins, B. J., M. E. McIntyre and A. W. Robertson, 1985: On the use and significance of isentropic potential vorticity maps. *Quart. J. Roy. Meteor. Soc.*, **111**, 877-946.

Johnston, E. C., 1981: Mesoscale vorticity centers induced by mesoscale convective complexes. M.S. thesis, University of Wisconsin, 54 pp.

Kallenbach, R. J., and M. T. Montgomery, 1995: Symmetrization, vortex Rossby waves, and hurricane motion in an asymmetric balance model. Paper 588, Dept. of Atmospheric Science, Colorado State University, 78 pp.

Kurihara, Y., and R. E. Tuleya, 1981: A numerical simulation study on the genesis of a tropical storm. *Mon. Wea. Rev.*, **109**, 1629-1653.

Lee, C. S., 1986: An observational study of tropical cloud cluster evolution and cyclogenesis in the Western North Pacific. Paper 403, Dept. of Atmospheric Science, Colorado State University, 250 pp.

Lee, C. S., 1989a: Observational analysis of tropical cyclogenesis in the Western North Pacific. Part I: Structural evolution of cloud clusters. *J. Atmos. Sci.*, **46**, 2580-2598.

Lee, C. S., 1989b: Observational analysis of tropical cyclogenesis in the Western North Pacific. Part II: Budget analysis. *J. Atmos. Sci.*, **46**, 2599-2616.

Lindzen, R. S., 1990: Dynamics in atmospheric physics. Cambridge University Press.

MacDonald, N. J., 1968: The evidence for the existence of Rossby-like waves in the hurricane vortex. *Tellus*, **20**, 138-150.

Mapes, B. E., and R. A. Houze Jr., 1995: Diabatic divergence profiles in Western Pacific mesoscale convective systems. *J. Atmos. Sci.*, **52**, 1807-1828.

McBride, J. L., 1979: Observational analysis of tropical cyclone formation. Paper 308, Dept. of Atmospheric Science, Colorado State University, 230 pp.

McBride, J. L., 1981a: Observational analysis of tropical cyclone formation. Part I: Basic description of data sets. *J. Atmos. Sci.*, **38**, 1117-1131.

McBride, J. L., 1981b: Observational analysis of tropical cyclone formation. Part III: Budget analysis. *J. Atmos. Sci.*, **38**, 1152-1166.

McBride, J. L., and R. Zehr, 1981: Observational analysis of tropical cyclone formation. Part II: Comparison of non-developing versus developing systems. *J. Atmos. Sci.*, **38**, 1132-1151.

Melander, M. V., N. J. Zabusky and J. C. McWilliams, 1988: Symmetric vortex merger in two dimensions: causes and conditions. *J. Fluid Mech.*, **195**, 303-340.

Montgomery, M. T., and J. Enagonio, 1998: Tropical cyclogenesis via convectively forced vortex Rossby waves in a three-dimensional quasigeostrophic model. Forthcoming in *Journal of the Atmospheric Sciences.*

Montgomery, M. T., and B. F. Farrell, 1993: Tropical cyclone formation. *J. Atmos. Sci.*, **50**, 285-310.

Montgomery, M. T., and R. J. Kallenbach, 1997: A theory for vortex Rossby-waves and its application to spiral bands and intensity changes in hurricanes. *Quart. J. Roy. Meteor. Soc.*, **123**, 435-465.

Ooyama, K., 1969: Numerical simulation of the life cycle of tropical cyclones. *J. Atmos. Sci.*, **26**, 3-40.

Ooyama, K. V., 1982: Conceptual evolution of the theory and modeling of the tropical cyclone. *J. Meteor. Soc. Japan*, **60**, 369-379.

Orlandi, P., and G. J. F. van Heijst, 1992: Numerical simulation of tripolar vortices in 2D flow. *Fluid Dynamics Research*, **9**, 179-206.

Orszag, S. A., 1971: Numerical simulation of incompressible flows within simple boundaries: accuracy. *J. Fluid Mech.*, **49**, 75-112.

Pedlosky, J., 1987: *Geophysical Fluid Dynamics.* 2d ed. Springer-Verlag, 710 pp.

Pfeffer, R. L., and M. Challa, 1981: A numerical study of the role of eddy fluxes of momentum in the development of Atlantic hurricanes. *J. Atmos. Sci.*, **38**, 2393-2398.

Polvani, L. M., 1991: Two-layer geostrophic vortex dynamics. Part 2. Alignment and two-layer V-states. *J. Fluid Mech.*, **225**, 241-270.

Polvani, L. M., and X. J. Carton, 1990: The tripole: a new coherent vortex structure of incompressible two-dimensional flows. *Geophys. Astrophys. Fluid Dyn.*, **51**, 87-102.

Press, W. H., S. A. Teukolsky, W. T. Vetterling and B. F. Flannery, 1992: Numerical recipes in FORTRAN, 2nd edition. Cambridge University Press.

Reed, R. J., D. C. Norquist and E. E. Recker, 1977: The structure and properties of African wave disturbances as observed during Phase III of GATE. *Mon. Wea. Rev.*, **105**, 317-333.

Ritchie, E. A., 1995: Mesoscale aspects of tropical cyclone formation. Ph.D. thesis, Monash University, 167 pp.

Ritchie, E. A., and G. J. Holland, 1993: On the interaction of tropical-cyclone-scale vortices. II: Discrete vortex patches. *Quart. J. Roy. Meteor. Soc.*, **119**, 1363-1379.

Ritchie, E. A., and G. J. Holland, 1997: Scale interactions during the formation of Typhoon Irving. *Mon. Wea. Rev.*, , in press.

Rotunno, R., and K. A. Emanuel, 1987: An air-sea interaction theory for tropical cyclones. Part II: Evolutionary study using a nonhydrostatic axisymmetric numerical model. *J. Atmos. Sci.*, **44**, 542-561.

Shapiro, L. J., 1977: Tropical storm formation from easterly waves: a criterion for development. *J. Atmos. Sci.*, **34**, 1007-1021.

Shapiro, L. J., and M. T. Montgomery, 1993: A three-dimensional balance theory for rapidly rotating vortices. *J. Atmos. Sci.*, **50**, 3322-3335.

Shepherd, T.G., 1987: Rossby waves and two-dimensional turbulence in a large-scale zonal jet. *J. Fluid Mech.*, **183**, 467-509.

Simpson, J., E. Ritchie, G. J. Holland, J. Halverson and S. Stewart, 1997: Mesoscale interactions in tropical cyclone genesis. *Mon. Wea. Rev.*, , in press.

Smith, G. B., and M. T. Montgomery, 1995: Vortex axisymmetrization: Dependence on azimuthal wavenumber or asymmetric radial structure changes. *Quart. J. Roy. Meteor. Soc.*, **121**, 1615-1650.

Smith, R. A., and M. N. Rosenbluth, 1990: Algebraic instability of hollow electron columns and cylindrical vortices. *Physical Review Letters*, **64**, 649-652.

Smith, R. K., 1997: On the theory of CISK. *Quart. J. Roy. Meteor. Soc.*, **123**, 407-418.

Stevens, B., D. A. Randall, X. Lin and M. T. Montgomery, 1997: A comment on: On large-scale circulations in convecting atmospheres by Emanuel, Neelin and Bretherton. *Quart. J. Roy. Meteor. Soc.*, in press.

Trier, S. B., W. C. Skamarock, M. A. LeMone, and D. B. Parsons, 1997: Structure and evolution of the 22 February 1993 TOGA COARE squall line: Numerical simulations. *J. Atmos. Sci.*, **53**, 2861-2886.

Tuleya, R. E., and Y. Kurihara, 1981: A numerical study on the effects of environmental flow on tropical storm genesis. *Mon. Wea. Rev.*, **109**, 2487-2506.

Tuttle, J. D., and B. Gall, 1995: Radar analysis of hurricanes Andrew and Hugo. *Proceedings 21st Conference on Hurricanes and Tropical Meteorology*, Miami, Florida, 608-610.

Velasco, I., and J. M. Fritsch, 1987: Mesoscale convective complexes in the Americas. *Jour. Geophys. Research*, **92**, 9591-9613.

Weisman, M. L., W. C. Skamarock, J. B. Klemp, and C. Davis, 1993: The generation of mesoscale convective vortices within long-lived convective systems. *20th Conference on Hurricanes and Tropical Meteorology*, San Antonio, Texas, 120-123.

Zehr, R. M., 1992: Tropical cyclogenesis in the Western North Pacific. *NOAA Technical Report NESDIS 61*, 181 pp.

Zehr, R., 1976: Tropical disturbance intensification. Paper 259, Dept. of Atmospheric Science, Colorado State University, 91 pp.

Zhang, D., and J. M. Fritsch, 1987: Numerical simulation of the Meso-β scale structure and evolution of the 1977 Johnstown flood. Part II: Inertially stable warm-core vortex and the mesoscale convective complex. *J. Atmos. Sci.*, **44**, 2593-2612.